Final Report

Low-Cost General Aviation Autonomous Navigation Project

Submitted to

Federal Aviation Administration
R&D Engineering Field Office, AAR-210
NASA, Langley Research Center
Hampton, VA 23681

By

J.E. Jackson (Project Director)
A.L. Highsmith
R.E. Leland
S. Kotru
H.P. Stern
T.M. Klein
L.T. Wurtz

The University of Alabama
College of Engineering
Tuscaloosa, AL 35487

December, 2006

CONTENTS

CONTENTS

1. EXECUTIVE SUMMARY

1.1 Introduction

Because GPS is subject to periodic failures, its use in replacing all or part of ground-based navigation for general aviation depends upon developing satisfactory backup systems. A great technical challenge for low-cost GA autonomous navigation is the need for accurate, low-cost gyroscopes. To try to develop low-cost gyroscopes researchers are focusing on MEMS technology. This paper reports the status of one such research program at the University of Alabama. The UA research program proposed improving the accuracy of MEMS gyroscopes in three ways: (1) increase mass of the gyro, that is, produce a meso-scale gyro using MEMS technology, (2) increase signal amplitude by using piezoelectric actuators and sensors (instead of conventional electrostatics), and (3) use alternatives to Silicon (for example, Quartz) that should reduce accuracy degradation caused by temperature changes. The following is a summary of the status of the development effort. Sections are devoted to fabrication issues, materials development, electronic system development, simulation, and test results.

To overcome the technological challenges in building the "UA X-post Gyro" the following must be achieved:

- Design and construct an electronic system capable of measuring both relatively large and extremely small rates of rotation
- Develop a computer simulation capability to be used for device design and future design optimization
- Develop the capability of producing high-quality thin films of piezoelectric materials
- Develop MEMS-technology fabrication processes that have never before been done
- Develop a MEMS clean room for production of the gyro devices
- Develop a Navigation Laboratory capable of testing MEMS-technology gyroscopes
- Develop a laser trimming system for improving the performance of the manufactured MEMS-technology gyroscopes

1.2 Device Structure and Operation Theory

A photograph of the MEMS gyroscope is shown in Fig. 1.1. It consists of a cross beam and a post. We call the gyroscope an "X-Post Gyroscope". The material of both beam and post are silicon. Four thin films, PNZT pads are deposited on the X-direction beam, and used as actuators. The other four thin film pads are deposited on the Y-direction beam, and used as sensors. The reason, why PNZT pads are used as actuators and sensors, is it is hoped that this will result in larger electrical signals than could be achieved by electrostatic excitation. If true, a higher signal to noise ratio could be expected. The gyroscope operates according to the Coriolis coupling principle. The post mass is vibrated in the X-Z plane around y-axis when suitable excitation voltage is applied to the actuators, shown in Fig. 1.2. When the gyroscope is rotated around the Z-axis, the post mass tends to vibrate in the Y-Z plane due to Coriolis coupling, shown in Fig. 1.3. By measuring the amplitude of the induced vibration, the angular rate of the applied rotation can be obtained. To obtain as large response as possible, the second natural frequency is applied as the frequency of the actuating voltage.

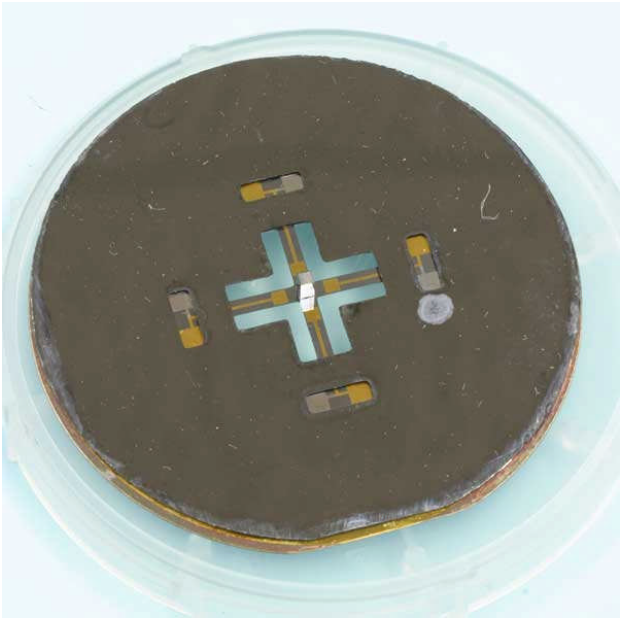

FIG. 1.1. The UA X-Post gyroscope.

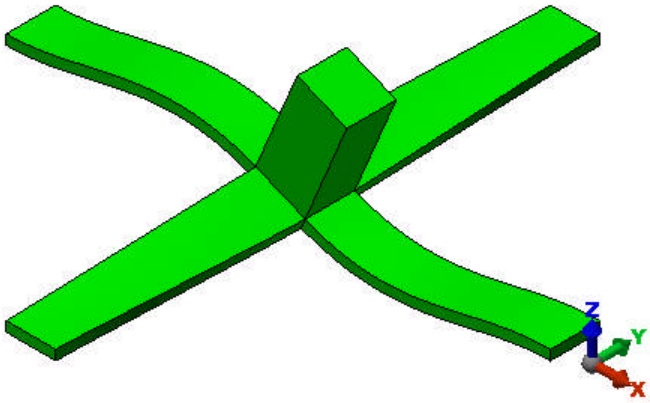

FIG. 1.2. Vibrating mode under actuating voltage.

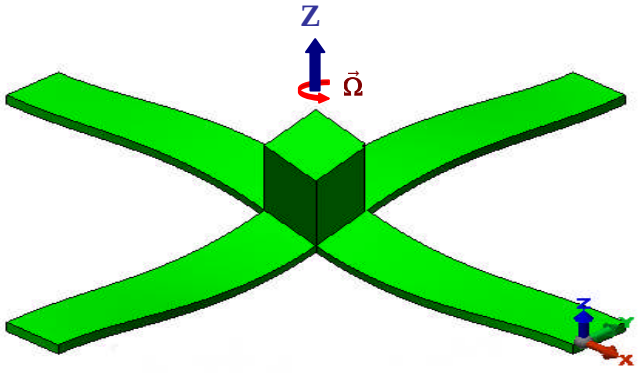

FIG. 1.3. Vibrating mode under actuating voltage and rotation.

1.3 Risks

The X-post gyro was a high-risk project for several reasons. These include:

- The possibility that time and funding may not be sufficient ($10.8 million over six years). We were supplied with information that the Draper Laboratories "Z-axis" gyro had consumed $100+ million without a navigation-grade device and the JPL-Boeing-Honeywell Meso-gyro consumed $30 million+ over 11 years without a navigation grade device.

- Rather than try to achieve success with an electrostatically driven device, such as those mentioned above, we chose to try to develop a piezoelectrically driven device. We saw no logic in trying the same approach as JPL and Draper Labs. The risk is that piezoelectric MEMS-technology devices are not nearly so well understood as conventional silicon-based technology.

- It was possible that we would not be able to produce or purchase piezoelectric thin films of sufficient quality.

- Some of the MEMS-technology processing steps have not, to our knowledge, been achieved anywhere else, so we needed to develop these processes.

- The fabrication process required very many steps to be performed successfully. With one device per wafer, our yield was binary- either a success or a failure. We did not have the luxury of producing many devices on a wafer and discarding the imperfect ones.

- We did not know (and still don't know) whether a device of our design can be produced to give the navigational accuracy needed. Simulations were developed to try to address this but they do not include some of the effects in the actual device.

1.4 Accomplishments

So far, the FAA gyro project has produced several outcomes we consider notable. These include

- Development of a simulation tool that is capable of assisting design of future mechanical gyros (not just of the X-post design.) It should be possible to assess effects of changing materials and shapes. We can assess the effects of imperfection of manufacturing and of temperature cycling.

- We have developed the ability to produce very high quality PNZT piezoelectric thin films. The uniformity and piezoelectric properties of these are superior to products available commercially.

- New MEMS-technology fabrication processes were developed. These will provide useful guidance to others in the future.

- We successfully constructed an X-post gyro that oscillates precisely at its designed frequency. It is premature to assess whether this design will eventually allow accurate rate measurements.

- Both analog and digital electronic control systems were produced. The analog system is operational and the digital system awaits connection to a device and the necessary programming.

1.5 Status of the X-post Gyro

Near the end of the project we were able to test the first X-post gyro design. The gyro oscillates at the designed frequency but we have not yet been able to measure rotation rates.With a small grant obtained since the end of the FAA project, we are attempting to correct some of the deficiencies we have seen in the initial device. New masks are being produced with the goal of testing the next generation design. Better electrical shielding will be provided and an attempt to reduce parasitic capacitance will tried by reducing electrode size. If possible, laser trimming will be attempted. Due to the complex manufacturing methodology, it is difficult to see how the goal of “low-cost” can be achieved in the near future with a piezoelectric thin-film device. However, the term “low-cost” is relative and what would be considered “low-cost” for one application may not be acceptable for another.

2. SIMULATION

2.1 Summary

During the project we developed a three-dimensional finite element code for dynamic analysis of three-dimensional systems, such as gyroscopes. This capability was needed for the initial design of the mechanical behavior and also for future design iterations to improve performance. There were two reasons why we did not choose to use an existing commercial code. First, our design proposed to make use of piezoelectric thin films for actuators and sensors. Piezoelectric finite elements in the codes we evaluated, such as ABAQUS, do have piezoelectric elements, but these are either two-dimensional, in-plane elements that accept an in plane applied voltage, or a full 3-D element. Since our device is a little unusual in that we apply a voltage through the thin film (perpendicular to the surface), we were left with only the choice of 3-D hexahedron piezo elements. However, because of the high aspect ratios of the thin films, we would have had to use very many 3-D elements. We felt that this would have made our simulations prohibitively expensive in human and computer resources, since the simulations involve computing dynamic response over thousands of time steps for each simulation. A second reason was that we wanted access to the source code because we had a long-term goal of integration of the finite element mechanical simulation to software simulating the gyro control system.

Beginning with a code already developed by one of these investigators, the primary work involved (1) development and implementation of a piezoelectric thin film finite element, and (2) inclusion of the Coriolis effect in the code. The rest of this chapter discusses development of the simulation tool, called BAMEFEM.

2.2 Introduction

The piezoelectric element presented in this chapter is an improvement of Chowdury's piezoelectric element.[1] The piezoelectric element developed by the author contains 9 DOFS (8 displacement DOFS and 1 electric DOF); and Chowdury's piezoelectric element contains 12 DOFS (8 displacement DOFS and 4 electric DOF). ABAQUS results and several experiments are used to examine the correctness of the author's piezoelectric element.

2.3 Formulation of 4-node piezoelectric film finite element

2.3.1 Constitutive equation

The coupling constitutive equation of linear piezoelectric materials between the elastic field and the electric field strain can be represented by the direct and the converse piezoelectric equations, respectively.[2]

$$\begin{Bmatrix} D_x \\ D_y \\ D_z \end{Bmatrix} = \begin{bmatrix} e_{11} & e_{12} & e_{13} & e_{14} & e_{15} & e_{16} \\ e_{21} & e_{22} & e_{23} & e_{24} & e_{25} & e_{26} \\ e_{31} & e_{32} & e_{33} & e_{34} & e_{35} & e_{36} \end{bmatrix} \begin{Bmatrix} \in_{11} \\ \in_{22} \\ \in_{33} \\ \in_{23} \\ \in_{13} \\ \in_{12} \end{Bmatrix} + \begin{bmatrix} \varepsilon^s_{11} & \varepsilon^s_{12} & \varepsilon^s_{13} \\ \varepsilon^s_{21} & \varepsilon^s_{22} & \varepsilon^s_{23} \\ \varepsilon^s_{31} & \varepsilon^s_{32} & \varepsilon^s_{33} \end{bmatrix} \begin{Bmatrix} E_x \\ E_y \\ E_z \end{Bmatrix} \qquad (2\text{-}1)$$

$$\begin{Bmatrix}\sigma_{11}\\ \sigma_{22}\\ \sigma_{33}\\ \sigma_{23}\\ \sigma_{13}\\ \sigma_{12}\end{Bmatrix}=\begin{bmatrix}C_{11}^0 & C_{12}^0 & C_{13}^0 & C_{14}^0 & C_{15}^0 & C_{16}^0\\ C_{12}^0 & C_{22}^0 & C_{23}^0 & C_{24}^0 & C_{25}^0 & C_{26}^0\\ C_{13}^0 & C_{23}^0 & C_{33}^0 & C_{34}^0 & C_{35}^0 & C_{36}^0\\ C_{14}^0 & C_{24}^0 & C_{34}^0 & C_{44}^0 & C_{45}^0 & C_{46}^0\\ C_{15}^0 & C_{25}^0 & C_{35}^0 & C_{45}^0 & C_{55}^0 & C_{56}^0\\ C_{16}^0 & C_{26}^0 & C_{36}^0 & C_{46}^0 & C_{56}^0 & C_{66}^0\end{bmatrix}\begin{Bmatrix}\in_{11}\\ \in_{22}\\ \in_{33}\\ \in_{23}\\ \in_{13}\\ \in_{12}\end{Bmatrix}-\begin{bmatrix}e_{11} & e_{21} & e_{31}\\ e_{12} & e_{22} & e_{32}\\ e_{13} & e_{23} & e_{33}\\ e_{14} & e_{24} & e_{34}\\ e_{15} & e_{25} & e_{35}\\ e_{16} & e_{26} & e_{36}\end{bmatrix}\begin{Bmatrix}E_x\\ E_y\\ E_z\end{Bmatrix} \quad (2\text{-}2)$$

where, $\{D_i\}$, $[e]$, $\{\in_{ij}\}$, $[\varepsilon^s]$ and $\{E_i\}$ are electric displacement vector, the piezoelectric coupling coefficients matrix for Stress-Charge form, strain tensor, the electric permittivity matrix and the electric field componenets, respectively; and $\{\sigma_{ij}\}$ and $[C]$ are stress tensor and the elasticity matrix, respectively.

2.3.2 Element stiffness matrix and element mass element

Piezoelectricity is a coupling between a material's mechanical and electrical behaviors. The equilibrium equation of each element for a material with coupled mechanical and electric properties can be described by the equation of motion[1]

$$\begin{bmatrix}[M^e] & 0\\ 0 & 0\end{bmatrix}\begin{Bmatrix}\ddot{u}^e\\ \ddot{\varphi}^e\end{Bmatrix}+\begin{bmatrix}[K_{uu}^e] & [K_{u\varphi}^e]\\ [K_{\varphi u}^e] & [K_{\varphi\varphi}^e]\end{bmatrix}\begin{Bmatrix}u^e\\ \varphi^e\end{Bmatrix}=\begin{Bmatrix}F^e\\ \mathrm{Q^e}\end{Bmatrix} \quad (2\text{-}3)$$

where, $\left[M^e\right]$, $\left[K_{uu}^e\right]$, $\left[\bar{K}_{u\varphi}^e\right]$ and $\left[K_{\varphi\varphi}^e\right]$ are element mass matrix, element stiffness matrix, element piezoelectric stiffness matrix and element dielectric stiffness matrix, respectively. $\{F^e\}$ is the force vector (mechanical and electrical) of element *e*, and $\{Q^e\}$ is the element charge.

$$[K_{uu}^e]=\int_V[B_u]^t[c][B_u]dV=t\int_{-1}^{1}\int_{-1}^{1}[B_u]^t[c][B_u]\left|J\right|drds \quad (2\text{-}4)$$

$$[K_{u\varphi}^e]=\int_V[B_u]^t[e][B_\varphi]dV=t\int_{-1}^{1}\int_{-1}^{1}[B_u]^t[e][B_\varphi]\left|J\right|drds \quad (2\text{-}5)$$

$$[K_{\varphi\varphi}^e]=-\int_V[B_\varphi]^t[\varepsilon^s][B_\varphi]dV=-t\int_{-1}^{1}\int_{-1}^{1}[B_\varphi]^t[\varepsilon^s][B_\varphi]\left|J\right|drds \quad (2\text{-}6)$$

$$\left[\bar{K}_{u\varphi}^e\right]=\left[K_{\varphi u}^e\right]^T \quad (2\text{-}7)$$

In equation (2-4), $[c]$ is the elasticity matrix of a material. For a 3-D orthotropic material, the elastic constant matrix is[1]

$$[C]=\begin{bmatrix}C_{11}^0 & C_{12}^0 & C_{13}^0 & 0 & 0 & 0\\ C_{12}^0 & C_{22}^0 & C_{23}^0 & 0 & 0 & 0\\ C_{13}^0 & C_{23}^0 & C_{33}^0 & 0 & 0 & 0\\ 0 & 0 & 0 & C_{44}^0 & 0 & 0\\ 0 & 0 & 0 & 0 & C_{55}^0 & 0\\ 0 & 0 & 0 & 0 & 0 & C_{66}^0\end{bmatrix} \quad (2\text{-}8)$$

For 2-D plane problems the matrix can be compressed to the form of equation (2-9).[3]

$$[c]=\begin{bmatrix}c_{11} & c_{12} & 0\\ c_{12} & c_{22} & 0\\ 0 & 0 & c_{33}\end{bmatrix} \quad (2\text{-}9)$$

In equation (2-9), c_{11}, c_{12}, c_{22} and c_{33} can be obtained by following equations:[1]

$$\left.\begin{aligned} c_{11} &= \frac{C_{11}^o C_{33}^o - (C_{13}^o)^2}{C_{33}^o} \\ c_{12} &= \frac{C_{12}^o C_{33}^o - C_{13}^o C_{23}^o}{C_{33}^o} \\ c_{22} &= \frac{C_{22}^o C_{33}^o - (C_{23}^o)^2}{C_{33}^o} \\ c_{33} &= C_{44}^o \end{aligned}\right\} \tag{2-10}$$

In equation (2-5), [e] is the piezoelectric coupling coefficients matrix for stress-charge form

$$[e] = [d][C] \tag{2-11}$$

where, [d] is the piezoelectric coupling coefficient matrix for Strain-Charge form, units C/N (Coulomb/Newton).

For a plain stress element, [e] has the form

$$[e] = \begin{bmatrix} 0 & 0 & 0 \\ 0 & 0 & 0 \\ e_{31} & e_{32} & 0 \end{bmatrix} \tag{2-12}$$

In equation (2-6), $\left[\varepsilon^s\right]$ is the electric permittivity matrix, it has the form

$$\left[\varepsilon^s\right] = \left[\varepsilon^T\right] - [d][C][d]^T \tag{2-13}$$

where, [ε^T] is the permittivity matrix, subscript T means that the permittivity data was measured under at least a constant, and preferably a zero, stress field.

For a plain stress element, $\left[\varepsilon^s\right]$ has the form

$$\left[\varepsilon^s\right] = \begin{bmatrix} \varepsilon_{11}^s & 0 & 0 \\ 0 & \varepsilon_{22}^s & 0 \\ 0 & 0 & \varepsilon_{33}^s \end{bmatrix} \tag{2-14}$$

In equations (2-4) ~ (2-6), matrix [B_u] is the usual geometrical matrix for a four-node quadrilateral:

$$[B_u] = \begin{bmatrix} N_{1,x} & 0 & N_{2,x} & 0 & N_{3,x} & 0 & N_{4,x} & 0 \\ 0 & N_{1,y} & 0 & N_{2,y} & 0 & N_{3,y} & 0 & N_{4,y} \\ N_{1,y} & N_{1,x} & N_{2,y} & N_{2,x} & N_{3,y} & N_{3,x} & N_{4,y} & N_{4,x} \end{bmatrix} \tag{2-15}$$

$N_{i,x}$, $N_{i,y}$ in equation (2-15) (i =1,2,3,4) can be obtained by following equations

$$\begin{bmatrix} N_{i,x} \\ N_{i,y} \end{bmatrix} = \begin{bmatrix} r_{,x} & t_{,x} \\ r_{,y} & t_{,y} \end{bmatrix} \begin{bmatrix} N_{i,r} \\ N_{i,s} \end{bmatrix} = [J]^{-1} \begin{bmatrix} N_{i,r} \\ N_{i,s} \end{bmatrix} \tag{2-16}$$

where, [J] is the Jacobian matrix for 4-node isoparametric elements. The shape functions and their derivatives are[4]

$$N_i = \frac{1}{4}(1+rr_i)(1+ss_i) = \frac{1}{4}\begin{bmatrix}(1-r)(1-s)\\(1+r)(1-s)\\(1+r)(1+s)\\(1-r)(1+s)\end{bmatrix} \tag{2-17}$$

$$N_{i,r} = \frac{1}{4}r_i(1+ss_i) = \frac{1}{4}\begin{bmatrix}-1+s\\1-s\\1+s\\-1-s\end{bmatrix} \tag{2-18}$$

$$N_{i,s} = \frac{1}{4}s_i(1+rr_i) = \frac{1}{4}\begin{bmatrix}-1+r\\-1-r\\1+r\\1-r\end{bmatrix} \tag{2-19}$$

The electric field vs. electric potential relation for a 4-node PNZT film element is

$$E_i = -\varphi_{,i} \tag{2-20}$$

Since the electric potential is constant throughout the plane of the element[5]

$$\varphi_k(r,s) = \varphi_k \tag{2-21}$$

Assume that the electric potential changes linearly through the thickness direction of the element, combined equations (2-20) and (2-21), we can obtain

$$\{E\} = \begin{Bmatrix}E_x\\E_y\\E_z\end{Bmatrix} = \begin{Bmatrix}0\\0\\E_z\end{Bmatrix} = \begin{Bmatrix}\partial/\partial x\\\partial/\partial y\\\partial/\partial z\end{Bmatrix}\{\varphi\} = -\begin{Bmatrix}0\\0\\1/t\end{Bmatrix}\{\varphi\} = -\left[B_\varphi\right]\{\varphi\} \tag{2-22}$$

Then,

$$\left[B_\varphi\right] = \begin{Bmatrix}0\\0\\1/t\end{Bmatrix} \tag{2-23}$$

In equations (2-22) and (2-23), t is the thickness of the 4-node PNZT film element. From the above equations, it can seen that the dimension of matrices $\left[K^e_{uu}\right]$, $\left[K^e_{u\varphi}\right]$, $\left[K^e_{\varphi u}\right]$ and $\left[K^e_{\varphi\varphi}\right]$ are 8×8, 8×1, 1×8 and 1×1, respectively. In the free vibration analysis, vector $\{Q^e\}$ is usually set to zero.[6] Thus, the voltage output in sensor elements can be obtained by solving the second row of equation (2-3)

$$\{\varphi_s\} = \left[K^e_{\varphi\varphi}\right]^{-1}\left\{-\left[K^e_{\varphi u}\right]\{u^e\}\right\} \tag{2-24}$$

Substituting equation (4-24) into the first row of equation (4-3) yields

$$\left[M^e\right]\{\ddot{u}^e\} + \left[K^e\right]\{u^e\} = \{F^e\} \tag{2-25}$$

where $\left[K^e\right]$ is defined by the equation

$$\left[K^e\right] = \left[K^e_{uu}\right] - \left[K^e_{u\varphi}\right]\left[K^e_{\varphi\varphi}\right]^{-1}\left[K^e_{\varphi u}\right] \tag{2-26}$$

$\left[M^e\right]$ is the consistent element mass matrix, and is given by

$$\left[M^e\right] = \int_{V^e} [N]^T \rho [N] dV^e = t \int_{-1}^{1}\int_{-1}^{1} [N]^T \rho [N] |J| drds \tag{2-27}$$

2.3.3 Determination of the electrical force vector

In the first row of equation (2-3), the element force vector $\{F^e\}$ can be decomposed into

$$\{F^e\} = \begin{Bmatrix} F^{eT} \\ F^{eQ} \end{Bmatrix} \tag{2-28}$$

where, $\{F^{eT}\}$ is the mechanical force vector, and $\{F^{eQ}\}$ is the electrical force vector due to the applied charges of the actuators.

For the free vibration problem, vector $\{Q^e\}$ is usually set to zero. The equation (2-3) can be rearranged into the form[7]

$$\begin{bmatrix} [M^e] & 0 \\ 0 & 0 \end{bmatrix} \begin{Bmatrix} \ddot{u}^e \\ \ddot{\varphi}^e \end{Bmatrix} + \begin{bmatrix} [K^e_{uu}] & [K^e_{u\varphi}] \\ [K^e_{\varphi u}] & [K^e_{\varphi\varphi}] \end{bmatrix} \begin{Bmatrix} u^e \\ \varphi^e \end{Bmatrix} = \begin{Bmatrix} F^{eT} \\ 0 \end{Bmatrix} + \begin{Bmatrix} 0 \\ F^{eQ} \end{Bmatrix} \tag{2-29}$$

Then, the first row of equation (4-29) can be written as

$$\left[M^e\right]\{\ddot{u}^e\} + \left[K^e_{uu}\right]\{u^e\} = \{F^{eT}\} - \left[K^e_{u\varphi}\right]\{\varphi^e\} = \{F^{eT}\} + \{F^{e\varphi}\} \tag{2-30}$$

where
$$\{F^{e\varphi}\} = -\left[K^e_{u\varphi}\right]\{\varphi^e\} \tag{2-31}$$

Equation (2-31) is defined as the element electrical force vector produced by the voltage applied to the actuator elements.

2.3.4 Stress and strain vectors

For a two dimensional shape sensor or actuator, the equations (2-1) and (2-2) can be compressed into

$$\begin{Bmatrix} D_x \\ D_y \\ D_z \end{Bmatrix} = \begin{bmatrix} 0 & 0 & 0 \\ 0 & 0 & 0 \\ e_{31} & e_{32} & 0 \end{bmatrix} \begin{Bmatrix} \in_x \\ \in_y \\ \in_{xy} \end{Bmatrix} + \begin{bmatrix} \varepsilon^s_{11} & 0 & 0 \\ 0 & \varepsilon^s_{22} & 0 \\ 0 & 0 & \varepsilon^s_{33} \end{bmatrix} \begin{Bmatrix} 0 \\ 0 \\ E_z \end{Bmatrix} \tag{2-32}$$

$$\begin{Bmatrix} \sigma_x \\ \sigma_y \\ \tau_{xy} \end{Bmatrix} = \begin{bmatrix} c_{11} & c_{12} & 0 \\ c_{12} & c_{22} & 0 \\ 0 & 0 & c_{33} \end{bmatrix} \begin{Bmatrix} \in_x \\ \in_y \\ \gamma_{xy} \end{Bmatrix} + \begin{bmatrix} 0 & 0 & e_{31} \\ 0 & 0 & e_{32} \\ 0 & 0 & 0 \end{bmatrix} \begin{Bmatrix} 0 \\ 0 \\ E_z \end{Bmatrix} \tag{2-33}$$

From equation (2-32), we can obtain $D_x = 0$ and $D_y = 0$.

The strain-displacement relationship is given by

$$\begin{Bmatrix} \in_x \\ \in_y \\ \tau_{xy} \end{Bmatrix} = [B_u]\{u\} \tag{2-34}$$

where $[B_u]$ can be obtained from equation (2-15). For an orthotropic piezoelectric material the strain in the thickness direction (Z-direction) can be obtained from equation[1]

$$\in_{zz} = -\frac{C_{13}^0 \in_{xx} + C_{23}^0 \in_{yy}}{C_{33}^0} \tag{2-35}$$

Change in thickness can be obtained by

$$\Delta t = \in_{zz} t \tag{2-36}$$

2.3.5 Implementation of piezoelectric film element

The implementation of the piezoelectric film element is in the module QUAD. QUAD contains 4 element types, standard 2D 4-node quadrilateral element (S2D4), 2D 4-node quadrilateral conforming element is applied to a 3D structure system (S3D4), 2D 4-node quadrilateral non-conforming element is applied to a 3D structure system (N3D4), 2D 4-node quadrilateral piezoelectric element (S2D4P) and 2D 4-node quadrilateral piezoelectric element is applied to a 3D structure system (S3D4P). Chowdury's thesis discussed the details how 2D elements are applied to a 3D structure system.[1]

2.4 Numerical examples for validation of thin film piezo element

2.4.1 Verification using ABAQUS

2.4.1.1 Material properties.

To verify the correctness of the developed piezoelectric thin film element, the author used one example. The selected material for the example is PZT-4, the material properties for strain-charge format are listed as follows:[1]

$$[S_E] = 1.0\text{e-}12 * \begin{bmatrix} 12.3 & -4.05 & -5.31 & 0 & 0 & 0 \\ -4.05 & 12.3 & -5.31 & 0 & 0 & 0 \\ -5.31 & -5.31 & 15.5 & 0 & 0 & 0 \\ 0 & 0 & 0 & 39 & 0 & 0 \\ 0 & 0 & 0 & 0 & 39 & 0 \\ 0 & 0 & 0 & 0 & 0 & 32.7 \end{bmatrix} \tag{2-37}$$

where, S_E defines the compliance coefficients for Strain-Charge format, units m^2/N.

$$[\mathrm{d}] = 1.0\text{e-}12 * \begin{bmatrix} 0 & 0 & 0 & 0 & 496 & 0 \\ 0 & 0 & 0 & 496 & 0 & 0 \\ -123 & -123 & 289 & 0 & 0 & 0 \end{bmatrix} \tag{2-38}$$

where, [d] defines the piezoelectric coupling coefficients for strain-charge form, units *C/N*.

$$[\varepsilon^T] = 8.854\text{e-}12 * \begin{bmatrix} 1475 & 0 & 0 \\ 0 & 1475 & 0 \\ 0 & 0 & 1300 \end{bmatrix} \tag{2-39}$$

where, $[\varepsilon^T]$ is relative Permittivity, unit *F/m* (*farad/meter*).

Transferring the above properties data to stress-charge format,

$$[C]=[S_E]^{-1}=\begin{bmatrix} 1.390e+11 & 7.784e+10 & 7.428e+10 & 0 & 0 & 0 \\ 7.784e+10 & 7.428e+10 & 1.390e+11 & 0 & 0 & 0 \\ 7.428e+10 & 7.428e+10 & 1.154e+11 & 0 & 0 & 0 \\ 0 & 0 & 0 & 2.564e+10 & 0 & 0 \\ 0 & 0 & 0 & 0 & 2.564e+10 & 0 \\ 0 & 0 & 0 & 0 & 0 & 3.058e+10 \end{bmatrix} \quad (2\text{-}40)$$

where, C is the elasticity matrix, units Pa.

$$[e]=d*C=\begin{bmatrix} 0 & 0 & 0 & 0 & 14.97 & 0 \\ 0 & 0 & 0 & 14.97 & 0 & 0 \\ -5.35 & -5.35 & 15.78 & 0 & 0 & 0 \end{bmatrix} \quad (2\text{-}41)$$

where, **[e]** is the piezoelectric coupling matrix (stress –charge format), unit C/m^2 (Coulomb/meter^2).

$$\left[\varepsilon^s\right]=\left[\varepsilon^T\right]\text{-d*C*d}^{\text{T}}=\begin{bmatrix} 6.752e\text{-}09 & 0 & 0 \\ 0 & 6.752e\text{-}09 & 0 \\ 0 & 0 & 5.872e\text{-}09 \end{bmatrix} \quad (2\text{-}42)$$

where, $[\varepsilon^s]$ is electric permittivity matrix, unit F/m.

2.4.1.2 Numerical example.

Fig. 2.1 shows the BAMAFEM model. It contains 4 nodes and only 1 piezoelectric plate element. Table 2.1 lists the coordinates of each node. The thickness of the PZT element is 5.0e-4 *m*. Node 1 is constrained in X and Y directions; node 2 is constrained in the X direction. A 1.0V voltage was applied normal to the element.

Because ABAQUS does not contain 4-node piezoelectric plate with normal electric DOF, to verify the correctness of the developed 4-node piezoelectric plate element with normal electric DOF, the author used an 8-node brick piezoelectric model with normal electric DOF, the model has the same dimensions and boundary conditions as the model shown in Fig. 2.1. Fig. 2.2 shows the ABAQUS model. Nodes 1 and 5 are fixed in both X and Y directions; nodes 2 and 6 are fixed in x direction; and bottom nodes 5, 6, 7 and 8 are fixed in the z direction.

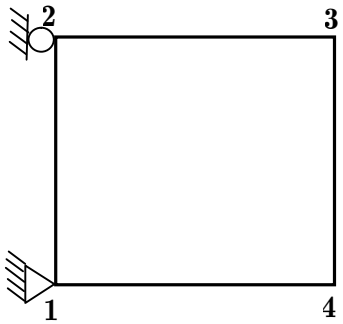

FIG. 2.1 4-node piezoelectric plate model for BAMAFEM

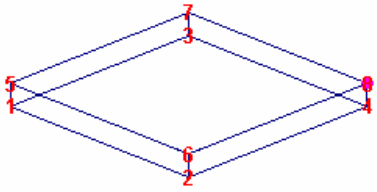

FIG. 2.2 8-node brick element model for ABAQUS

Table 2.2 lists nodal displacements calculated by BAMAFEM; Table 2.3 lists nodal displacements calculated by ABAQUS6.5. We can see that the two kinds of results are identical. Table 2.4 lists the strain results at each gauss point obtained by BAMAFEM; Table 2.5 lists the strain results calculated by ABAQUS6.5. From the displacement results and strain results obtained by BAMAFEM and those obtained by ABAQUS6.5, we can conclude that the formulation of the piezoelectric 4-node film finite element is correct.

TABLE 2.1. Nodal coordinates for Fig. 2.1 (Unit: m).

Node	Coordinate (x, y)
1	(0.0, 0.0)
2	(0.0002, 0.0)
3	(0.0002, 0.0002)
4	(0.0, 0.0002)

TABLE 2.2. Nodal displacements obtained by BAMAFEM (Unit: m).

Node	Displacements	
	u	*v*
1	-0.1765e-09	0.0000e+00
2	0.0000e+00	0.0000e+00
3	-0.1790e-23	0.1765e-09
4	-0.1765e-09	0.1765e-09

TABLE 2.3. Nodal displacements obtained by ABAQUS (Unit: m).

Node number	Displacements	
	u	v
1	-0.17655e-09	0.0000e+00
2	0.0000e+00	0.0000e+00
3	0.0000e+00	0.17655e-09
4	-0.17655e-09	0.17655e-09
5	-0.17655e-09	0.0000e+00
6	0.0000e+00	0.0000e+00
7	0.0000e+00	0.17655e-09
8	-0.17655e-09	0.17655e-09

TABLE 2.4. Strain results obtained by BAMAFEM.

Gauss Point	Strain Components			
	ε_{xx}	ε_{yy}	ε_{zz}	γ_{xy}
(0.0, 0.0)	0.88275e-07	0.88275e-07	0.11364e-06	-0.66174e-23
(-0.577, -0.577)	0.88275e-07	0.88275e-07	0.11364e-06	0.13235e-22
(-0.577, 0.577)	0.88275e-07	0.88275e-07	0.11364e-06	0.52940e-21
(0.577, -0.577)	0.88275e-07	0.88275e-07	0.11364e-06	-0.51285e-21
(0.577, 0.577)	0.88275e-07	0.88275e-07	0.11364e-06	-0.13235e-22

TABLE 2.5. Strain results obtained by ABAQUS6.5.

Node	Strain Componenets					
	E_{11}	E_{22}	E_{33}	E_{12}	E_{13}	E_{23}
1	8.8276e-8	8.8276e-8	-1.1364e-7	-1.0092e-22	4.1359e-23	8.2718e-25
2	8.8276e-8	8.8276e-8	-1.1364e-7	4.3179e-22	1.6544e-23	-1.8198e-23
3	8.8276e-8	8.8276e-8	-1.1364e-7	-9.7607e-23	3.8877e-23	-6.6174e-23
4	8.8276e-8	8.8276e-8	-1.1364e-7	4.4833e-22	3.8877e-23	-1.2739e-22
5	8.8276e-8	8.8276e-8	-1.1364e-7	-1.1084e-22	3.2260e-23	6.9483e-23
6	8.8276e-8	8.8276e-8	-1.1364e-7	4.3510e-22	2.5643e-23	8.2718e-25
7	8.8276e-8	8.8276e-8	-1.1364e-7	-1.1911e-22	3.3087e-24	-3.3087e-24
8	8.8276e-8	8.8276e-8	-1.1364e-7	4.3675e-22	3.3087e-24	-1.1829e-22

2.4.2 Experimental verification

Two experiments were made to verify the correctness of piezoelectric element plate element developed by the author. One experiment was done by Nistorica,[8] it was used to verify the correctness of the output displacement results.. Jian Zhong performed another experiment it was used to verify the correctness of the output voltage results.

2.4.2.1 Experimental materials and their properties.

The experimental samples consist of two kinds of materials, Silicon and PNZT. The properties of Silicon are as follows:[9]

Density: ρ = 2330kg/m^3
Poisson's ratio: υ = 0.17
Young's modulus: E = 150 GPa
The coefficient of thermal expansion: α = 2.7e-6

The Material properties of PNZT were measured by Nistorica. They are listed as follows:

Elasticity matrix (unit: *Pa*):

$$[C]=\begin{bmatrix} 1.21e+11 & 7.54e+10 & 7.52e+10 & 0 & 0 & 0 \\ 7.54e+10 & 7.52e+10 & 7.52e+10 & 0 & 0 & 0 \\ 7.52e+10 & 7.52e+10 & 1.11e+11 & 0 & 0 & 0 \\ 0 & 0 & 0 & 2.11e+10 & 0 & 0 \\ 0 & 0 & 0 & 0 & 2.11e+10 & 0 \\ 0 & 0 & 0 & 0 & 0 & 2.26e+10 \end{bmatrix}$$

Piezoelectric coupling matrix (stress –charge format) (unit: *Coulomb/m*^{2}):

$$[e] = \begin{bmatrix} 0 & 0 & 0 \\ 0 & 0 & 0 \\ -5.4 & -5.4 & 0 \end{bmatrix}$$

Electric permittivity matrix (unit: *Farad/meter*):

$$\left[\varepsilon^s\right] = \begin{bmatrix} 6.752\text{e-}09 & 0 & 0 \\ 0 & 6.752\text{e-}09 & 0 \\ 0 & 0 & 5.872\text{e-}09 \end{bmatrix}$$

2.4.2.2 Sample and cantilever preparation and measurement setup.

Nb-doped lead zirconate titanate (PNZT) films were prepared by using a sol-gel technique. The detail of the film process is described by Han *et al.*[10] The substrate is Pt(150 nm)/TiO_x(40 nm)/SiO_2(500 nm)/Si(400 μm)/SiO_2(500 nm)/TiO_x(40 nm)/Pt(150 nm). The PNZT films were coated on both sides of the wafer. The typical solution composition is $Pb_{12}(Zr_{0.2}Ti_{0.8})O_3$ with 2% Nb, which was named PNZT(2/20/80). Using a steel wire saw with diamond-embedded cut the cantilevers. Wet etching was used to remove PNZT film to expose the bottom electrode. The thickness of PNZT(2/20/80) was 650 nm, which was measured by using a Dektak profilometer. The top electrode Pt with a square area was deposited by magnetron sputtering with a shadow mask. A fine silver wire was glued to the bottom and top electrodes by using silver epoxy. The PNZT films were poled under a field of 250 kV/cm by using 60,000 pulses with the duration of 0.01 ms. X-ray diffraction (XRD) result shows that PNZT(2/20/80) film has a random orientation with major (111), (110) and minor (100) peaks.

Fig. 2.3 and Fig. 2.4c show the dimensions of the experimental samples. Fig. 2.4a,b and Fig. 2.5 show the experimental setup to measure the response of PNZT film as a sensor and an actuator. For the sensor measurement shown in Fig. 2.4a, the idea of the cantilever setup is the same as that proposed by Dubois and Muralt.[11] A bulk PNZT actuator was used to drive the cantilever beam from the top at a certain frequency, a charge amplifier was used to collect the charge on the top electrode. Here a preamplifier and lock-in amplifier were used to make sure that only the signal with the driving frequency was selected and measured. An optical sensor was used to measure the deflection at the driving point from the other side of the cantilever. An oscilloscope was used to monitor the signals. For the actuator measurement shown in Fig. 2.4a, a certain frequency AC voltage was used to drive the cantilever from the top and bottom electrodes, and then detect the deflection of the free end of the cantilever by an optical sensor. For one cantilever, there are two capacitors: one in the front side facing the optical sensor and another in the backside.

2.4.2.3 Actuating mode measurement.

Dimensions of the measured beam are shown in Fig. 2.3, point A is the location where displacement is measured. The thickness of the beam is 0.7mm, and the thickness of the PNZT film is 1μm. In this experiment, the driving AC voltage on the back side capacitor is (3.5*sin(6πt)+3.5)volt. The amplitude of deflection measured at the point of L = 27.5 mm is 1.12014 $\times 10^{-7}$m.

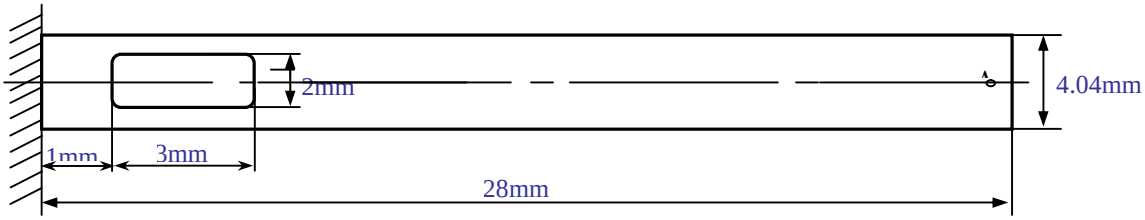

FIG 2.3. Dimensions of the beam for actuating mode measurement

2.4.2.4 Sensing mode measurement.

Fig. 2.4c shows the geometric definition of the measured cantilever beam. The total length *L* of the cantilever made from PNZT(2/20/80) is 34.3 mm, the width *b* of the cantilever is 2.5 mm, the thickness *h* of Si substrate is 0.4 mm. The thickness of PNZT film is 650 nm. The top electrode Pt is a square of 1 mm x 1 mm and its thickness is about 100 nm. The distance x_1 from the electrode front edge to the base is 4.45 mm.

For the sensor measurement, the distance L_d from the bulk PNZT driving point to the base is 23.3 mm. The driving AC voltage of the bulk PNZT actuator is 5*sin(2πft) volt with a frequency f of 10 Hz. The deflection amplitude measured at the driving point is 369.3 nm. The charge amplitude measured from the front side capacitor is (0.70±0.01) pC. The capacitance of the electrode is 7.49 nF. So the voltage on the electrode due to the charge is about 0.09 mV, while for the backside capacitor the charge amplitude is (0.93±0.02) pC. The voltage on the electrode due to the charge is about 0.12 mV.

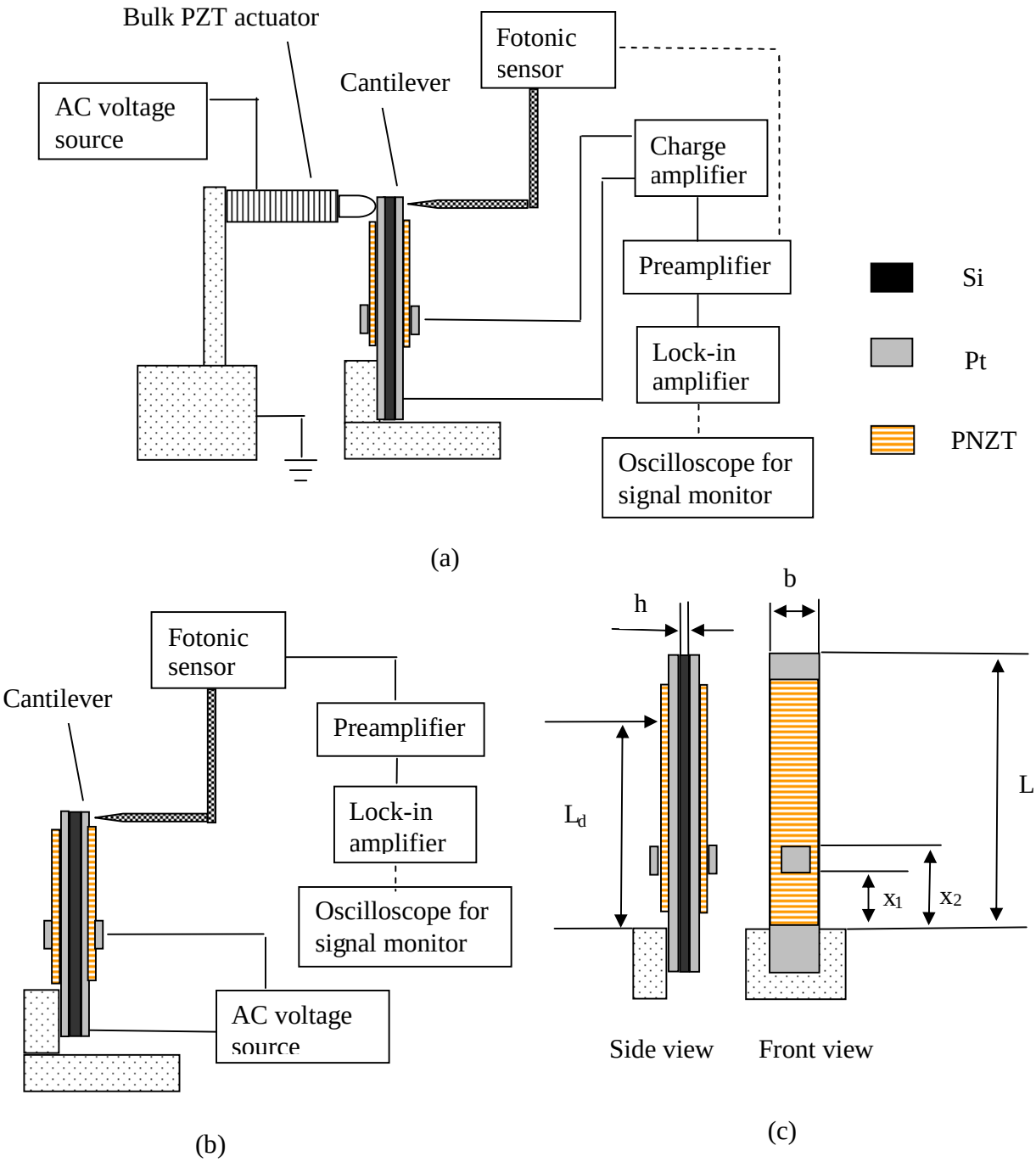

Figs 2.4 (b) drawing for actuating mode measurement; (c) a cantilever geometry; (d) a picture of the setup.

FIG. 2.5. Photograph of experimental setup.

2.4.2.5 Texture effect on piezoelectric response.

Ledermann *et al.* has already shown that the value of the piezoelectric coefficients of PZT films have very strong dependence on the texture of the film even when the composition and the thickness are kept the same.[12] The PZT film with (100) texture may have a piezoelectric response of twice that of the film with (111) texture. Their results agree with the theoretical calculation very well.[13,14] The sensing mode measurement here shows two different values between the front side PNZT capacitor (0.70 pC) and the back side one (0.93 pC). The possible reason is that the textures of the films on two sides are different. Simulation result for the film will be more accurate if the texture effect is included in the model.

2.4.3 BAMAFEM results

2.4.3.1 BAMAFEM results for actuating mode

To consider the convergence of the calculation results, 4 different mesh models are constructed. Mesh 1 shown in Fig. 2.6 contains 320 nodes; and consists of 12 piezoelectric 4-node thin film elements and 124 8-node brick elements. Fig. 2.7 shows the calculated dynamic response at measurement point A (shown in Fig. 2.3). From the figure, we can see that it took about 1800 time steps to converge to the steady state result. It is believe that the reason is because the precision of the stiffness matrix and the mass matrix are not enough.

Mesh 2 shown in Fig. 2.8 contains 480 nodes; and consists of 12 piezoelectric 4-node thin film elements and 248 8-node brick elements. Fig. 2.9 shows the calculated dynamic response at measurement point A for the mesh.

Mesh 3 (shown in Fig. 2.10) contains 1116 nodes; and consists of 24 piezoelectric 4.node thin film elements and 488 8-node brick elements. The curve shown in Fig. 2.11 is the calculated dynamic response at measurement point A corresponding to the mesh.

Mesh 4 (shown in Fig. 2.12) contains 1674 nodes; and consists of 24 piezoelectric 4-node thin film elements and 976 8-node brick elements. Fig. 2.13 shows the calculated dynamic response at measurement point A.

Table 2.6 lists the first two natural frequencies for each mesh. Table 2.7 lists the calculated dynamic response at the same location for different meshes.

TABLE 2.6. Natural frequencies for various meshes.

Mesh Cases	Natural frequencies (Unite: Hz)		
	f_1	f_2	f_3
Mesh 1	1.4940E+03	6.6638E+03	9.7452E+03
Mesh 2	1.4814E+03	6.6628E+03	9.6833E+03
Mesh 3	1.2791E+03	6.6068E+03	7.9827E+03
Mesh 4	1.2662E+03	6.6058E+03	4.9709E+04

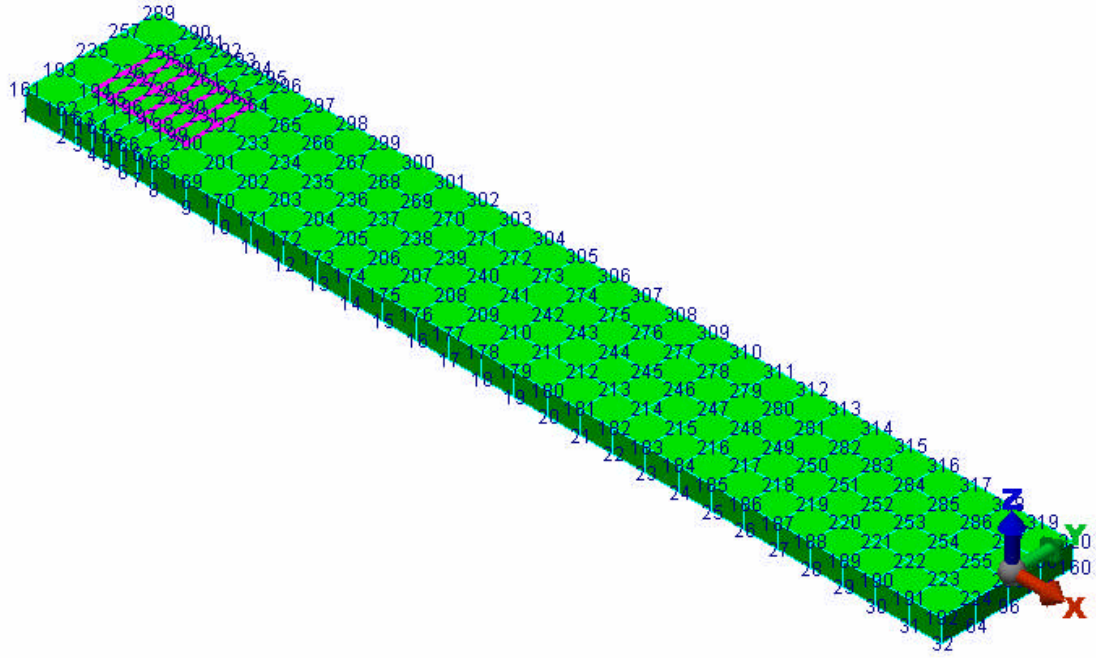

FIG. 2.6. FEA mesh 1 of cantilever beam for actuating mode.

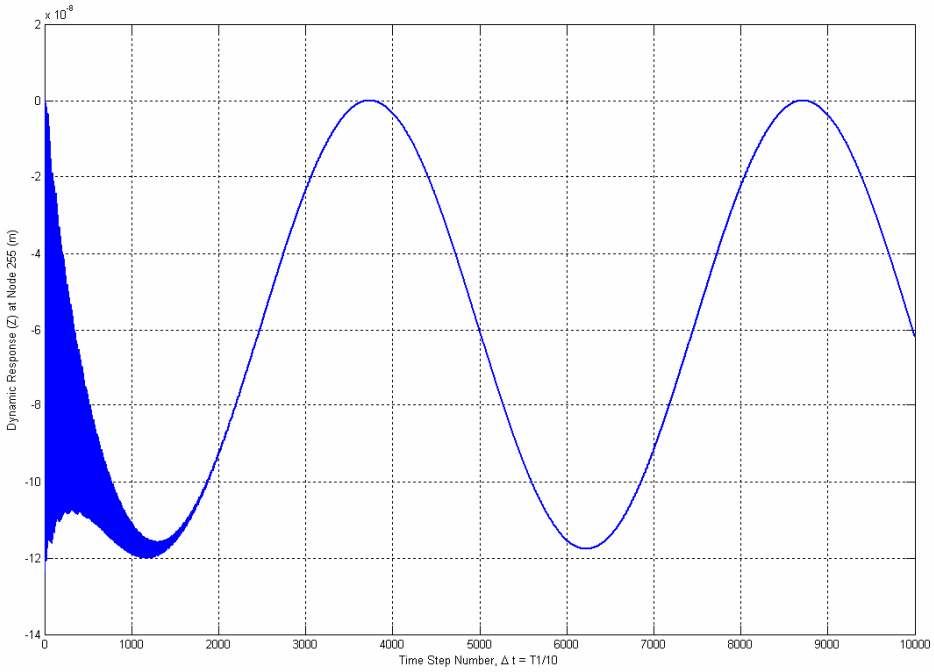

FIG. 2.7. Dynamic responses of mesh 1 at node 255.

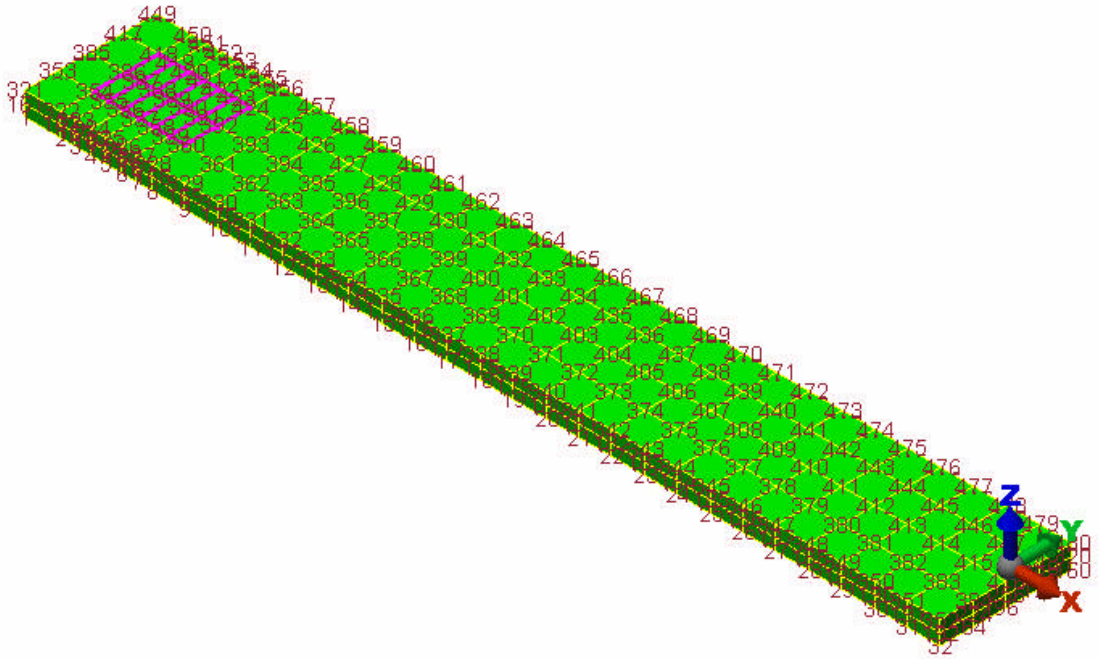

FIG. 2.8. FEA mesh 2 of cantilever beam for actuating mode.

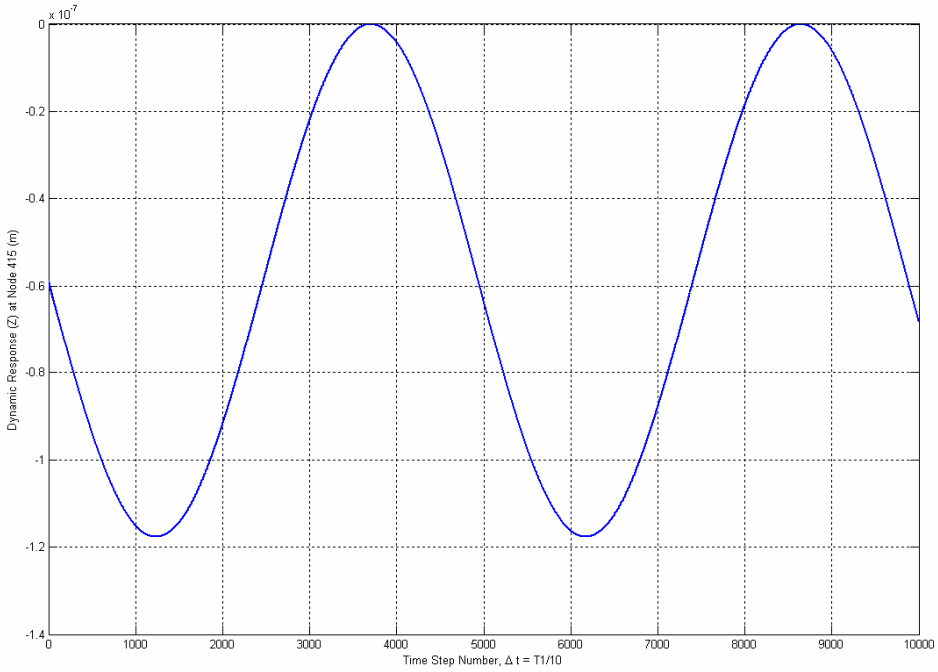

FIG. 2.9. Dynamic responses of mesh 2 at node 415.

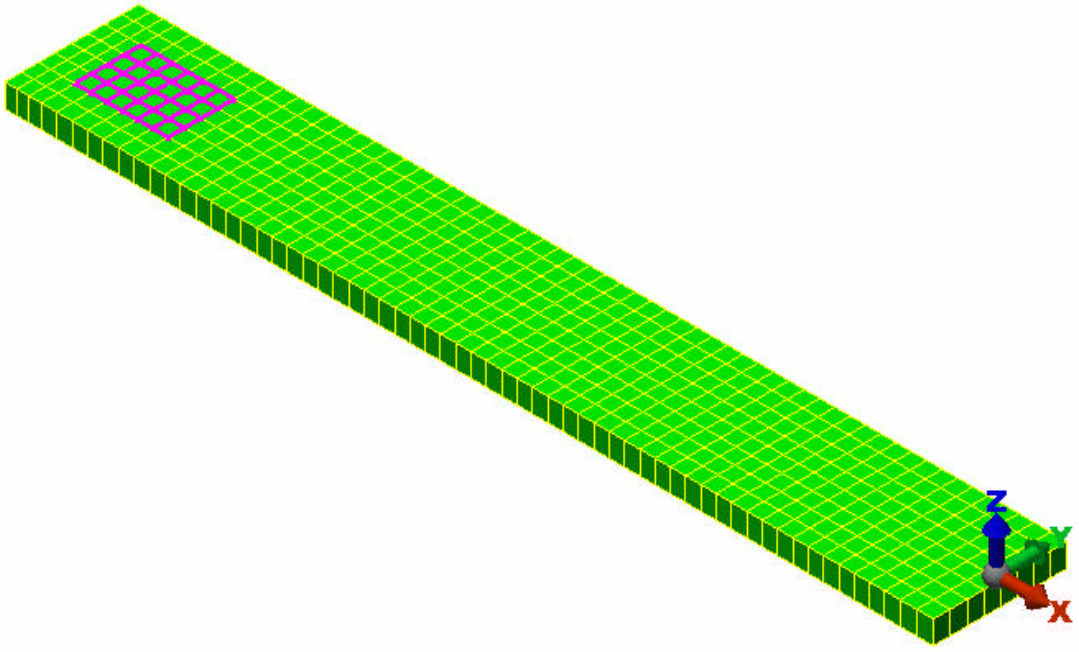

FIG. 2.10. FEA mesh 3 of cantilever beam for actuating mode.

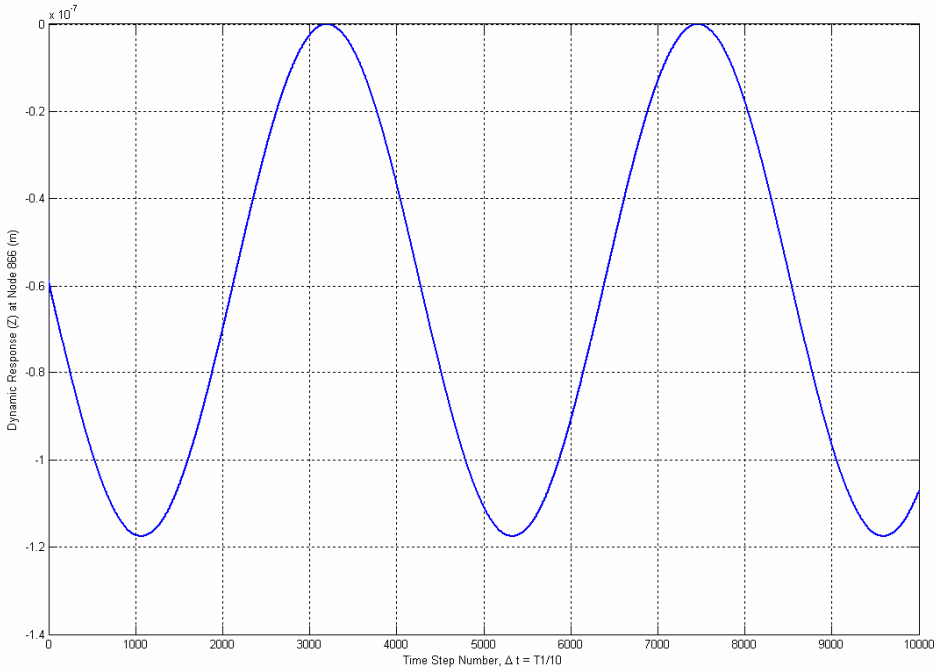

FIG. 2.11. Dynamic responses of mesh 3 at node 866.

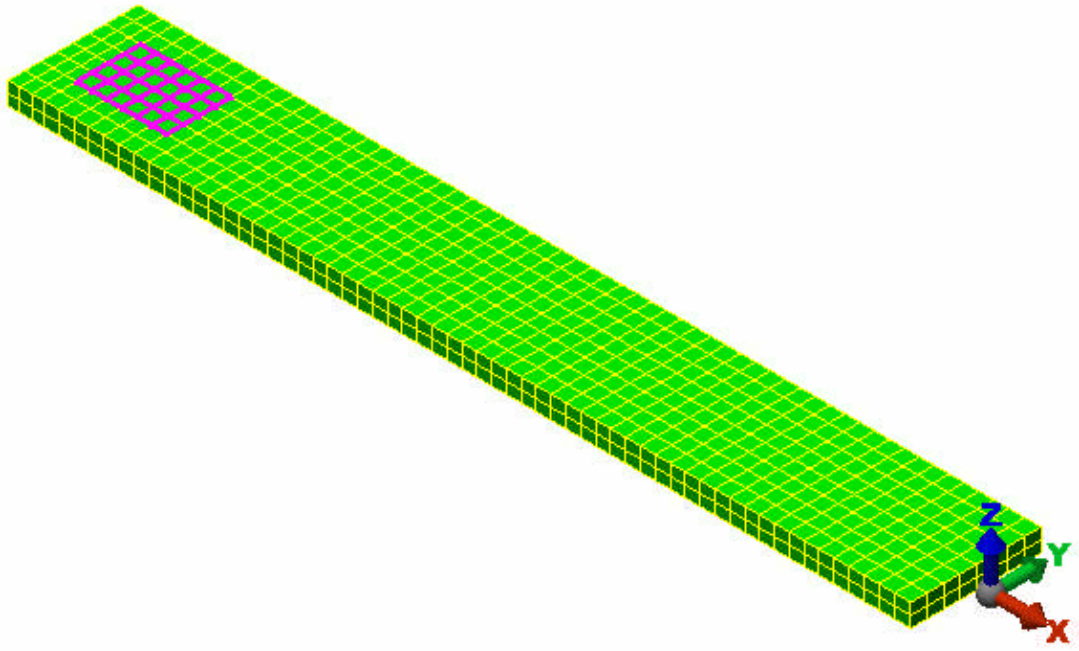

FIG. 2.12. FEA mesh 4 of the cantilever beam for actuating mode.

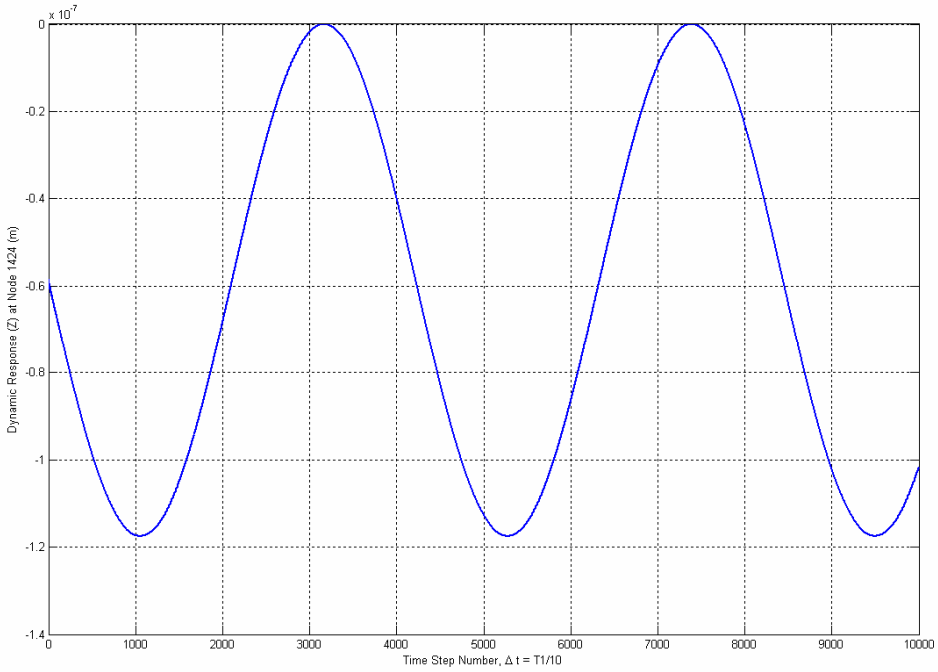

FIG. 2.13. Dynamic responses of mesh 4 at node 1424.

TABLE 2.7. Maximum displacements for different mesh.

Cases	Dsplacements (Z) (Unit: m)
Experiment	1.12014×10^{-7}
Mesh 1	1.1765×10^{-7}
Mesh 2	1.1764×10^{-7}
Mesh 3	1.1751×10^{-7}
Mesh 4	1.1749×10^{-7}

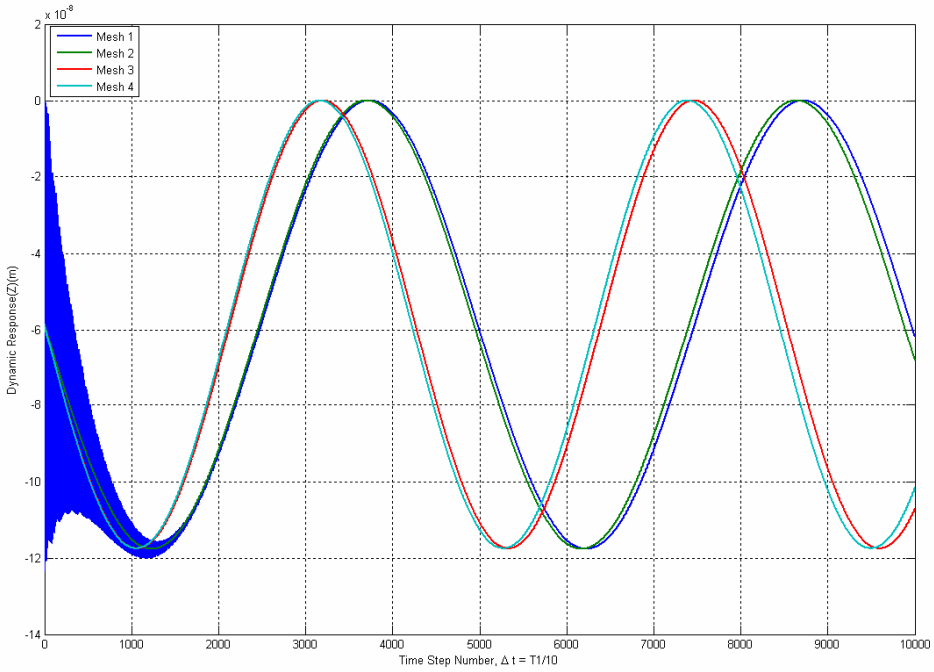

FIG. 2.14. Comparison of dynamic response for different mesh.

Fig. 2.14 shows the comparison of dynamic response for different meshes at the same location when 7V voltage is applied. The calculated maximum value is 1.1765×10^{-7}. The experimental measurement result is 1.12014×10^{-7}m. Comparing calculated results and experimental results, theoretical results are larger by 5.03% than experimental values; the maximum dynamic responses for different meshes are almost the same, the main difference is the phase, the reason is that the natural frequencies are sensitive to mesh. Also, the Newmark method for time history computation exhibits phase errors for unconverged models. It can be concluded that the two results match very well.

2.4.3.2 BAMAFEM results for sensing mode.

Because the dynamic responses are nearly the same for different meshes of the structure, the author constructed only one mesh to analyze the sensing mode. Fig. 2.15 shows the FEA model used to compute for the sensing mode. The mesh contains 602 nodes, 4 piezoelectric plate elements and 252 8-node non-conforming 8-node brick elements.

TABLE 2.8. Output voltage in the sensor elements.

Element	Output Voltage (mV)
1	0.0933
2	0.0934
3	0.866
4	0.0868

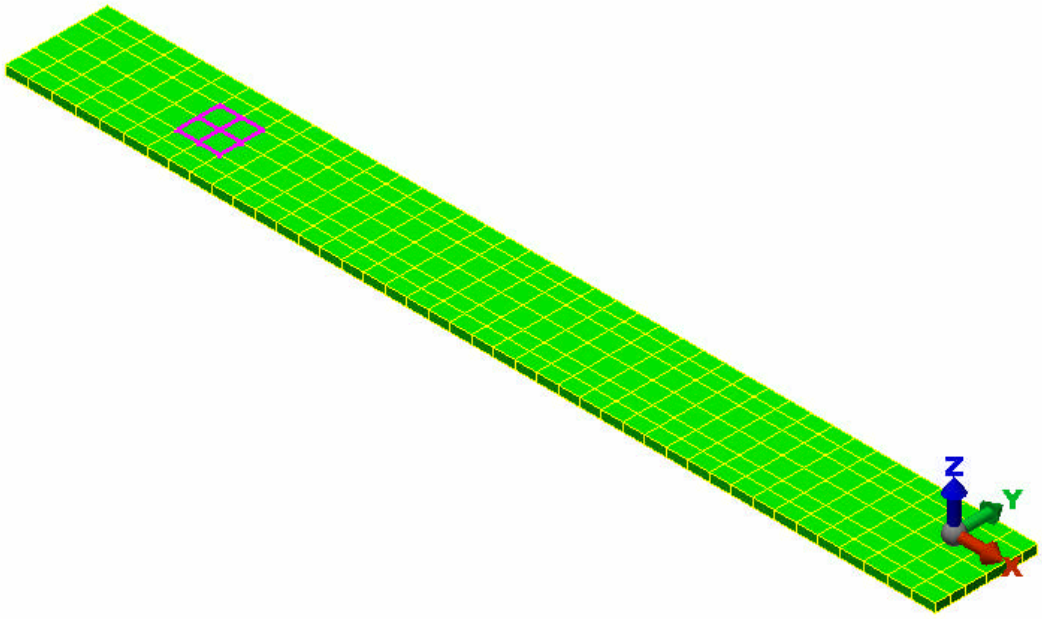

FIG. 3.15. FEA mesh of cantilever beam for sensing mode.

Table 2.8 lists the output voltages in the 4 PNZT elements obtained by BAMAFEM. Because the strains in the sensor elements that are close to the end of the beam are larger than that of other two sensor elements, their output voltages are larger. The average output voltage in the 4 PNZT elements is 0.09 mV. So, the computational results match the experimental result (0.09mV) very well.

2.5 Inclusion of Coriolis Effect into the Finite Element Software

If a dynamic system is in equilibrium, the sum of the external and internal virtual work is zero. Mathematically, we state this as

$$\int_V \{\delta u\}^T [f^b] dV + \int_S \{\delta u\}^T [f^s] dS + \sum_{i=1}^{n} \{\partial u_i\}^T [p_i] - \int_V (\{\delta\varepsilon\}^T [\sigma] + \{\delta u\}^T \rho [\ddot{u}] + \{\delta u\}^T c [\dot{u}]) dV - \int_V \{\delta u\}^T \rho \{a_c\} dV = 0 \quad (2\text{-}43)$$

The first three terms account for the virtual work of the body, surface, and concentrated forces, respectively. Terms four, five and six represent the virtual work of the internal stresses, inertial forces, and viscous forces. The quantity δu indicates virtual displacement, u is displacement, and $\delta\varepsilon$ is virtual strain. The quantity ρ is mass density and c is a measure of viscous damping. The first six terms lead to the well-known result:

$$[M]\{\ddot{d}\} + [C]\{\dot{d}\} + [K]\{d\} = \{F(t)\} \quad (2\text{-}44)$$

where {d} is the nodal displacement vector. For example, for an 8-node hexahedron, this would be

$$\{d\}^T = \begin{bmatrix} d_{1x} & d_{1y} & d_{1z} & d_{2x} & d_{2y} & d_{2z} & \cdots & d_{8x} & d_{8y} & d_{8z} \end{bmatrix} \quad (2\text{-}45)$$

The last (seventh) term in equation (2-43) is the virtual work resulting from the Coriolis acceleration of the body, where a_c is Coriolis acceleration. The figure below indicates a coordinate system fixed in a rotating rigid body. Let the angular rate of the body be given by

$$\vec{\Omega} = \Omega_x \hat{i} + \Omega_y \hat{j} + \Omega_z \hat{k} \tag{2-46}$$

where the i, j, and k are unit vectors.

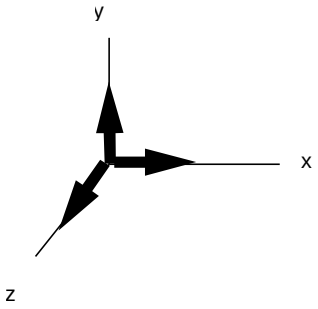

Figure 2.16. Angular rate vector for a rotating rigid body

Now the Coriolis acceleration represents the interaction between the angular rate of rotation of the rigid body and the velocity of a point relative to the body. It is given by

$$\vec{a}_c = 2\vec{\Omega} \times \dot{\vec{u}} \tag{2-47}$$

In expanded form this is

$$\begin{Bmatrix} a_x \\ a_y \\ a_z \end{Bmatrix} = \begin{bmatrix} 0 & -2\Omega_z & 2\Omega_y \\ 2\Omega_z & 0 & -2\Omega_x \\ -2\Omega_y & 2\Omega_x & 0 \end{bmatrix} \begin{Bmatrix} \dot{u}_x \\ \dot{u}_y \\ \dot{u}_z \end{Bmatrix} \tag{2-48}$$

Now substituting this into the seventh term of equation (2-43) gives, after replacing the continuous velocity components with the usual finite element discretization,

$$\int_V \{\delta d\}^T \rho \{a_c\} dV = \int_V \{\delta d\}^T [N]^T \rho [\Omega][N] \{\dot{d}\} dV \tag{2-49}$$

The [N] is the matrix of finite element shape functions. For example, for an eight node hexahedron, N has dimensions 3 x 24. After dropping the common virtual displacement term, we obtain the following modification to equation (2-44):

$$[M]\{\ddot{d}\} + [C]\{\dot{d}\} + [COR]\{\dot{d}\} + [K]\{d\} = \{F(t)\} \tag{2-50}$$

where the additional term comes from

$$\left[COR\right] = \int_V \rho \left[N\right]^T \left[\Omega\right]\left[N\right]\left\{\dot{d}\right\} dV \tag{2-51}$$

The Coriolis matrix $\left[COR\right]$ has precisely the same form as the well-known finite element mass matrix $\left[M\right]$ except for the presence of the $\left[\Omega\right]$ matrix.

There are at least three ways to incorporate the Coriolis effect into an analysis. First, the elemental finite element equations can remain in the form of equation (2-50) and the usual procedure of assembly, application of Dirichlet boundary conditions, and implementation of a time integration scheme will yield a solution for the dynamic response. Unfortunately, $\left[\Omega\right]$ is skew-symmetric. Thus, the resulting matrix $\left[COR\right]$ and the assembled global finite element equations will not be symmetric. This will preclude the economy of using a symmetric storage scheme and a symmetric equation solver, as is normally the case in finite element analysis. This would be a severe penalty in storage and computational time.

Another approach would be to treat the Coriolis effect as an applied force; thus, the Coriolis force is given by

$$\left\{ f^c \right\} = -\left[COR\right]\left\{\dot{d}\right\} \tag{2-52}$$

The governing elemental equations now take the form

$$\left[M\right]\left\{\ddot{d}\right\} + \left[C\right]\left\{\dot{d}\right\} + \left[K\right]\left\{d\right\} = \left\{F(t)\right\} + \left\{ f^c \right\} \tag{2-53}$$

where the Coriolis effect is treated as an additional applied force. The difficulty with this is that while the angular rates are prescribed, the velocity vector $\left\{\dot{d}\right\}$ is unknown. We can deal with this in one of two ways. First, we can solve the assembled finite element equations iteratively at each time increment of the dynamic analysis. That is,

$$\left[M\right]\left\{\ddot{d}\right\}^{i+1} + \left[C\right]\left\{\dot{d}\right\}^{i+1} + \left[K\right]\left\{d\right\}^{i+1} = \left\{F(t)\right\}^{i+1} + \left\{ f^c \right\}^{i} \tag{2-54}$$

where the superscripts i and i+1 refer to iterations. The Coriolis force is evaluated from

$$\left\{ f^c \right\}^{i} = -\left[COR\right]\left\{\dot{d}\right\}^{i} \tag{2-55}$$

When displacement and velocity vectors (or suitable norms) have changed by less than a prescribed quantity between successive iterations, convergence has been achieved. To avoid the expensive iterations at each time step, an alternative is to evaluate the Coriolis force vector using the values for the velocities at the previous time increment. In other words equation (2-54) is solved only once at each time increment and the value of the Coriolis force $\left\{ f^c \right\}^{i}$ is evaluated using the velocity vector obtained for the previous time increment. This will result in the application of Coriolis forces that lag the actual forces by one time increment. This means, for example, that if the time increment is taken as 1/10 of the period of the actuating signal, the applied Coriolis forces will lag the actual values by that same time. This is the method implemented in the current version of the BAMAFEM code and we believe it to be an acceptable model for use in simulating gyroscope behavior.

3. FINITE ELEMENT SIMULATION OF THE X-POST GYROSCOPE

3.1 Summary

The theory and verification studies for the simulation code developed for the gyro project were presented in Chapter 2. After verification the code was used to design a configuration that would oscillate at the desired frequency. The code was also used for risk management in that magnitudes of deformations and voltage output which could theoretically be obtained from the design were computed. These results showed that signal output could be large enough to accurately measure. The simulation did not, however, include the effects of electronic noise. The effects of imperfections in manufacture and of thermal changes were also studied. Just as has been noted experimentally by other investigators, the effects on device accuracy of temperature changes during operation were found to be severe. Imperfections were harmful, as well, but not nearly as important as thermal effects. These gyro simulation studies suggest that the developed simulation capability could be used in the future to improve gyro design through use of various materials and/or geometric changes

3.2 Modeling of a MEMS-technology gyroscope

3.2.1 Governing equation of motion

The gyroscope system can be represented by the following governing equation

$$[M]\{\ddot{U}\}+[C]\{\dot{U}\}+[K]\{U\}=\{F\} \tag{3-1}$$

where coefficient $[M]$, $[C]$, $[K]$ represent the global mass, damping and stiffness matrices respectively. Vector $\{F\}$ is the system force vector. Matrix $[C]$ can be obtained by equation

$$[C]=\alpha[M]+\beta[K] \tag{3-2}$$

where α and β are the mass and stiffness proportional damping constants. The relationship between α , β and the fraction of critical damping ξ at frequency ω is given by the following equation[4]

$$\xi=\frac{1}{2}\left(\alpha\omega+\frac{\beta}{\omega}\right) \tag{3-3}$$

α , β can be determined by choosing the fractions of critical damping (ξ_1 and ξ_2) at two different frequencies (ω_1 and ω_2). By solving the following equations, α and β can be obtained

$$\left.\begin{aligned}\alpha &= 2\omega_1\omega_2(\xi_1\omega_2-\xi_2\omega_1)/(\omega_2^2-\omega_1^2)\\ \beta &= 2(\xi_2\omega_2-\xi_1\omega_1)/(\omega_2^2-\omega_1^2)\end{aligned}\right\} \tag{3-4}$$

3.2.2 Formulation of force vector

For non-inertial reference frames, considering the effects of temperature, the force vector applied to a strap down MEMS-technology gyroscope can be described as follows:

$$\{F\}=\{F_T\}+\{F_P\}+\{F_I\} \tag{3-5}$$

where $\{F_T\}$, $\{F_P\}$ and $\{F_I\}$ are the thermal force vector, piezoelectric force vector and inertial force vector, respectively. $\{F_P\}$ can be obtained by equation (2-29).

3.2.2.1 Thermal force vector.

Since the X-post gyroscope is modeled with 4-node piezoelectric thin film elements and 8-node nonconforming brick elements, the thermal force can be decomposed into

$$\{F_T\} = \{F_{T1}\} + \{F_{T2}\} \tag{3-6}$$

For 4-node piezoelectric thin film elements, the thermal force induced due to thermal change is

$$\{F_{T1}\} = t\int_{-1}^{1}\int_{-1}^{1}[B_u]^t[C]\{\in_{T1}\}|J|drds \tag{3-7}$$

where $[B_u]$ can be obtained by equation (2-13); $[C]$ can be determined by equations (2-8) to (2-10); and $\{\in_{T1}\}$ is the pre-strain vector induced by thermal difference.

$$\{\in_{T1}\} = \begin{Bmatrix}\in_{xx}\\ \in_{yy}\\ \gamma_{xy}\end{Bmatrix} = \begin{Bmatrix}\alpha_1\Delta T\\ \alpha_1\Delta T\\ 0\end{Bmatrix} \tag{3-8}$$

In equation (3-7), α_1 is the coefficient of thermal expansion of the material. For 8-node nonconforming brick elements, the thermal force induced due to thermal change is

$$\{F_{T2}\} = \int_{-1}^{1}\int_{-1}^{1}\int_{-1}^{1}[B_u]^t[C]\{\in_{T2}\}|J|drdsdt \tag{3-9}$$

In the thesis by G. Huang,[9] details are offered about how to obtain [B_u]; $\{\in_{T1}\}$ is the pre-strain vector induced by thermal difference.

$$\{\in_{T2}\} = \begin{Bmatrix}\in_{11}\\ \in_{22}\\ \in_{33}\\ \gamma_{12}\\ \gamma_{23}\\ \gamma_{13}\end{Bmatrix} = \begin{Bmatrix}\alpha_2\Delta T\\ \alpha_2\Delta T\\ \alpha_2\Delta T\\ 0\\ 0\\ 0\end{Bmatrix} \tag{3-10}$$

In equation (3-10), α_2 is the coefficient of thermal expansion of the material.

3.2.2.2 Inertial vector.

In strapdown systems the gyroscopes are fixed to the vehicle (a rotating frame *Oxyz*) and rotate with its angular rate Ω.[15] For a frame shown in Fig 3-5, $\{F_I\}$ are the inertial forces due to the motion of the vehicle given by equation (3-11)

$$\{F_I\} = M\ddot{R} - M\Omega\times(\Omega\times U) - 2M\Omega\times\dot{U} - M\dot{\Omega}\times U \tag{3-11}$$

where *M, R(t), Ω(t), U(t)* is system mass matrix, vehicle position vector (Frame O*xyz* relative to frame OXYZ), angular frequency vector and node position vector, respectively. The terms on the right side of equation (3-11) correspond to translational, centrifugal, Coriolis, and transverse forces, respectively. To verify the correctness, a simple case was considered, i.e., the vehicle is static. In this

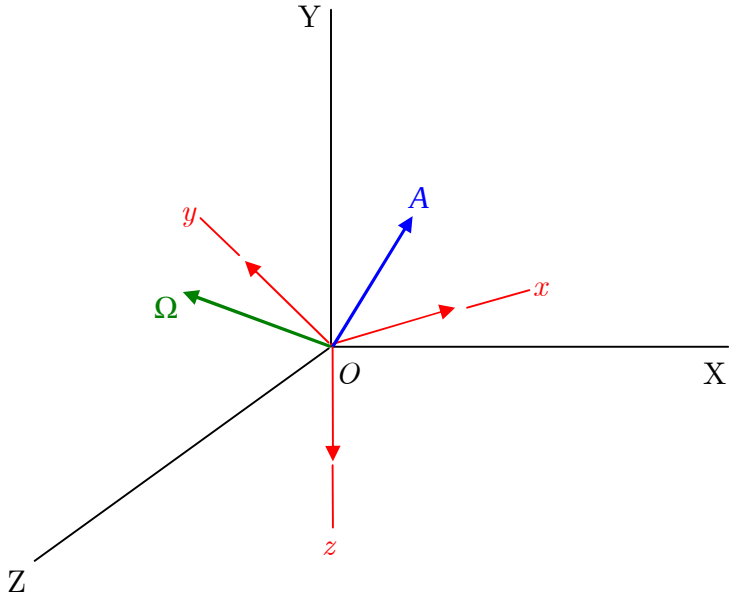

FIG. 3.5. Motion frame for X-post gyroscope.

case the first term in equation (3-11) equals zero. In the present application $U \ll \dot{U}$ and $\dot{\Omega}$ is very small. Then the second term and the fourth term in equation (3-11) is much smaller than its third term. So, only the Coriolis force is considered as the inertial force. Then,

$$\{F_I\} \approx -2M\,\Omega \times \dot{U} \tag{3-12}$$

For any element in a MEMS gyroscope, the velocity vector can be represented:

$$\vec{v} = v_x\vec{i} + v_y\vec{j} + v_z\vec{k} \tag{3-13}$$

and the rotation vector is:

$$\vec{\Omega} = \Omega_x\vec{i} + \Omega_y\vec{j} + \Omega_z\vec{k} \tag{3-14}$$

The Coriolis acceleration vector is:

$$\vec{a}_c = 2\vec{\Omega}\times\vec{v} = \begin{vmatrix} \vec{i} & \vec{j} & \vec{k} \\ 2\Omega_x & 2\Omega_y & 2\Omega_z \\ v_x & v_y & v_z \end{vmatrix} = \begin{vmatrix} 2\Omega_y & 2\Omega_z \\ v_y & v_z \end{vmatrix}\vec{i} - \begin{vmatrix} 2\Omega_x & 2\Omega_z \\ v_x & v_z \end{vmatrix}\vec{j} + \begin{vmatrix} 2\Omega_x & 2\Omega_y \\ v_x & v_y \end{vmatrix}\vec{k}$$

$$\vec{a}_c = (2\Omega_y v_z - 2\Omega_z v_y)\vec{i} + (2\Omega_z v_x - 2\Omega_x v_z)\vec{j} + (2\Omega_x v_y - 2\Omega_y v_x)\vec{k} \tag{3-15}$$

Also, $\vec{a}_c = a_{cx}\vec{i} + a_{cy}\vec{j} + a_{cz}\vec{k}$

Then, $a_{cx} = (2\Omega_y v_z - 2\Omega_z v_y)$ $a_{cy} = (2\Omega_z v_x - 2\Omega_x v_z)$ $a_{cz} = (2\Omega_x v_y - 2\Omega_y v_x)$ (3-16)

Using matrix form, the components of $\vec{a}_c$ can be written as follows:

$$\begin{Bmatrix} a_{cx} \\ a_{cy} \\ a_{cz} \end{Bmatrix} = 2\begin{bmatrix} 0 & -\Omega_z & \Omega_y \\ \Omega_z & 0 & -\Omega_x \\ -\Omega_y & \Omega_x & 0 \end{bmatrix}\begin{Bmatrix} v_x \\ v_y \\ v_z \end{Bmatrix} = 2\begin{bmatrix} 0 & -\Omega_z & \Omega_y \\ \Omega_z & 0 & -\Omega_x \\ -\Omega_y & \Omega_x & 0 \end{bmatrix}\begin{Bmatrix} \dot{u} \\ \dot{v} \\ \dot{w} \end{Bmatrix} \tag{3-17}$$

For an 8-node non-conforming brick element,

$$\begin{Bmatrix} \dot{u} \\ \dot{v} \\ \dot{w} \end{Bmatrix} = \sum_{i=1}^{8} N_i \begin{Bmatrix} \dot{u}_i \\ \dot{v}_i \\ \dot{w}_i \end{Bmatrix} \tag{3-18}$$

So, the Coriolis force can be represented as[16]

$$F_c = \int_V \rho a_c dV = 2\int_V [N]^T \rho [\Omega][N]\{\dot{U}\} dV \tag{3-19}$$

Then, the Coriolis force can be obtained by equation

$$F_c = \sum_{i=1}^{3}\sum_{j=1}^{3}\sum_{k=1}^{3} w_i w_j w_k (\det J)_{ijk} \rho N_{ijk}^T [\Omega] N_{ijk} \{\dot{U}\} \tag{3-20}$$

where,
$$[\Omega] = \begin{bmatrix} 0 & -\Omega_z & \Omega_y \\ \Omega_z & 0 & -\Omega_x \\ -\Omega_y & \Omega_x & 0 \end{bmatrix} \tag{3-21}$$

$$[N] = \begin{bmatrix} N_1\ 0\ 0\ N_2\ 0\ 0\ N_3\ 0\ 0\ \ldots\ldots\ N_8\ 0\ 0 \\ 0\ N_1\ 0\ 0\ N_2\ 0\ 0\ N_3\ 0\ \ldots\ldots\ 0\ N_8\ 0 \\ 0\ 0\ N_1\ 0\ 0\ N_2\ 0\ 0\ N_3\ \ldots\ldots\ 0\ 0\ N_8 \end{bmatrix} \tag{3-22}$$

$$\{\dot{U}\} = \begin{Bmatrix} \dot{u}_1 \\ \dot{v}_1 \\ \dot{w}_1 \\ \vdots \\ \vdots \\ \dot{u}_8 \\ \dot{v}_8 \\ \dot{w}_8 \end{Bmatrix} \tag{3-23}$$

3.3 Solution of the equations of motion

The equation of motion of a typical dynamic system is given as follows:

$$[M]\{\ddot{U}\} + [\alpha M + \beta K]\{\dot{U}\} + [K]\{U\} = \{F\} \tag{3-24}$$

The above equations may be solved by in-core or out-of-core solvers, normally versions of Gaussian elimination. In this work we have used both of these plus an iterative conjugate gradient method.

Writing the equation of motion for a single element by the differential form at both the "0" and "1" stations (time steps) gives:[17]

$$M\frac{d^2U_0}{dt^2} + (\alpha M + \beta K)\frac{dU_0}{dt} + KU_0 = F_0 \tag{3-25}$$

$$M\frac{d^2U_1}{dt^2} + (\alpha M + \beta K)\frac{dU_1}{dt} + KU_1 = F_1 \tag{3-26}$$

Perform linear interpolation in time for the Newmark method, giving

$$U_1 = U_0 + \frac{\Delta t}{2}\left(\frac{dU_0}{dt} + \frac{dU_1}{dt}\right) \tag{3-27}$$

$$\frac{dU_1}{dt} = \frac{dU_0}{dt} + \frac{\Delta t}{2}\left(\frac{d^2U_0}{dt^2} + \frac{d^2U_1}{dt^2}\right) \tag{3-28}$$

Rearrangement of the above four equations leads to the following three equations:

$$\left[\left(\alpha+\frac{2}{\Delta t}\right)M+\left(\beta+\frac{\Delta t}{2}\right)K\right]U_1=\frac{\Delta t}{2}(F_0+F_1)+\left(\alpha+\frac{2}{\Delta t}\right)MU_0+2M\frac{dU_0}{dt}+\left[\beta-\frac{\Delta t}{2}\right]KU_0 \tag{3-29}$$

$$\frac{dU_1}{dt}=\frac{2}{\Delta t}(U_1-U_0)-\frac{dU_0}{dt} \tag{3-30}$$

$$\frac{d^2U_1}{dt^2}=\frac{2}{\Delta t}\left(\frac{dU_1}{dt}-\frac{dU_0}{dt}\right)-\frac{d^2U_0}{dt^2} \tag{3-31}$$

Set

$$\left.\begin{aligned} A&=\left(\alpha+\frac{2}{\Delta t}\right)M+\left(\beta+\frac{\Delta t}{2}\right)K \\ b&=\frac{\Delta t}{2}(F_0+F_1)+\left(\alpha+\frac{2}{\Delta t}\right)MU_0+2M\frac{dU_0}{dt}+\left[\beta-\frac{\Delta t}{2}\right]KU_0 \end{aligned}\right\} \tag{3-32}$$

Then the equation can be rewritten as

$$AU_1=b \tag{3-33}$$

Solving, velocity vector U_1 at time step t_1 can obtained. Then, by substituting U_1 into equation (3-28), $\dot{U}_1$ can be obtained, and finally $\ddot{U}_1$ is obtained.

3.4 Finite element simulation of the X-post gyroscope

We have now derived all equations to simulate the behavior of the X-post gyroscope. For the purpose of our research, two different X-post gyroscopes are simulated. One is the perfect gyroscope (shown in Fig. 3.6); another one is an imperfect gyroscope (shown in Fig. 3.7).

For each case, the actuating voltage is $V=7\sin(\omega_2 t)$. The following six cases were simulated for each gyroscope:

(1) Temperature 0 ^0C + actuating voltage V
(2) Temperature 0 ^0C + Rotation (1rad/s) + actuating voltage V
(3) Temperature 0 ^0C + Rotation (100rad/s) + actuating voltage V
(4) Temperature 60 ^0C + actuating voltage V
(5) Temperature 60 ^0C + Rotation (1rad/s) + actuating voltage V
(6) Temperature 60 ^0C + Rotation (100rad/s) + actuating voltage V

The rotation vector is $\vec{\Omega}=\Omega_x\vec{i}+\Omega_y\vec{j}+\Omega_z\vec{k}=\vec{k}$. Its matrix forms are:

$$[\Omega]_1=\begin{bmatrix}0&-\Omega_z&\Omega_y\\ \Omega_z&0&-\Omega_x\\ -\Omega_y&\Omega_x&0\end{bmatrix}=\begin{bmatrix}0&1&0\\1&0&0\\0&0&0\end{bmatrix},[\Omega]_2=\begin{bmatrix}0&-\Omega_z&\Omega_y\\ \Omega_z&0&-\Omega_x\\ -\Omega_y&\Omega_x&0\end{bmatrix}=\begin{bmatrix}0&100&0\\100&0&0\\0&0&0\end{bmatrix} \tag{3-34}$$

3.4.1 Perfect X-post gyroscope

Fig. 3.6 shows the perfect X-post gyroscope. The actuating beam is parallel to the Y-axis and the sensing beam is in the X-axis direction. Pads 1, 2, 3 and 4 are deposited on the top surface, and pads 5, 6, 7 and 8 are deposited on the bottom surface. Pad 1 and pad 8 were used as actuator pads, and pads 3 and 6 were used as sensors.

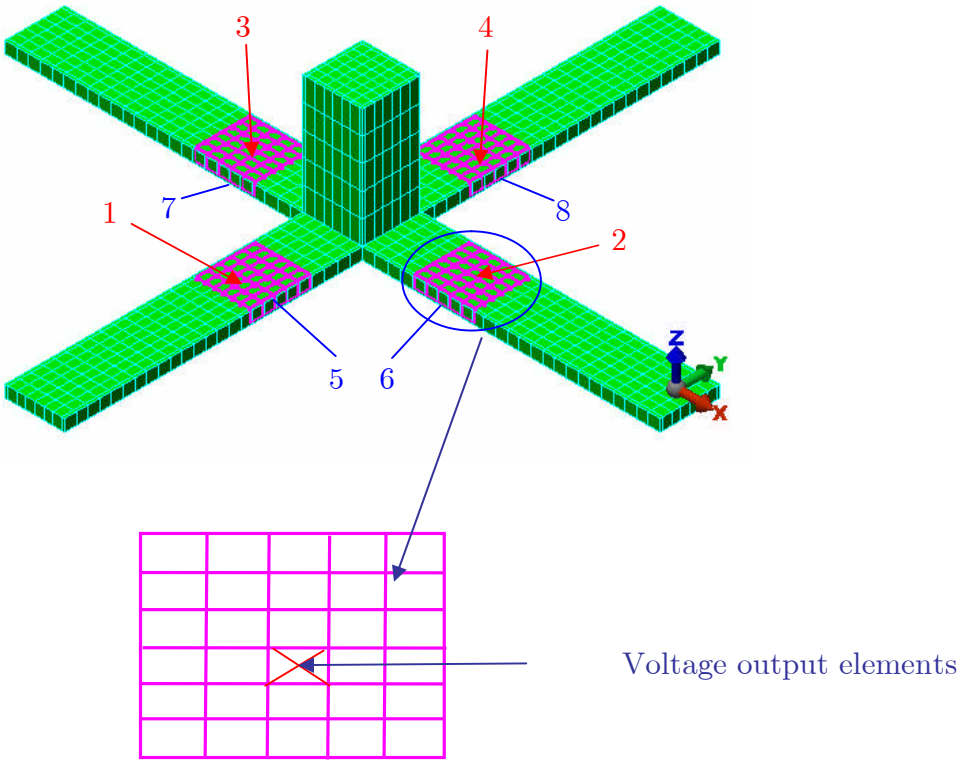

FIG. 3.6. Perfect X-post gyroscope.

3.4.1.1 Case 1 (Voltage).

Fig. 3.7 shows the voltage output at one element in pad 6. The maximum value is 2.9165e-3 mV, and the minimum is –2.9159e-3 mV. Fig. 3.8 shows the voltage output at one element in pad 3, the maximum value is 1.7249e-3 mV, and the minimum is –1.7253e-3 mV. Fig. 5.9 shows the voltage output at one element in pad 5. The maximum value is 1.4317 mV, and the minimum is –1.4316 mV. All output voltages in those calculated elements change from minimum value to maximum value with a sine-like curve.

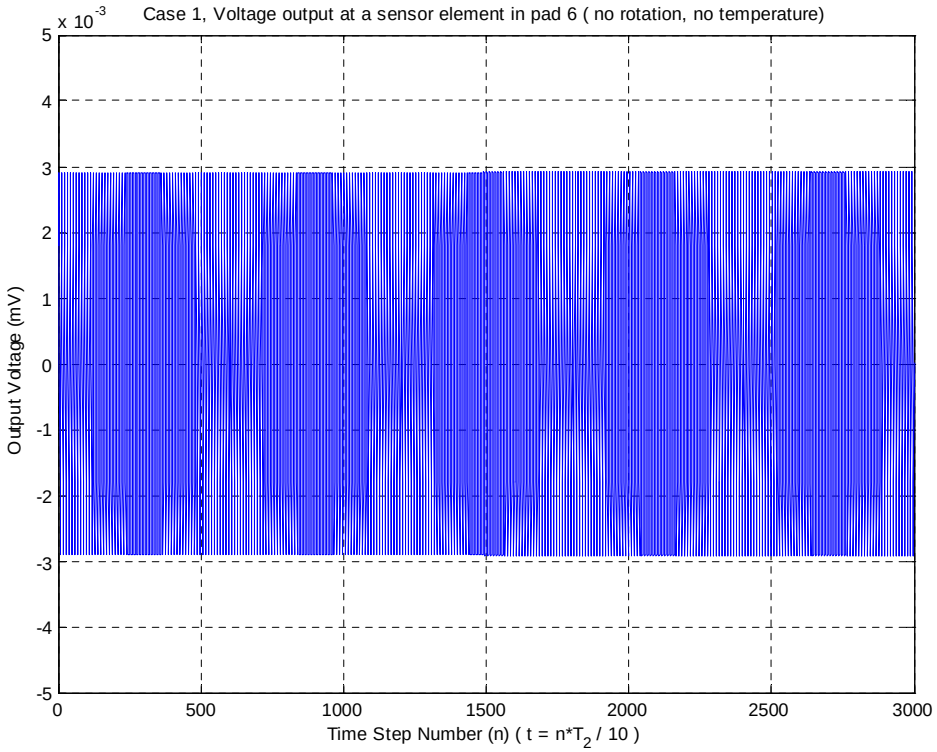

FIG. 3.7. Case 1, Voltage output at a sensor element in pad 6.

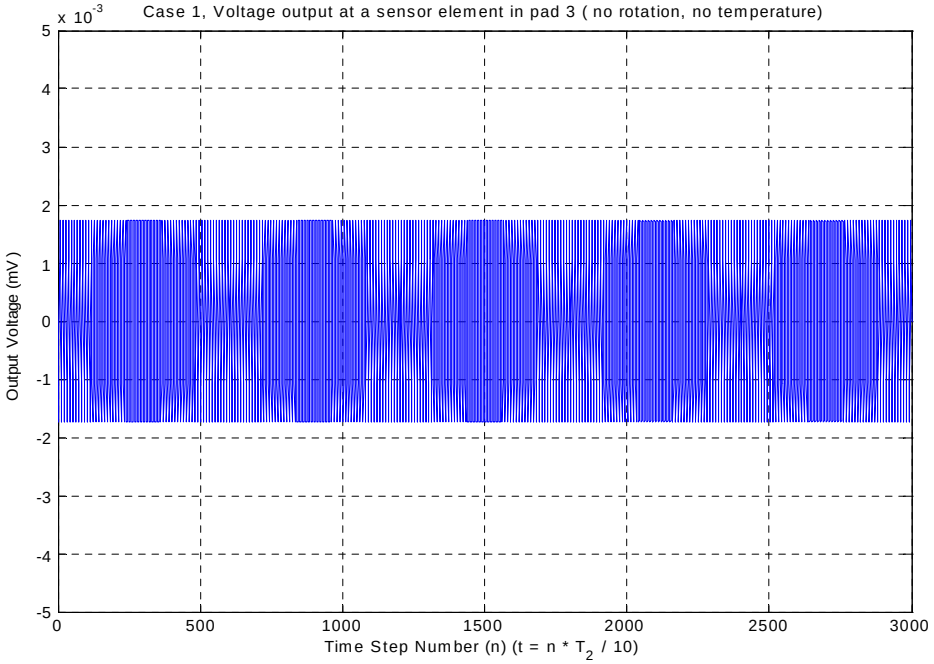

FIG. 3.8. Case 1, Voltage output at a sensor element in pad 3.

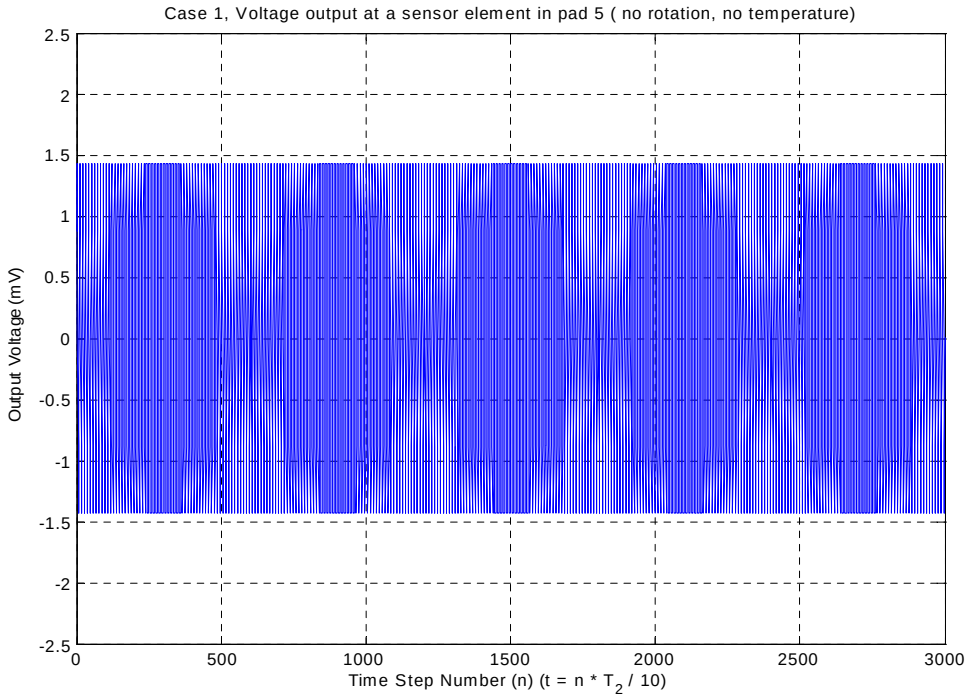

FIG. 3.9. Case 1, Voltage output at a sensor element in pad 5.

3.4.1.2 Case 2 (Voltage + Rotation(1rad/s))

Fig. 3.10 shows the voltage output at one element in pad 6 for case 2. The maximum value is 2.9236e-3 mV, and the minimum is –2.9256e-3 mV. Fig. 3.11 shows the voltage output at one element in pad 3. The maximum value is 1.7186e-3 mV, and the minimum is –1.7185e-3 mV. Fig. 3.12 shows the voltage output at one element in pad 5. The maximum value is 1.4313 mV, and the minimum is –1.4311 mV. Fig. 3.13 shows the Coriolis effect in pad 6 when the gyroscope rotates about the Z axis with the speed 1 rad/s. The maximum value is 1.151e-5 mV. Fig. 3.14 shows the Coriolis effect in pad 3 when the gyroscope rotates about the Z axis with the speed 1 rad/s. The maximum value is 1.304e-5 mV.

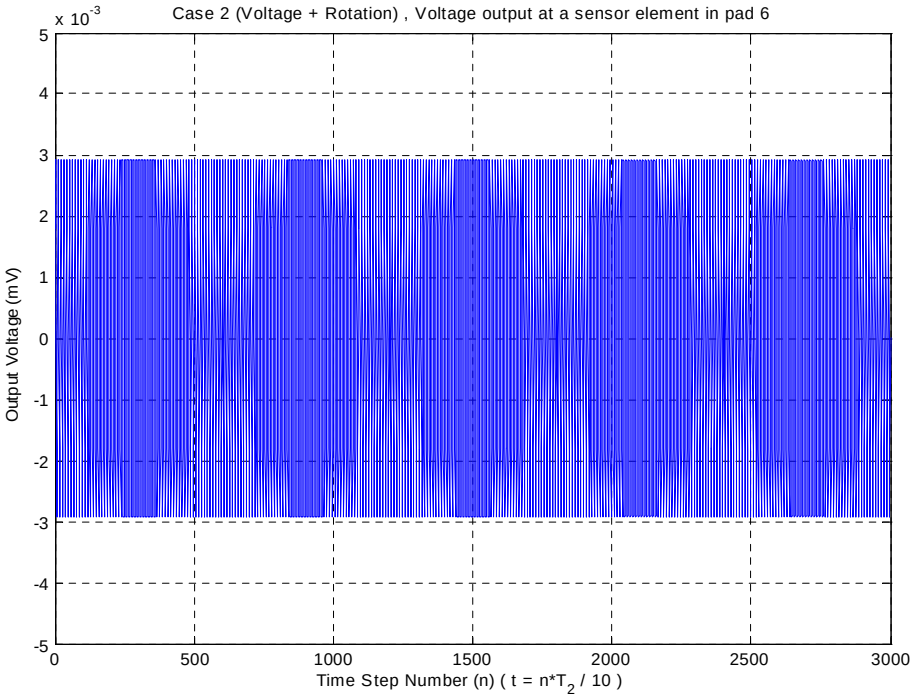

FIG. 3.10. Case 2, Voltage output at a sensor element in pad 6.

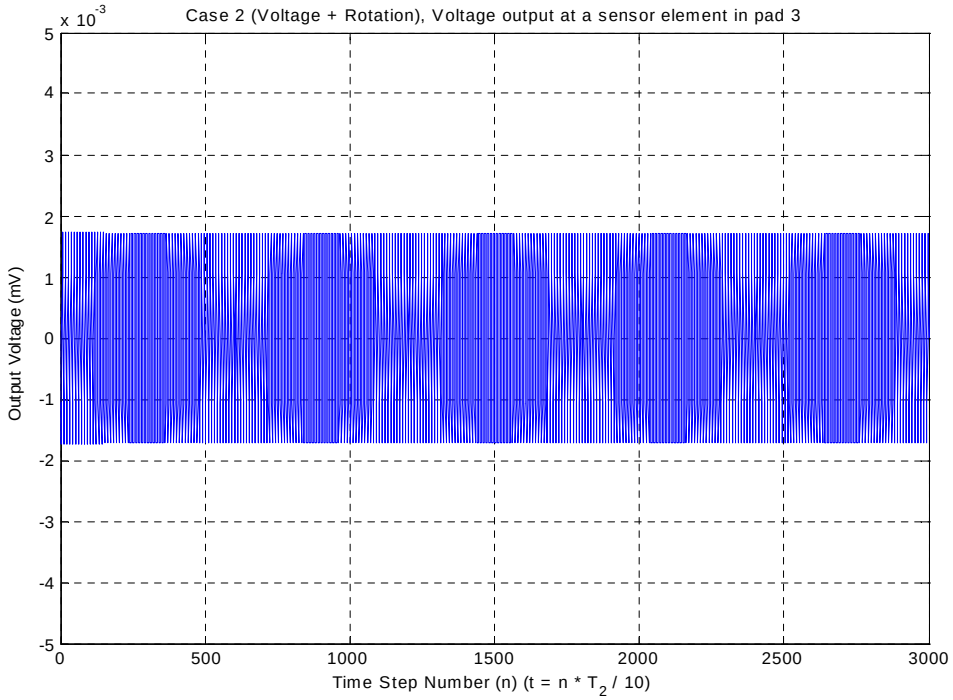

FIG. 3.11. Case 2, Voltage output at a sensor element in pad 3.

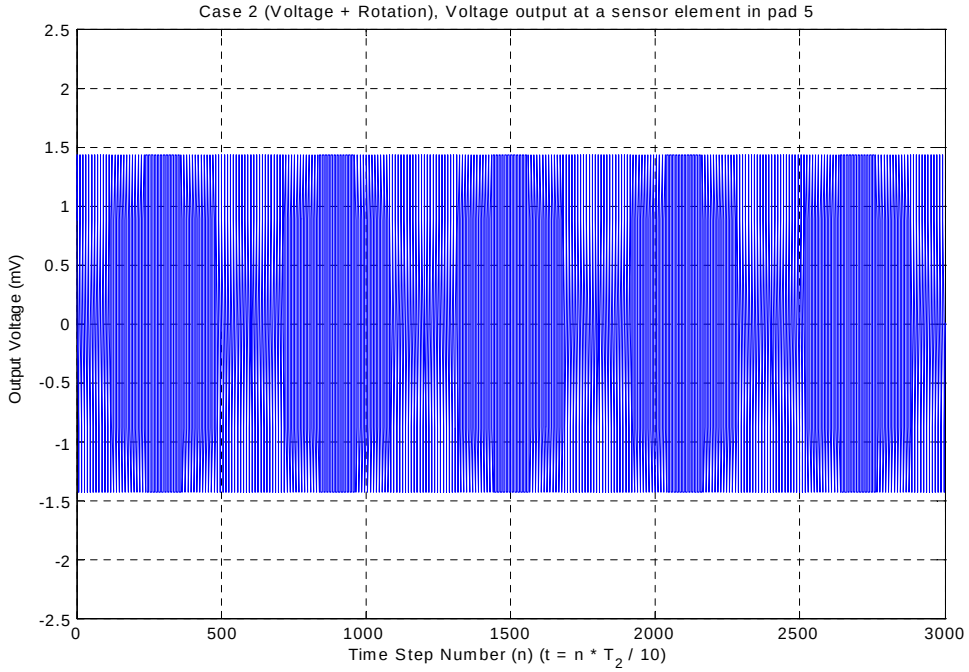

FIG. 3.12. Case 2, Voltage output at a sensor element in pad 5.

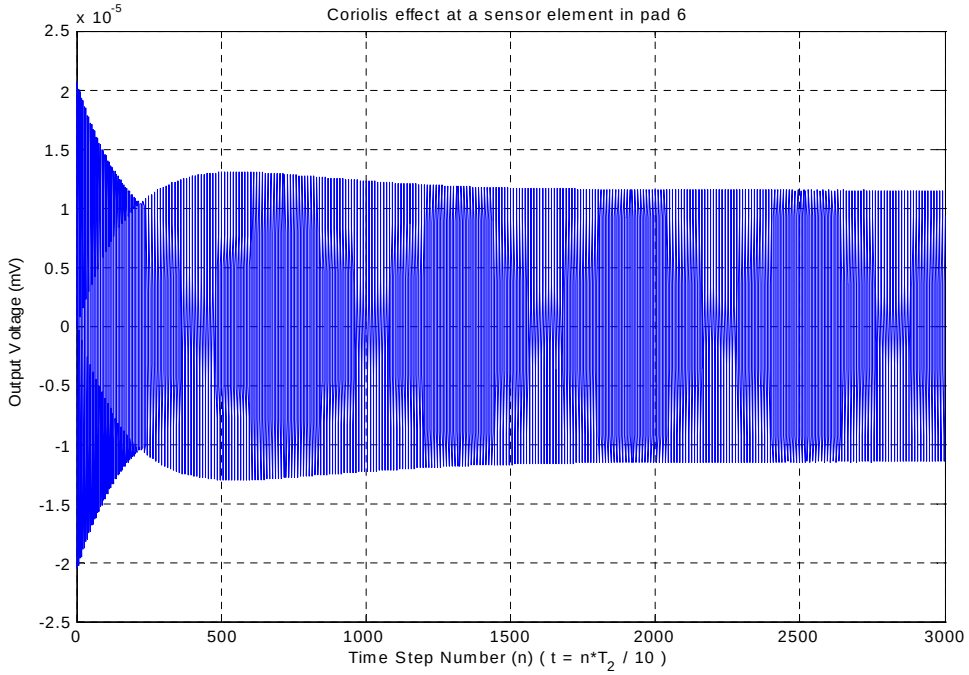

FIG. 3.13. Case 2, Coriolis effect at a sensor element in pad 6.

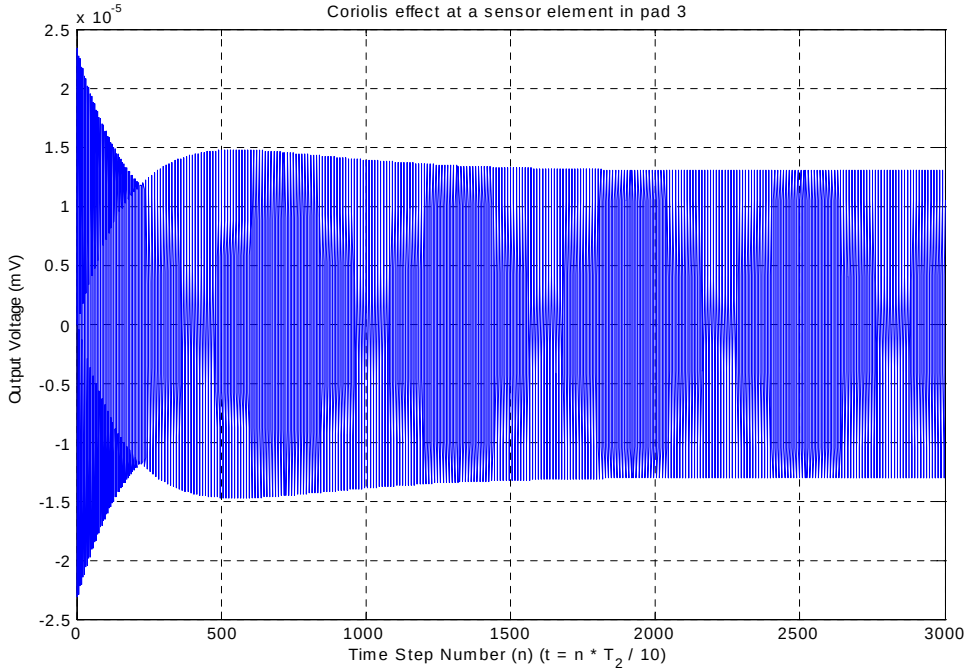

FIG. 3.14. Case 2, Coriolis effect at a sensor element in pad 3.

3.4.1.3 Case 3 (Voltage + Rotation(100rad/s))

Fig. 3.15 shows the voltage output at one element in pad 6 for case 3. The maximum value is 3.8451e-3 mV, and the minimum is –3.845e-3 mV. Fig. 3.16 shows the voltage output at one element in pad 3. The maximum value is 1.4678e-3 mV, and the minimum is –1.4657e-3 mV. Fig. 3.17 shows the Coriolis effect in pad 6 when the gyroscope rotates about the Z axis with the speed 100 rad/s. The maximum value is 1.431 mV. Fig. 3.18 shows the Coriolis effect in pad 3 when the gyroscope rotates about the Z axis with the speed 100 rad/s. The maximum value is 1.300e-3 mV.

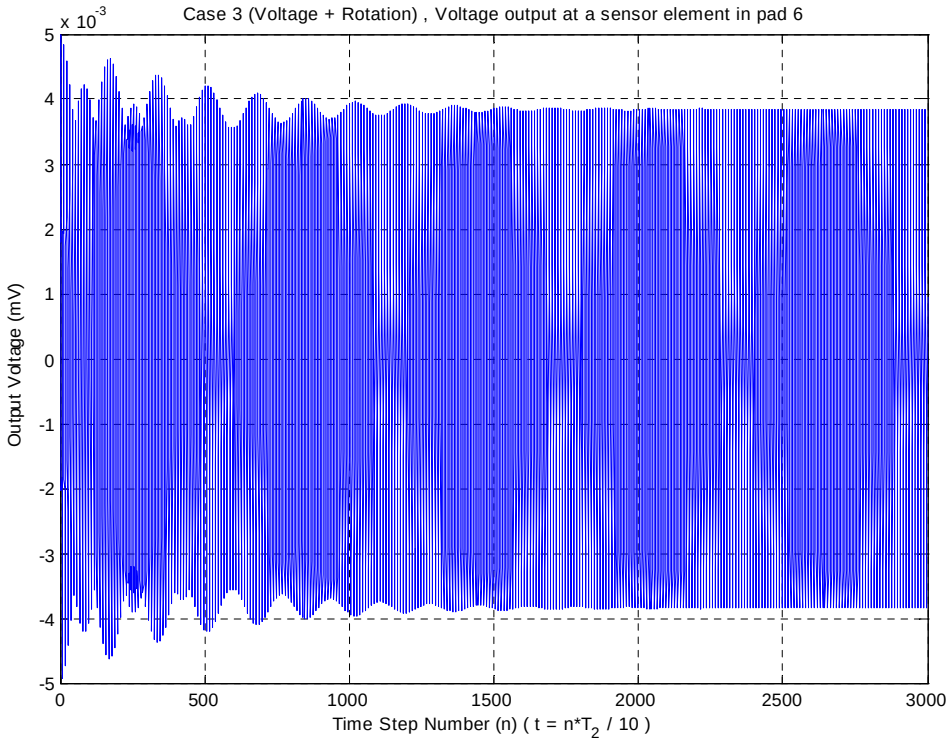

FIG. 3.15. Case 3, Voltage output at a sensor element in pad 6.

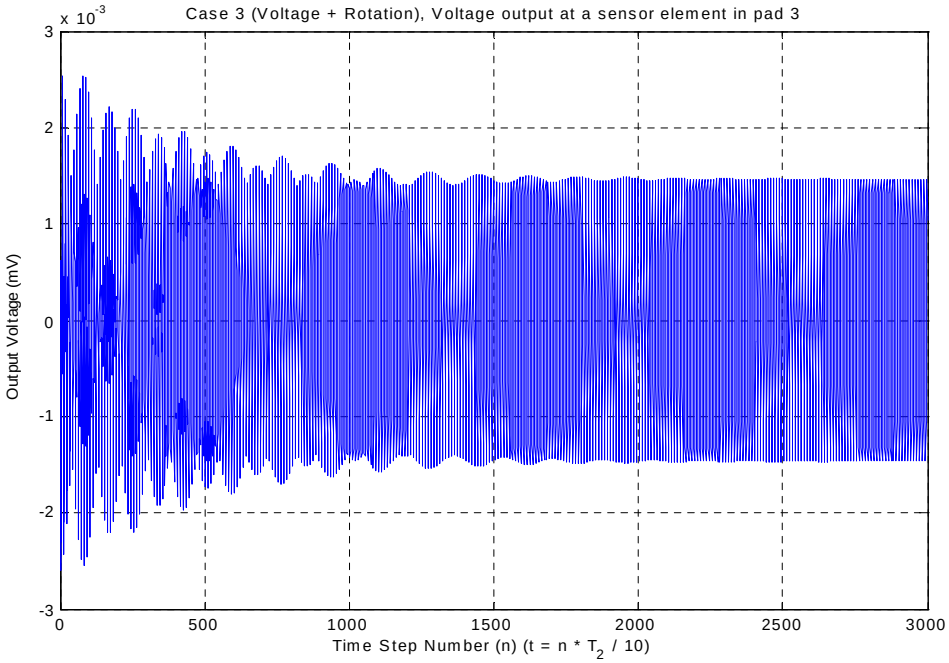

FIG. 3.16. Case 3, Voltage output at a sensor element in pad 3.

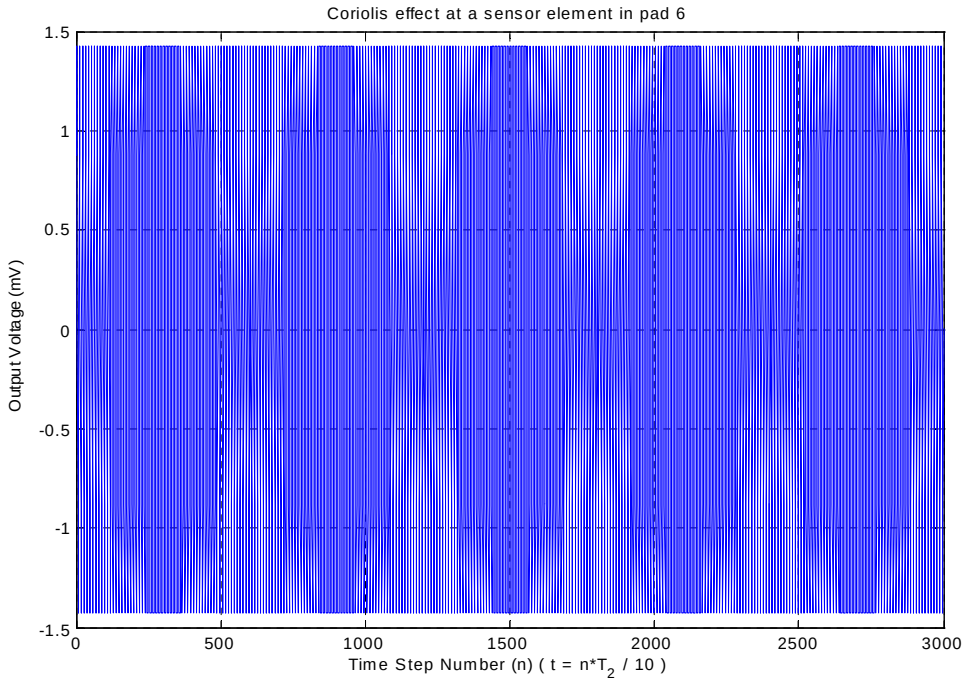

FIG. 3.17 Case 3, Coriolis effect at a sensor element in pad 6.

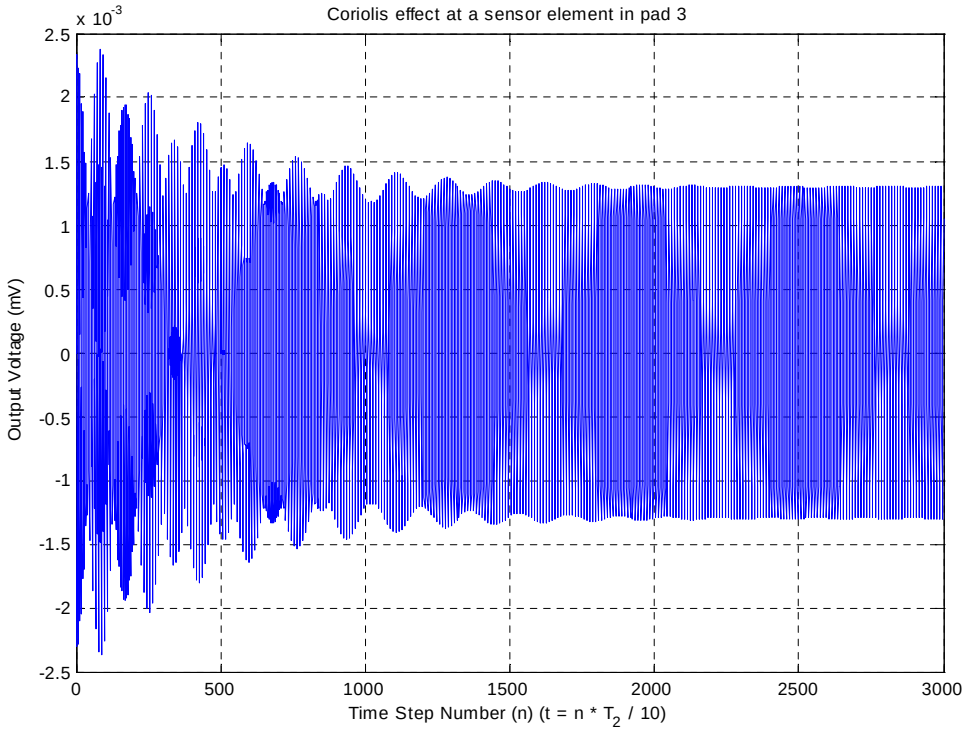

FIG. 3.18. Case 3, Coriolis effect at a sensor element in pad 3.

3.4.1.4 Case 4 (Voltage + T (60 °C))

Fig. 3.19 shows the voltage output at one element in pad 6. The maximum value is -4.3839 mV, and the minimum is –4.3898 mV. Fig. 3.20 shows the voltage output at one element in pad 3. The maximum value is 4.4916 mV, and the minimum is 4.4882 mV. Fig. 3.10 shows the voltage output at one element in pads 5. The maximum value is -2.9565 mV, and the minimum is –5.8174 mV. All output voltage in those calculated elements change from minimum value to maximum value with a sine-like curve.

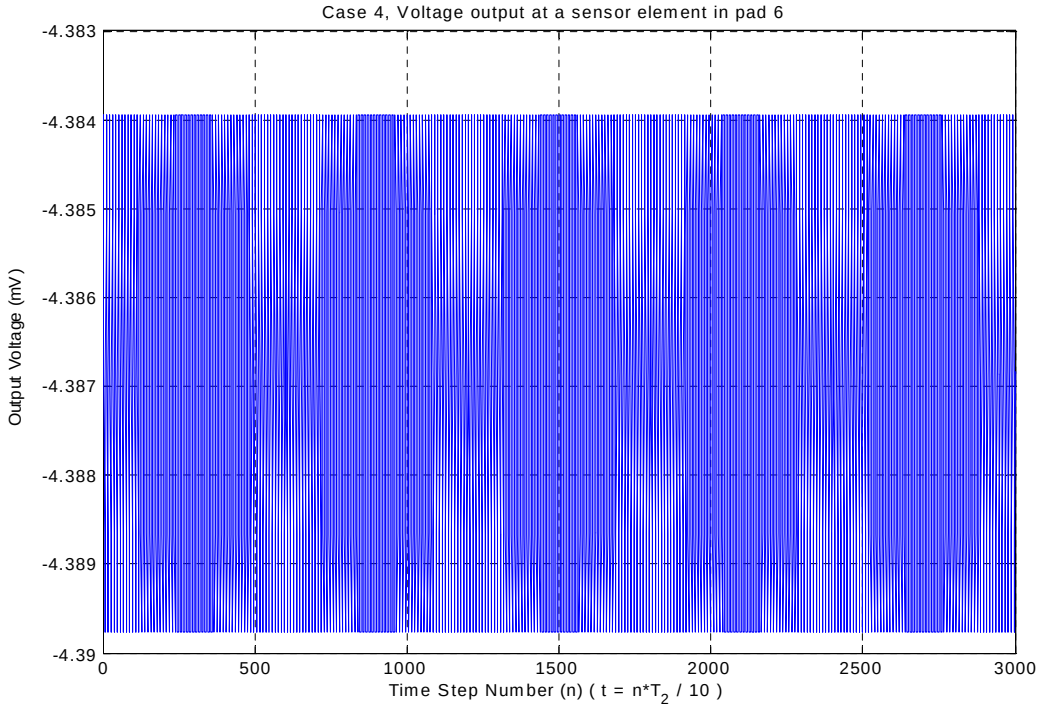

FIG. 3.19. Case 4, Voltage output at a sensor element in pad 6.

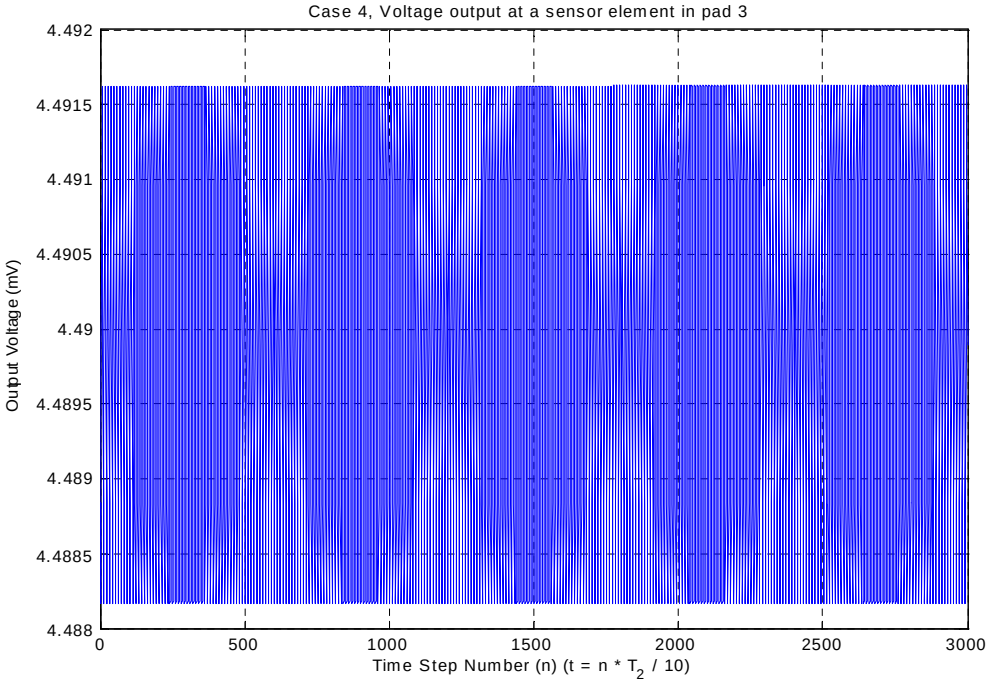

FIG. 3.20. Case 4, Voltage output at a sensor element in pad 3.

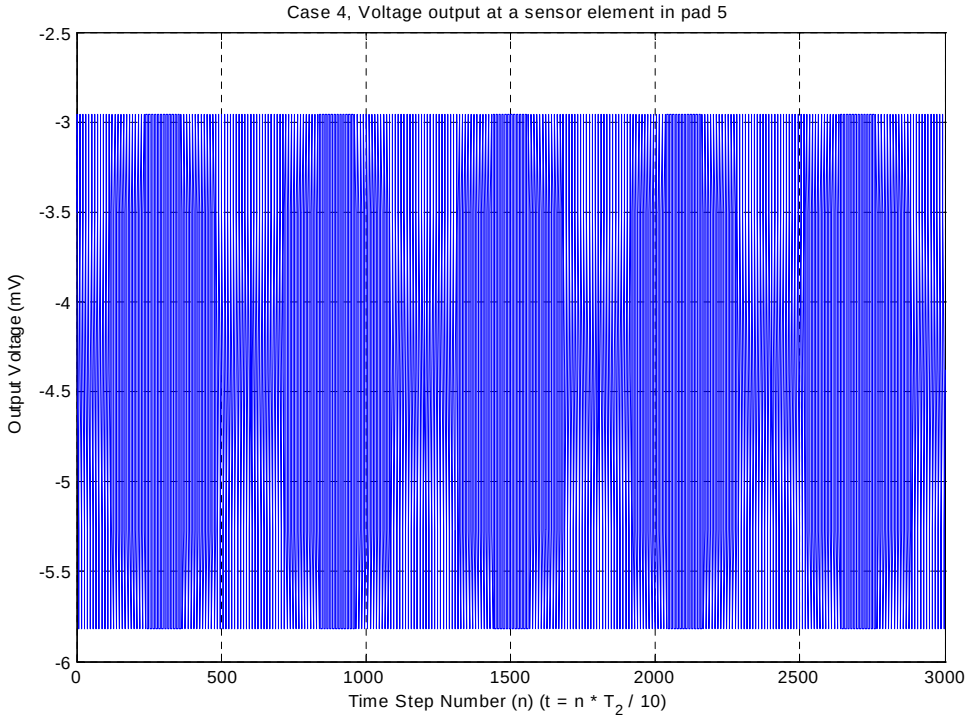

FIG. 3.21. Case 4, Voltage output at a sensor element in pad 5.

3.4.1.5 Case 5 (Voltage + T (60°C) + Rotation (1rad/s))

Fig. 3.22 shows the voltage output at one element in pad 6. The maximum value is -4.3839 mV, and the minimum is –4.3898 mV. Fig. 3.23 shows the voltage output at one element in pad 3. The maximum

value is 4.4916 mV, and the minimum is 4.4882 mV. Fig. 3.24 shows the voltage output at one element in pad 5. The maximum value is -2.9562 mV, and the minimum is -5.8178 mV. All output voltage in those calculated elements change from minimum value to maximum value with a sine-like curve.

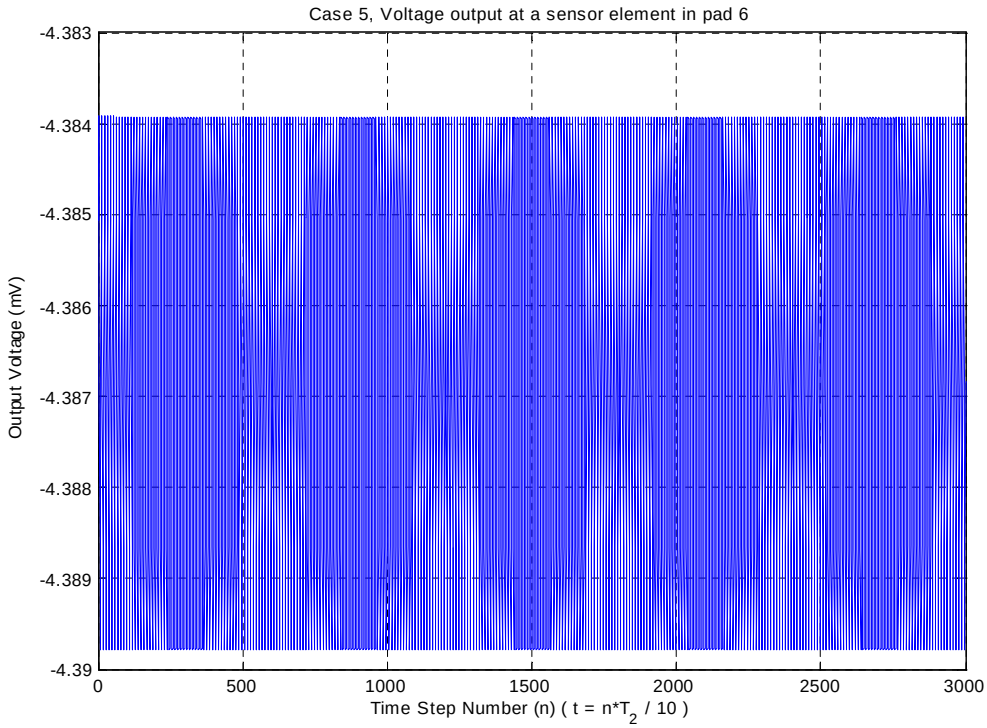

FIG. 3.22. Case 5, Voltage output at a sensor element in pad 6.

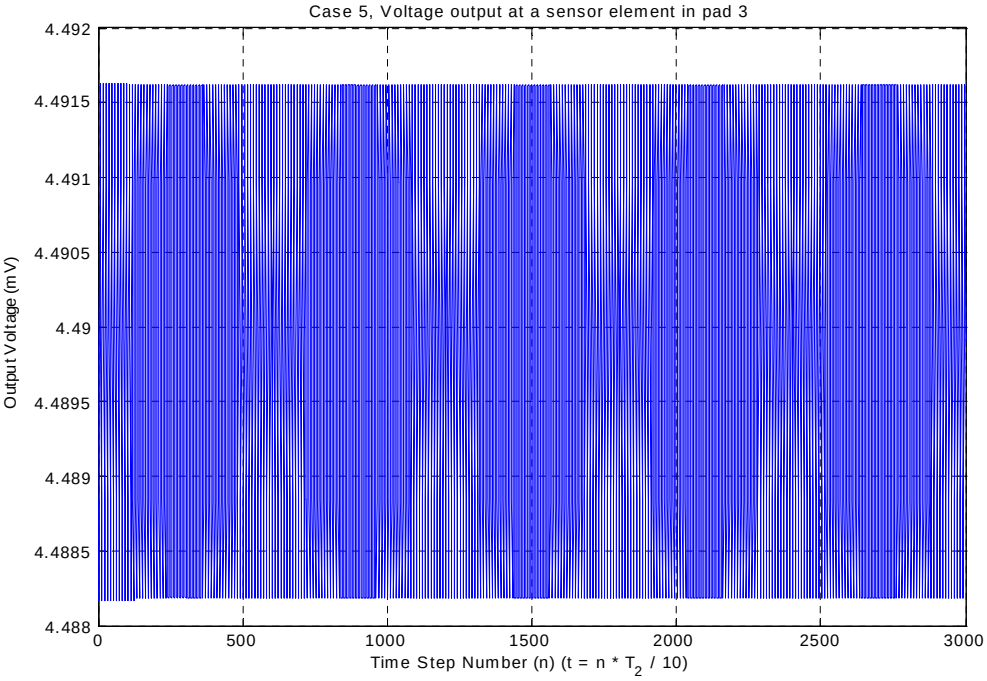

FIG. 3.23. Case 5, Voltage output at a sensor element in pad 3.

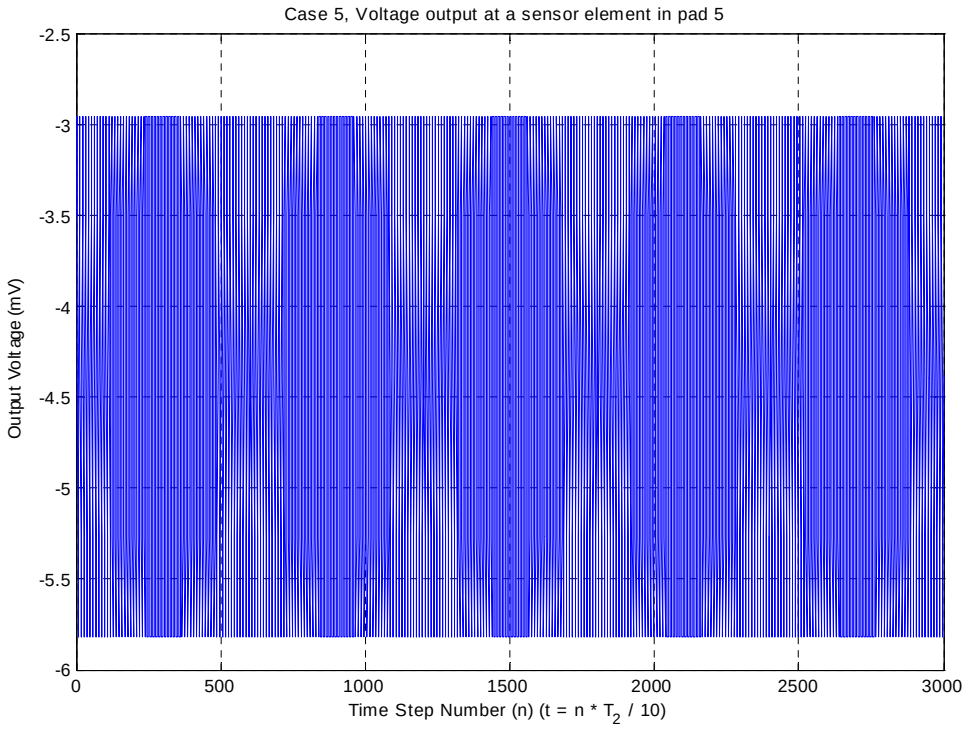

FIG. 3.24. Case 5, Voltage output at a sensor element in pad 5.

3.4.1.6 Case 6 (Voltage + T (60°C) + Rotation (100 rad/s))

Fig. 3.25 shows the voltage output at one element in pad 6. The maximum value is -4.383 mV, and the minimum is –4.3907 mV. Fig. 5.26 shows the voltage output at one element in pad 3. The maximum value is 4.4914 mV, and the minimum is 4.4884 mV. Fig. 3.27 shows the voltage output at one element in pad 5. The maximum value is -2.9554 mV, and the minimum is –5.8181mV. All output voltage in those calculated elements change from minimum value to maximum value with a sine-like curve.

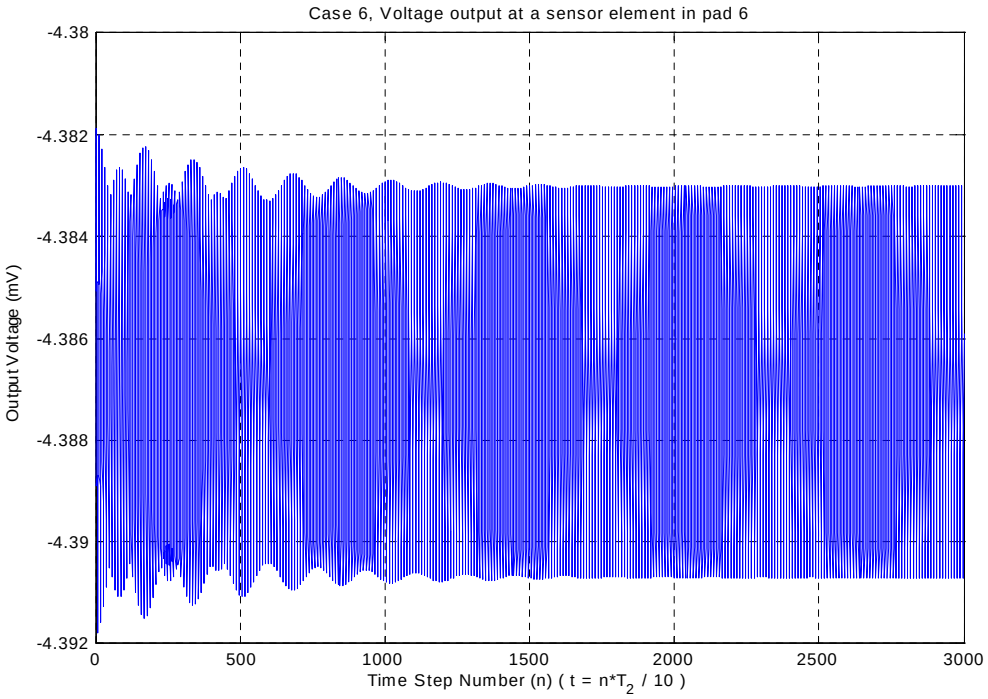

FIG. 3.25. Case 6, Voltage output at a sensor element in pad 6.

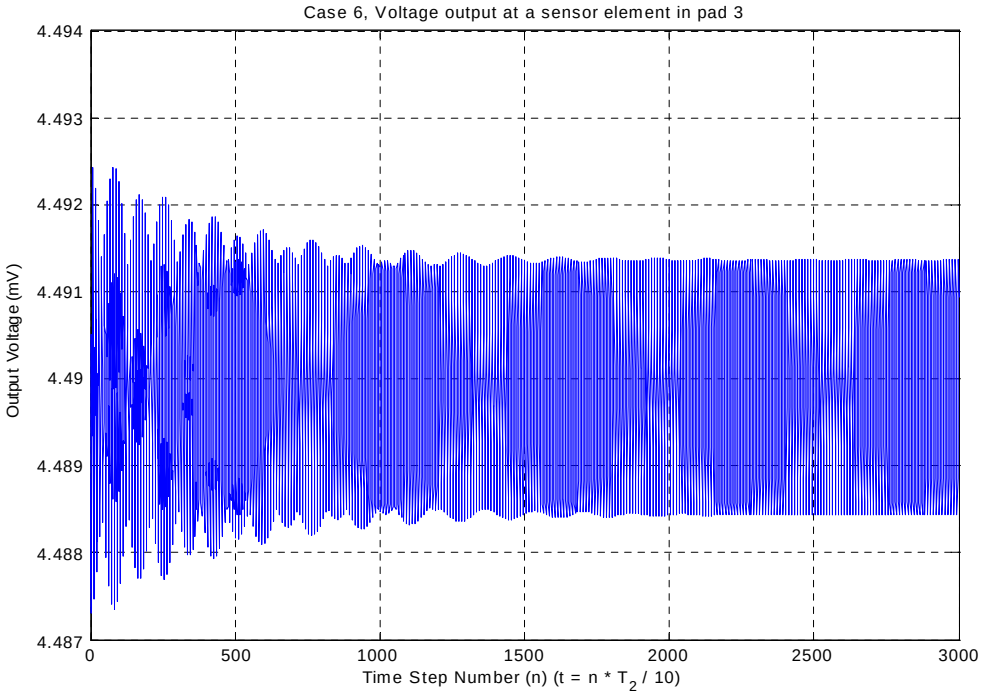

FIG. 3.26. Case 6, Voltage output at a sensor element in pad 3.

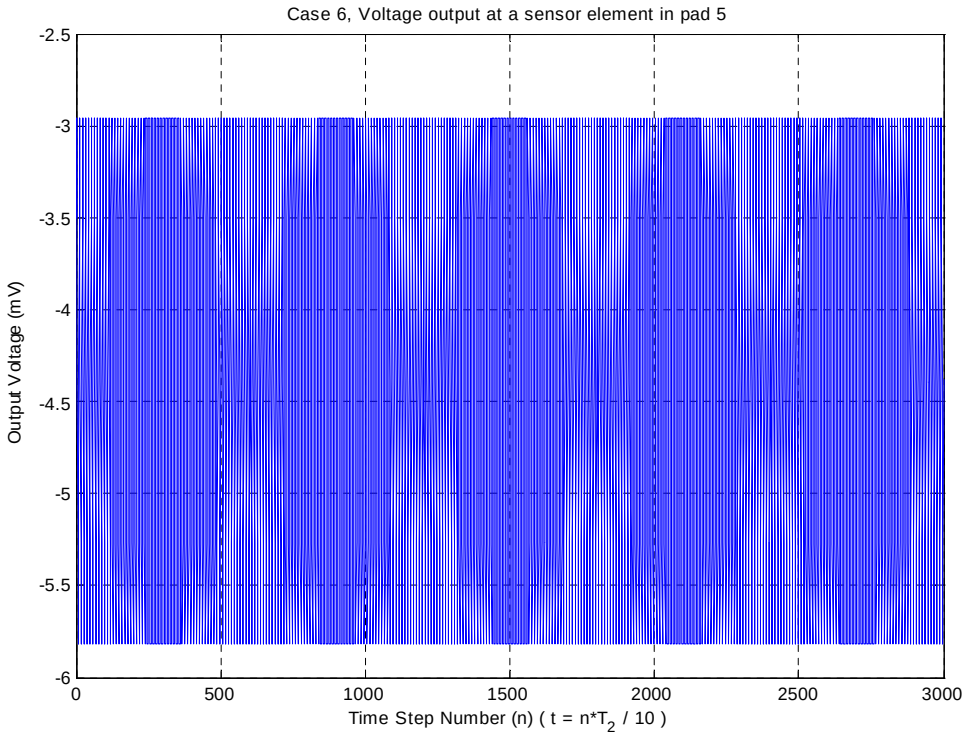

FIG. 3.27. Case 6, Voltage output at a sensor element in pad 5.

TABLE 3.1. Case comparison of output voltage in the perfect gyroscope.

Cases	Pad 6		Pad 3		Pad 5	
	Max(mV)	Min(mV)	Max(mV)	Min(mV)	Max(mV)	Min(mV)
Case 1	2.9165e-3	-2.9159e-3	1.7249e-3	-1.7253e-3	1.4317	-1.4316
Case 2	2.9236e-3	-2.9256e-3	1.7186e-3	-1.7185e-3	1.4313	-1.4311
Case 3	3.8451e-3	-3.845e-3	1.4678e-3	-1.4657e-3	1.431	-1.4314
Case 4	-4.3839	-4.3898	4.4916	4.4882	-2.9565	–5.8174
Case 5	-4.3839	-4.3898	4.4916	4.4882	-2.9562	-5.8178
Case 6	-4.383	–4.3907	4.4914	4.4884	-2.9554	–5.8181

3.4.2 Imperfect X-post gyroscope

Fig. 3.28 shows the imperfect X-post gyroscope. The actuating beam is parallel to the Y-axis, and the sensing beam is in the X-axis direction. Pads 1, 2, 3 and 4 are deposited on the top surface. Pads 5, 6, 7 and 8 are deposited on the bottom surface. Pad 1 and pad 8 were used as actuator pads. All other pads can be used as sensors.

For the imperfect gyroscope, the author simulated all 6 cases. For each case, the curve shape of output voltages at the sensor elements of different sensor pads looks like the corresponding curves for the perfect gyroscope pad. The author did not show all of the curves. The maximum values and minimum values for each case are in Table 3.2.

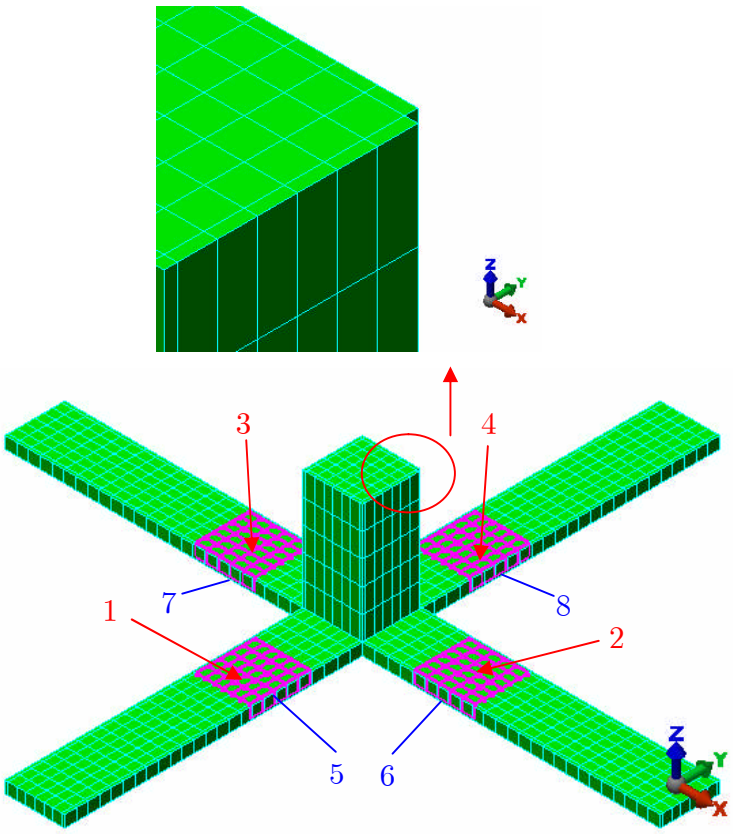

FIG. 3.28. Imperfect X-post gyroscope.

TABLE 3.2. Case comparison of output voltage in the imperfect gyroscope.

	Pad 6		Pad 3		Pad 5	
	Max(mV)	Min(mV)	Max(mV)	Min(mV)	Max(mV)	Min(mV)
Case 1	2.9302e-3	-2.9311e-3	1.7173e-3	-1.7178e-3	1.4311	-1.4311
Case 2	2.9397e-3	-2.9413e-3	1.7097e-3	-1.7097e-3	1.4318	-1.4317
Case 3	3.859e-3	-3.859e-3	1.461e-3	-1.4631e-3	1.4317	-1.4317
Case 4	-4.3824	-4.3882	4.4848	4.4813	-2.9535	–5.817
Case 5	-4.3823	-4.3882	4.4848	4.4813	-2.9535	-5.8171
Case 6	-4.3814	–4.3891	4.4845	4.4816	-2.9535	–5.8171

3.4.3 Comparison and conclusion

The maximum and minimum output voltage listed in Table 3.1 and Table 3.2 indicated clearly the difference in results between cases. From these differences, the following conclusions can be drawn:

1. The finite element code BAMAFEM can compute the results of the Coriolis effect. For a perfect gyroscope, when rotated at 1 rad/s, the Coriolis effect produced a voltage output 1.304e-5 mV. When the rotation speed was 100 rad/s, the value was 1.299e-3 mV.
2. The output voltages at the pad in the actuating beam are reasonable for all cases (millivolts). The output voltage in the sensing beam is much smaller (microvolts)
3. The effect of temperature environment on the performance is a dominant source of error in the simulated gyroscopes.
4. The imperfection of manufacture is also a source of error. For the first three cases, the effects of imperfection are larger than the Coriolis effect.

3.5 References

1. K. A. Chowdhury, Master thesis, The University of Alabama, 2002.
2. V. Z. Parton, B. A. Kudryavtsev, Electromagnetoelasticity Piezoelectrics and Electrically Conductive Solids, (Gordon and Breach, Amsterdam, the Netherlands, 1988).
3. A.P. Boresi, K. P. Chong, Elasticity in Engineering Mechanics. (Elsevier Science, New York).
4. Robert D. Cook, David S. Malkus, Michael E. Plesha. Concepts and Application of Finite Element Analysis, (John Wiley & Sons, New York, 1989)
5. D. T. Detwiler, M. H. Shen, V. B. Venkayya. “Finite element analysis of laminated structures containing distributed piezoelectric actuators and sensors,” Finite Elements in Analysis and Design, 20, 87-100 (1995)

6. H. S. Tzou and C. I. Tseng, "Distributed piezoelectric sensor/actuator design for dynamic measurement/control of distributed parameter systems: a pizeoelectric finite element approach," Journal of Sound and Vibration 138(1), 17-34 (1990).
7. S. K. Ha, C. Keilers, and F. K. Chang, "Finite element analysis of composite structures containing distributed piezoceramic sensors and actuators," AIAA Journal, 30 (3) (1992).
8. Corina Nistorica, Ph.D. Dissertation, The University of Alabama, 2003.
9. Guosheng Huang, Masters Thesis, The University of Alabama, 2002.
10. H. Han, X. Song, J. Zhong, S. Kotru, P. Padmini and R. K. Pandey, Applied Physics Letters, 85(22), 5310 (2004).
11. M.-A. Dubois and P. Muralt, Sensors and Actuators, 77, 106-112 (1999).
12. N. Ledermann, P. Muralt, J. Baborowski, S. Gentil, K. Mukati, M. Cantoni, A. Seifert and N. Setter, Sensors and Actuators, A105, 162-170 (2003)
13. X.-H. Du, J. Zheng, U. Belegundu and K. Uchino, Applied Physics Letters, 72 (19), 2421 (1998).
14. J. Ouyang, R. Ramesh and A. L. Roytburd, Applied Physics Letters, 86, 152901 (2005)
15. M. Kayton, W. R. Fried, Avionics Navigation Systems. 2nd ed. (John Wiley & Sons, Inc, 1996).
16. D. Guo, Z. Zheng, C. Zhao, F. Chu, "Vibration analysis of spinning cylindrical shells by finite element method", International Journal of Solids and Structures, 39 (3), 725-739 (2002).
17. I. M. Smith, D. V. Griffiths, Programming the Finite Element Method, Third Edition. (John Wiley & Sons, 1998).

4. LABORATORY DEVELOPMENT

4.1 Summary

About half of the FAA funding was spent on developing laboratory facilities to enable manufacture and testing of MEMS-technology gyroscopes. The clean room developed to do this is described below. It emphasizes bulk micromachining capabilities. The clean room also contains an unusual deep reactive ion etching machine that is capable of micromachining devices of materials other than silicon (in particular, quartz). The use of alternative materials is one idea that may help mitigate the severe effects on gyro performance due to temperature changes.

The clean room was completed only shortly before expiration of the FAA grant. Prior to its completion, development of the manufacturing processes for the proposed gyro was carried out at Redstone Arsenal in Huntsville, Alabama. We were only able to station one person at Redstone for extended time periods, a fact that substantially slowed progress in developing the gyroscope.

We also installed equipment to improve our ability to produce high-quality thin films, which are used for gyro actuators and sensors. We established a navigation laboratory containing a rate table, which was used to measure gyro performance. In addition we designed and constructed a laser trimming system to enable improving performance of individual gyros.

4.2. UA MEMS Fabrication Facility

Figure 4.1 Blue-M Oven

Figure 4.2 Second Blue-M Oven

Figure 4.3 Deep Reactive Ion Etcher (DRIE) Used for Bulk Micromachining

Figure 4.4 E-Beam Evaporator Used for Material Deposition

Figure 4.5 Profilometer Used for Dimensional Measurements

Figure 4.6 One of Three Fume Hoods- Used for Wet Etching and Other Purposes

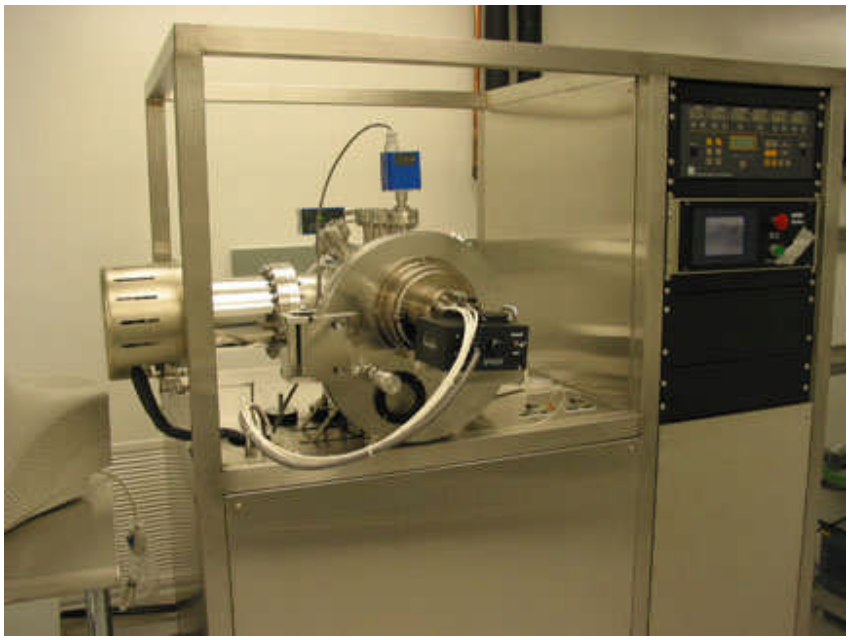

Figure 4.7 Ion Milling Unit Used for Material Removal

Figure 4.8 Microscope System

Figure 4.9 Plasma Asher Used for Photoresist Removal

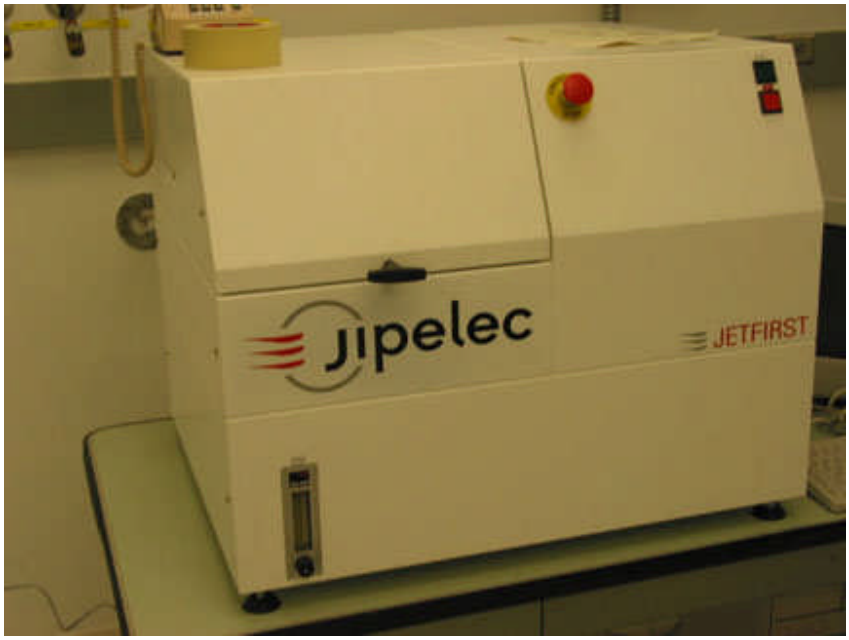

Figure 4.10 Rapid Thermal Annealing Unit- Used for Processing Thin Films

Figure 4.11 Photoresist Spinner

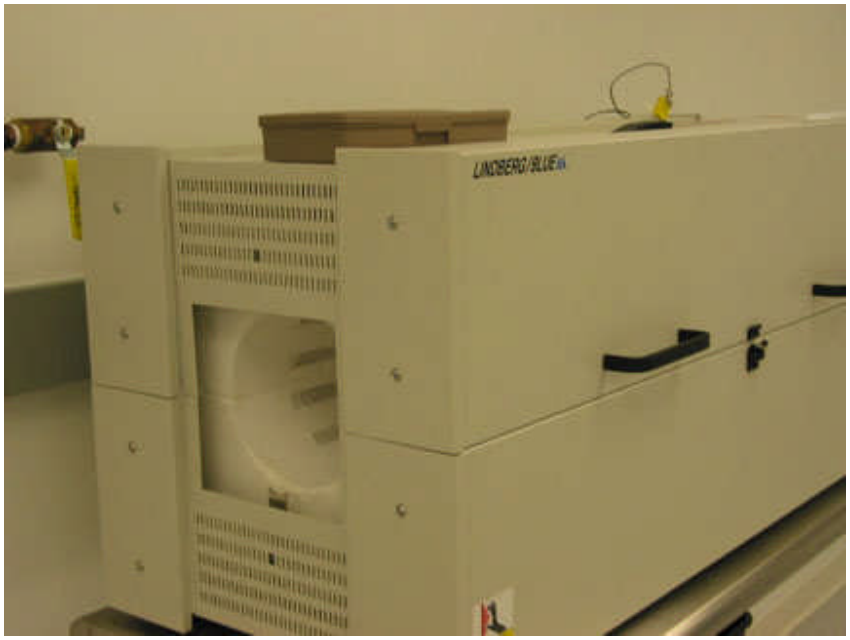

Figure 4.12 Tube Furnace

Figure 4.13 The Advanced Oxide Etch DRIE equipment

4.3 Navigation Laboratory

4.3.1 Laser Trimming System

The current method of optimizing gyroscope performance requires the removal of material to change the stiffness and mass distribution of the resonator. The objectives of this trimming operation are to bring the drive and sense frequencies closer together, and to bring the sense direction into close alignment with the sense direction. At present, this material removal is performed using a metal file. The laser trimming system will allow the systematic removal of much smaller amounts of material, enabling more precise trimming of the resonator, and thus improving the performance of the gyroscope. A software interface and control program for the laser system, shown in Fig. 4.14, below, has been implemented, allowing the power output of the laser to be controlled remotely, and providing a means to control burn duration. Fixtures for mounting the laser within a safety enclosure have been designed and constructed.

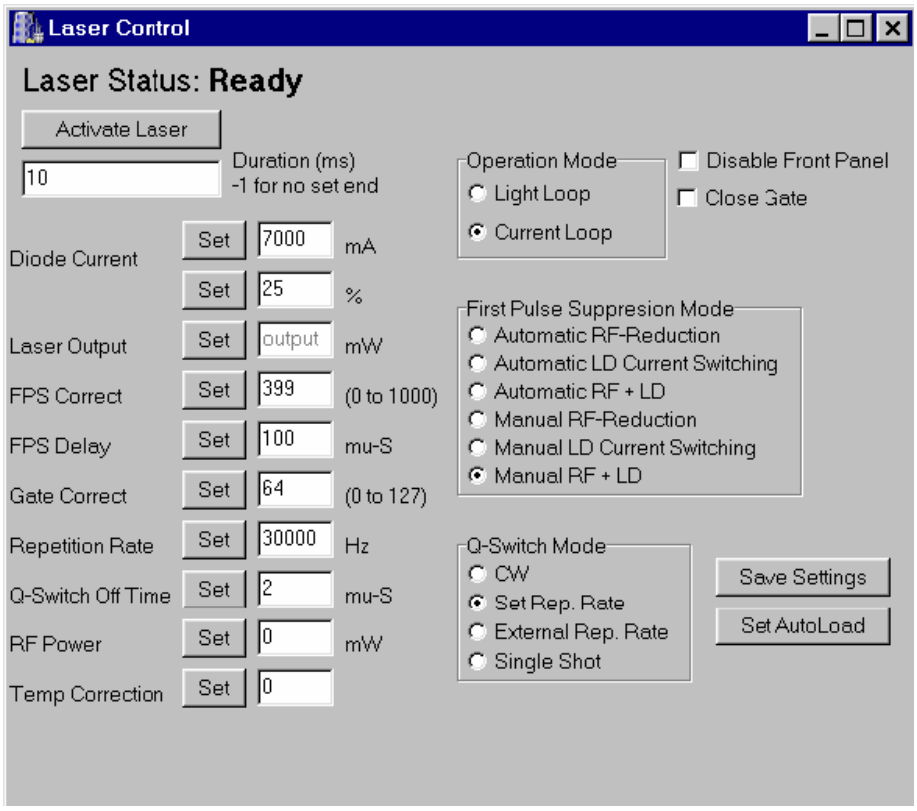

Figure 4.14 Laser Control Interface.

5. MATERIALS

5.1 Summary

In producing the gyro we decided to use PNZT thin film, a relatively new material, instead of the better understood PZT. This was done because we expected a larger output signal from PNZT, since its piezoelectric coefficient is higher than that of PZT. The choice of PNZT led to a research effort into optimizing the material deposition process for this material. This chapter reports the results of the successful process development. Use of the experimental apparatus designed and built to characterize the piezoelectric response of the film is described. We have optimized the sol-gel process for producing uniform PNZT films. The original gyro wafers undergoing processing used films produced by commercial vendors. The wafers we are now producing appear to have more uniformity and better properties. Our own wafers will be used for all devices manufactured after the first several we worked on prior to optimizing our processes. Also, as a possible option for the future, we briefly address the possibility of using sputtered RuO_x thin films.

5.2 Preparation of PNZT film on 4-inch diameter double sided wafers

Considerable amount of time was spent to scale up the growth of PNZT films from one inch square substrate to 4 inch diameter wafer. We were successful in depositing PNZT films by sol-gel on both sides of the 4 inch wafer with a good uniformity over 2 inch area. The film is about 650 nm thick and free of any cracks. Details about the film growth are described below.

Lead acetate trihydrate, zirconium acetate were dissolved in heated acetic acid, acetylacetone was then added to stabilize the solution. Titanium butoxide was added according to the atomic ratio of Zr/Ti = 20/80. The mixed solution was stirred for 30 minutes before 2 or 4 at.% niobium ethoxide was added. Finally, the solution was adjusted to 0.4 mol/L by adding 2-Methoxyethanol. An extra 20% of lead acetate trihydrate were added into the solution in order to compensate the loss of lead during heating process. The precursor solution was then spin-coated on both sides of $Pt/TiO_x/SiO_2/Si/SiO_2/TiO_x/Pt$ substrate at 3000 rpm for 30 seconds. Each layer was pyrolyzed at 400 ^oC for 5 minutes, and then annealed at 650 ^oC for 5 minutes in air by inserting the sample directly into the tube furnace. These steps were repeated to achieve the desired thickness. Figure 5.1 shows the picture of one sample.

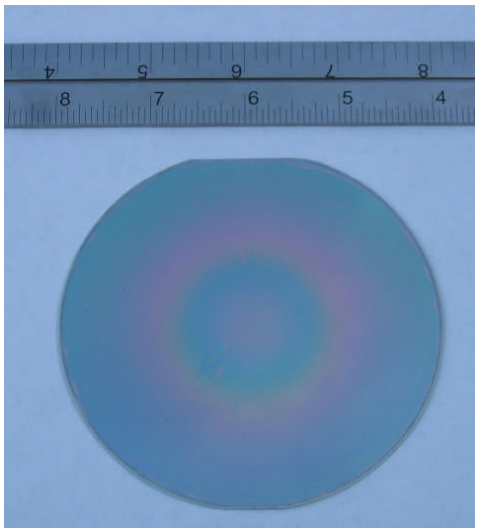

Fig. 5.1 PNZT film on a 4-inch diameter $Pt/TiO_x/SiO_2/Si$ wafer (film is on both sides of the wafer, only one side shown in picture)

5.3 Structural characterization of PNZT films

The nominal composition of the films is $Pb_{1.2}(Zr_{0.2}Ti_{0.8})O_3$ with 2% Nb which will be referred to as PNZT(2/20/80), and $Pb_{1.2}(Zr_{0.2}Ti_{0.8})O_3$ with 4% Nb referred to as PNZT(4/20/80). X-ray diffraction (XRD) result shows that PNZT(2/20/80) film has a random orientation with major (111), (110) and minor (100) peaks whereas PNZT(4/20/80) film has a texture of (100), as shown in Figs. 5.2 (a,b).

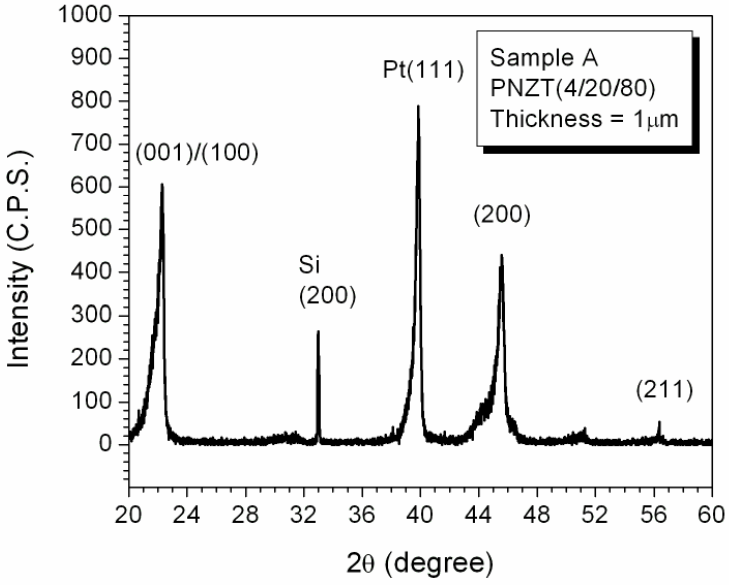

(a)

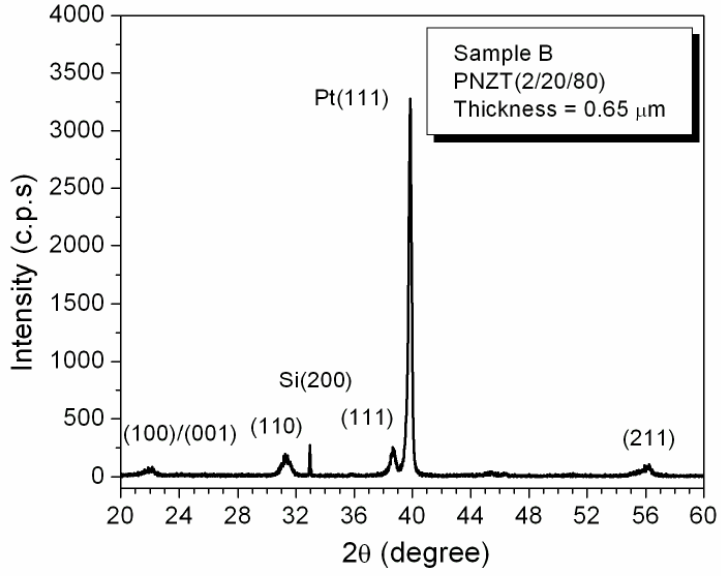

(b)

Fig. 5-2. XRD profiles of PNZT(4/20/80) and PNZT(2/20/80) films

5.4 Measurement set up for measuring piezoelectric properties

This section discusses the experimental apparatus to measure the response of PNZT films as a sensor and an actuator. These systems were shown in Chapter 2, Figures 2.4a,b,c and 2.5. To measure the PNZT film as a sensor we used the idea proposed by Dubois and Muralt[1]. In this set-up a bulk PZT actuator was used to drive the cantilever beam from the top at a certain frequency and a charge amplifier was used to collect the charge on the top electrode. Preamplifier and a lock-in amplifier were used to make sure that only the signal with the driving frequency was selected and measured. An optical sensor was used to measure the deflection at the driving point from the other side of the cantilever. An oscilloscope was used to monitor the signals. The piezoelectric coefficient $e_{31,f}$ was calculated by using the sensing mode[1].

For the actuator measurement (Fig. 2.4b), an AC voltage was used to drive the cantilever at a certain frequency from the top and bottom electrodes and the deflection of the free end of the cantilever was detected by an optic sensor. Figure 2.4c shows the geometric definition of the cantilever. For each cantilever there are two capacitors: one in the front side facing the optical sensor and another in the back side. Figure 2.5 is a photo of the set-up.

5.5 Preparation of cantilevers

The cantilevers were cut from the 4 inch PNZT wafers by using a wire saw with diamond-embedded steel wire. Wet etching was used to remove PNZT film to expose the bottom electrode. The top pt electrode was deposited by sputtering using a shadow mask. A fine silver wire was bonded to the bottom and top electrodes by silver epoxy. The PNZT films were poled under a field of 250 kV/cm by using 60,000 pulses with the duration of 0.01 ms. Dimensions of one of the cantilevers prepared from PNZT(2/20/80) are:

Length (L) = 34.3 mm
Width (b) =2.5 mm
Thickness (h) of Si substrate = 0.4 mm
Thickness of PNZT film = 650 nm.
Area of top electrode = 1 mm × 1 mm
Thickness of the top electrode = ~ 100 nm.
Distances x_1 from the electrode front edge to the base = 4.45 mm

5.6 Sensing mode measurement

For the sensor measurement, the distance L_d from the bulk PZT driving point to the base is 23.3 mm. The driving AC voltage of bulk PZT actuator is $5*\sin(2\pi ft)$ volt with a frequency f of 10 Hz. The deflection amplitude measured at the driving point is 369.3 nm. The charge amplitude measured from the front side capacitor is (0.70±0.01) pC. The capacitance of the electrode is 7.49 nF. So the voltage on the electrode due to the charge is about 0.09 mV. While for the back side capacitor the charge amplitude is (0.93±0.02) pC.

5.7 Actuating mode measurement

For the actuator measurement, the driving AC voltage on the back side capacitor is (2*sin(2πft)+2)volt with a frequency f of 10 Hz. The amplitude of deflection measured at the point of L = 29.3 mm is 20.6 nm.

5.8 Frequency dependence of the cantilever where one side is used a an actuator and another side as sensor

For this measurement another cantilever was prepared from the film PNZT(4/20/80). The dimensions of this cantilever are: length (*L)* = 43.85 mm, width (*b)* = 4.75 mm, thickness (*h*) of Si substrate = 0.4 mm, thickness of PNZT film = 1 micron, area of top electrode = 2 mm × 2 mm, thickness of the top electrode = ~ 100 nm. Since there is PNZT film on both sides of the wafer, we identify the two sides by naming these sides as "front side" and "back side". The electrode 1 extremity of both front side and back side is X_1=6.75 mm, X_2=8.75 mm. The driving point of bulk PZT on the cantilever is 38.80 mm and the deflection detect point is also at 38.80 mm. The driving source is 1.0*sin(2πft) volt with f = 10 Hz.

Figure 5.3 shows the piezoelectric coefficients $e_{31,f}$ measured on the front and back side of the PNZT film. The value of $e_{31,f}$ for back side PNZT film is 1.5 times higher than that of front side PNZT film. Figure 5.4 shows frequency dependence of the charge collected on the sensor side while the cantilever is driven on the actuator side. Here we first used front side of the film as an actuator and back side of the film as a sensor and then vise versa. In both cases the maximum signal is obtained at a frequency of 260 Hz (resonant frequency) whereas there is a 20 % difference in the value of charge obtained on the sensor side when we switch the actuating side and the sensing side. It should be noted here that the difference in the piezoelectric coefficients for the front side and back side of the film is about 50 %.

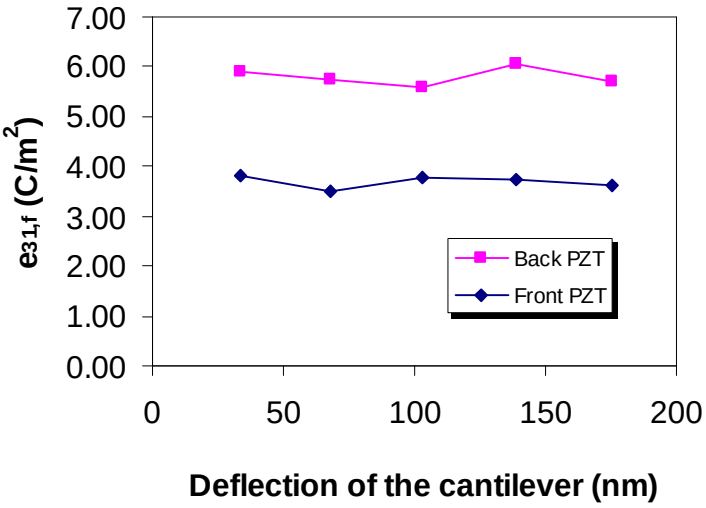

Fig.5.3. Piezoelectric coefficients $e_{31,f}$ of both sides PNZT films for PNZT(4/20/80)

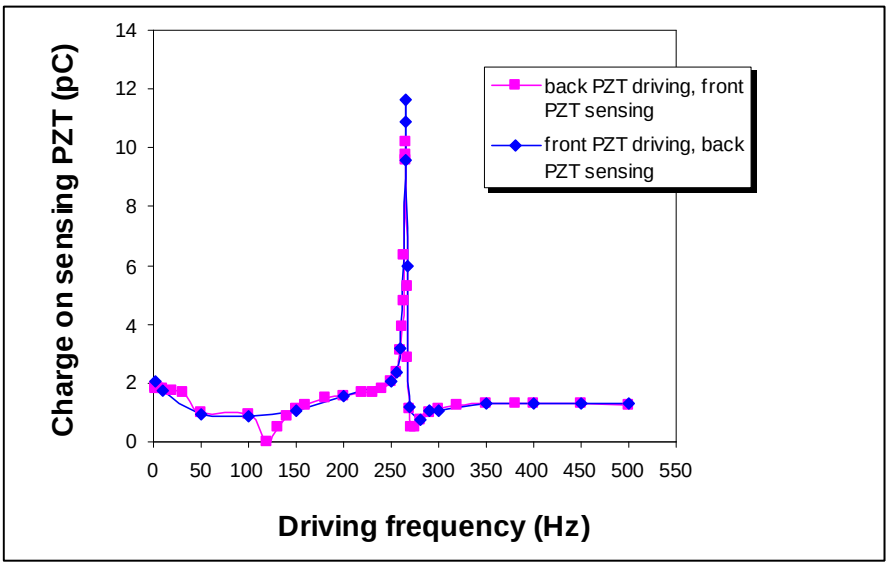

Fig. 5.4. Frequency dependence of actuating and sensing signal of a cantilever

5.9 Room temperature reactively sputtered RuOx thin films

As a possible option for the future, we addressed the possibility of using sputtered RuO_x thin films. RuO_x thin films were deposited at room temperature by reactive RF magnetron-sputtering using Ar/O2 discharges of varying O_2 ratio (f_{O2}) over the range 10% to 50% and were characterized using X-ray diffraction, X-ray reflectivity, X-ray photoelectron spectroscopy, resistivity and stress-temperature measurements. With the increase of f_{O2}, the film texture changed from (110) to (101). Films deposited with f_{O2}>25% were determined stoichiometric. The residual stresses in as-deposited films were all compressive and increased with addition of O_2, except for the film sputtered at f_{O2} =20% which was in biaxial tension. The film deposited at f_{O2} =30% had a low resistivity value of 68 µ.-cm and near zero stress (<50 MPa tensile) after a thermal cycle in air up to 500 ºC which is promising for use in micro-devices. More details details of this work may be found in reference 2.

5.10 References

1. M.-A. Dubois and P. Muralt, *Sensors and Actuators* **77**, 106 (1999)
2. J. Shi, F. Huang, M.L. Weaver, and T.M. Klein, "Effect of O_2 Flow Ratio on the Microstructure and Stress of Room Temperature Reactively Sputtered RuO_x Thin Films," J. Vac. Sci. Technol. A., Vol. 23, No. 3, May/Jun 2005. pp. 452-459.

6. ELECTRONICS

6.1 Summary

Gyro signal processing may be achieved by either analog signal processing or digital signal processing. As an effort to mitigate risk, we pursued parallel development of the two options. The analog signal processing system was completed and has been used in the navigation lab to test the X-post gyro. The circuit board for the digital processing system was designed, manufactured, and populated. Signal processing software was developed for it. The digital processing system awaits implementation in future work

6.2 Analog vs Digital Signal Processing

The gyro control system must:

- Induce a drive axis vibration at resonance (phase locked loop or adaptive mode tuning).
- Maintain a desired amplitude for the drive axis vibration (automatic gain control).
- Decouple drive and sense axes (quadrature control).
- Drive the sense axis vibration to zero (force-to-rebalance). The control signal becomes the rotation rate measurement.

The advantages of digital signal processing over analog signal processing are:

- Tighter control of accuracy/quality (No drift with temperature changes or aging or component manufacturing tolerances)
- No additional noise is introduced after A/D conversion
- More powerful processing techniques can be implemented, such as
  - Correlation filtering with tight synchronization
  - Thermal drift compensation
  - Electronic trimming
  - Adaptive processing
- Generate cleaner and more precise sinusoidal signals for gyro inputs and processing
- More flexibility
- Incorporation of multiple functions within a single Digital Signal Processor

The disadvantages of digital signal processing are:

- Restricted sampling speed – impacts response time, filtering, and noise reduction capabilities
- Restricted quantization accuracy – adds quantization noise
- Large learning curve for software development

6.3 Analog signal processing system

The system shown below in Figures 6.1 through 6.6 was designed, constructed, and used in the navigation laboratory to test the X-post gyroscope.

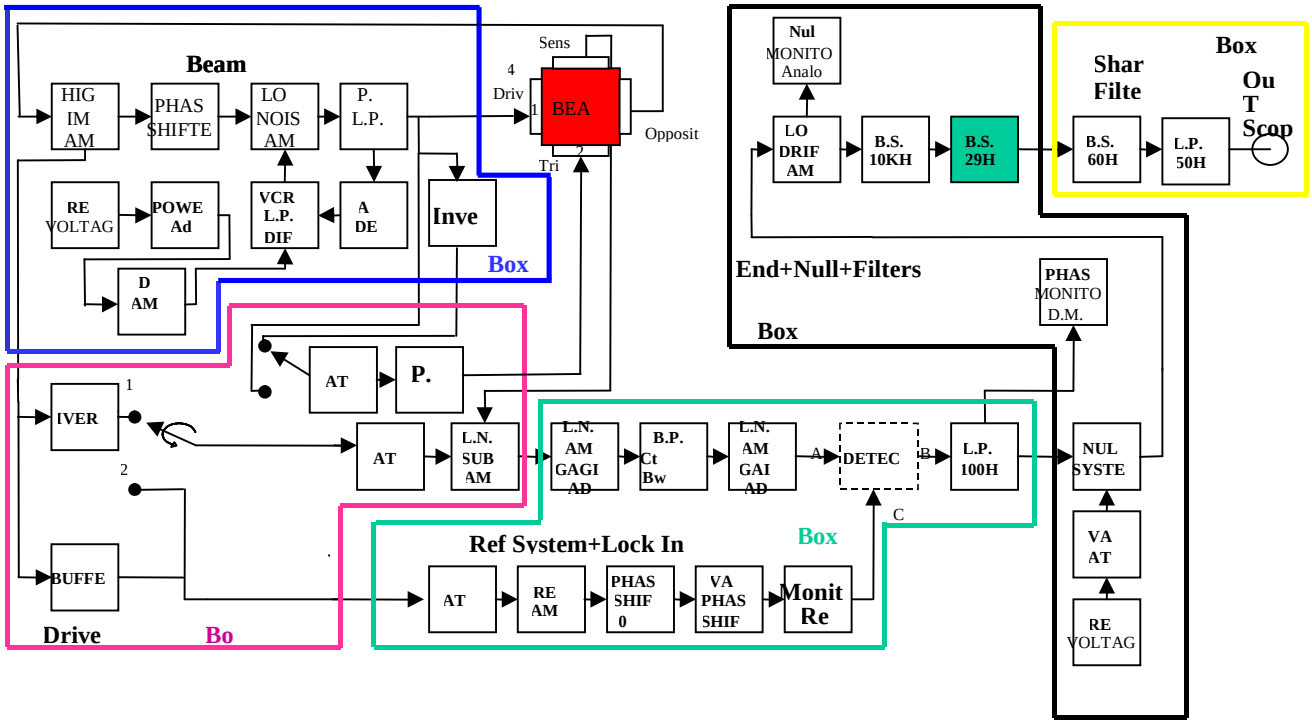

Figure 6.1 Design of open-loop analog electronics system

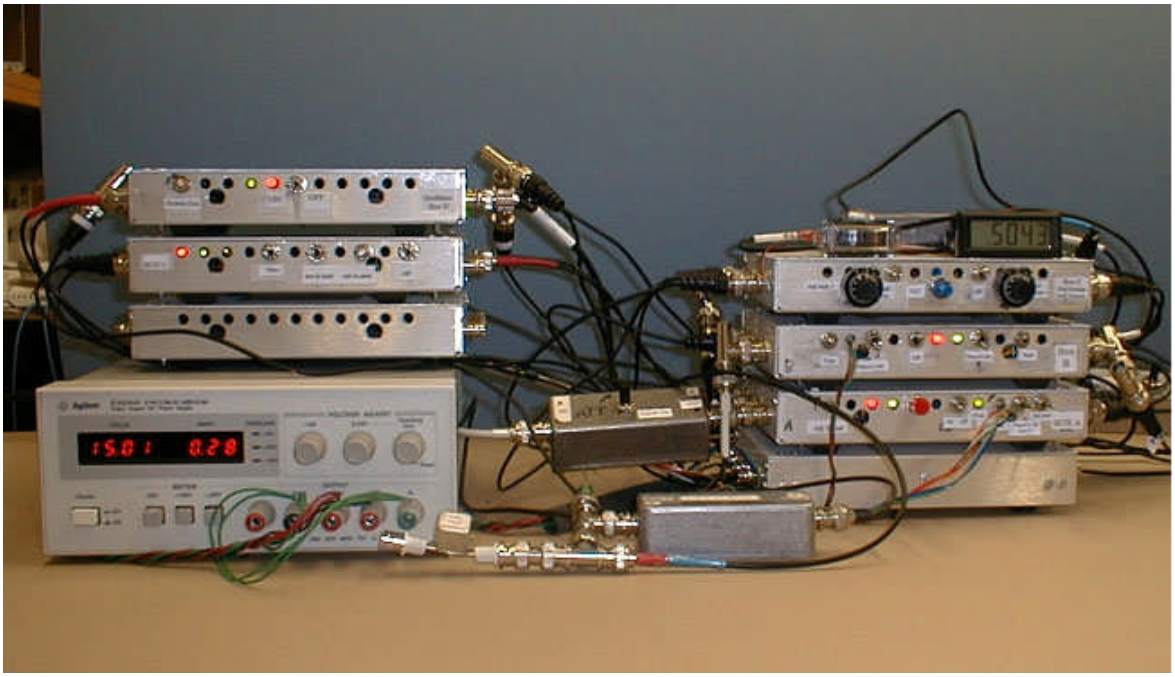

Figure 6.2 Photo of open-loop analog electronics system

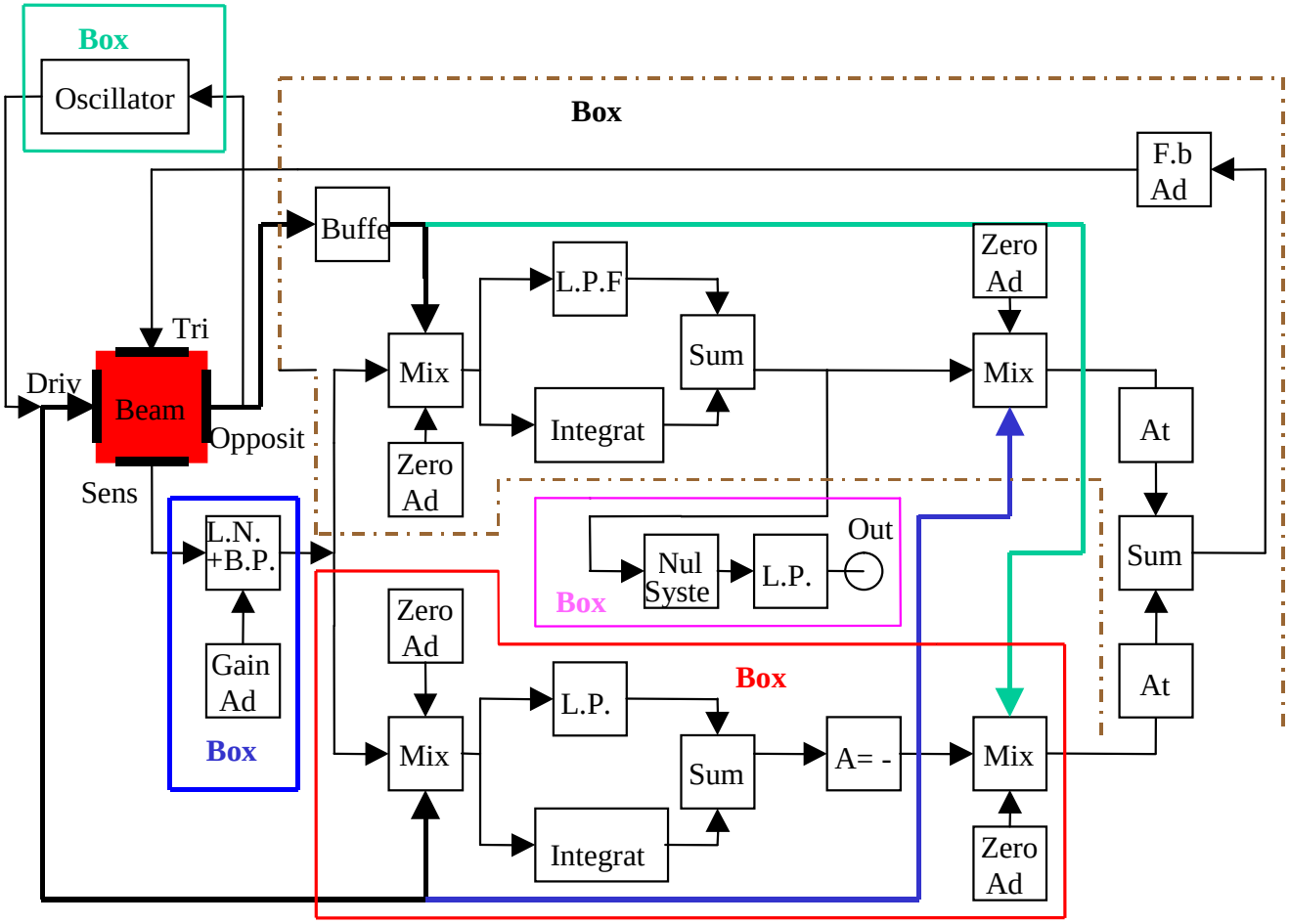

Figure 6.3 Design of closed-loop analog electronics system

Figure 6.4 Photo of closed-loop analog electronics system for gyro

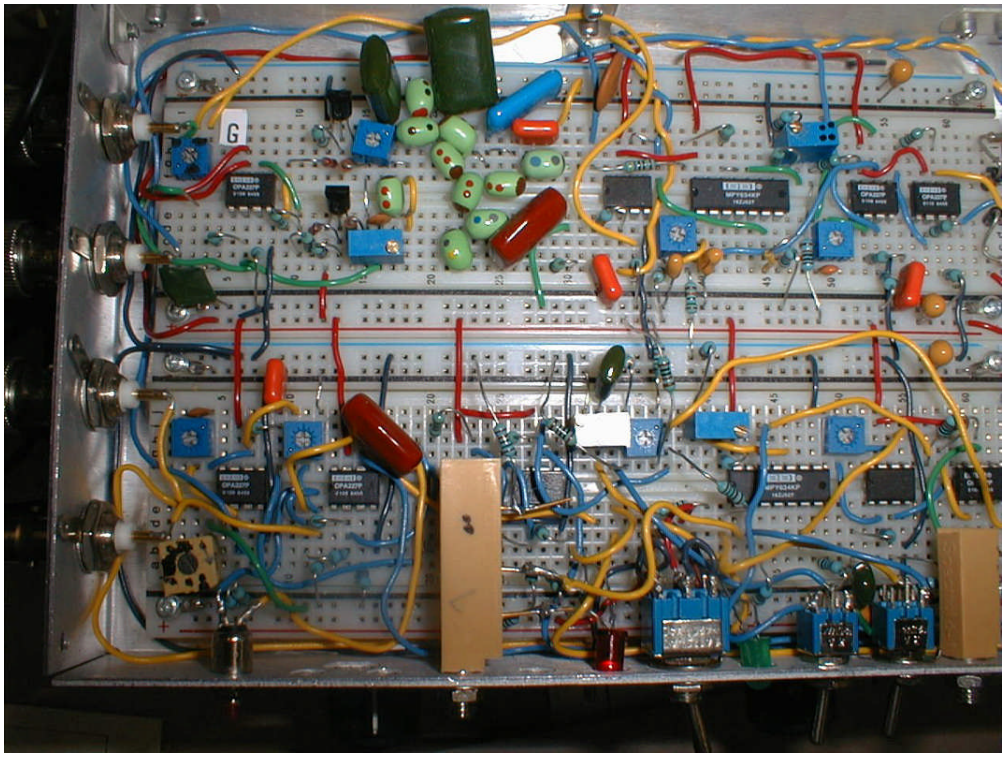

Figure 6.5 Circuit of closed-loop analog electronics system for gyro- box 1

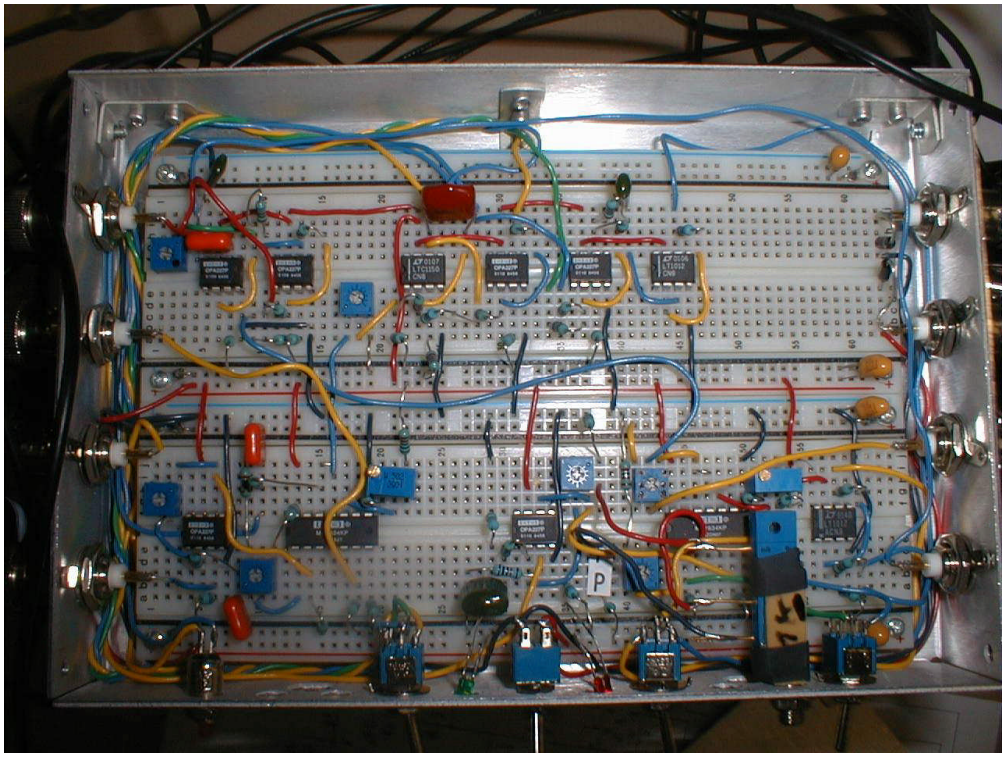

Figure 6.6 Circuit of closed loop analog electronics system for gyro- box 2

6.4 Digital Control System

We have created a general development platform using inexpensive off-the-shelf equipment (with existing software development tools and existing software libraries) as much as possible.
We have developed and added custom electronics where necessary. The digital control system begins with a TI TMS320C6711 DSK motherboard. For use with the gyro we designed and built a custom daughterboard to mate with the motherboard. The system is illustrated in Figures 6.7 and 6.8.

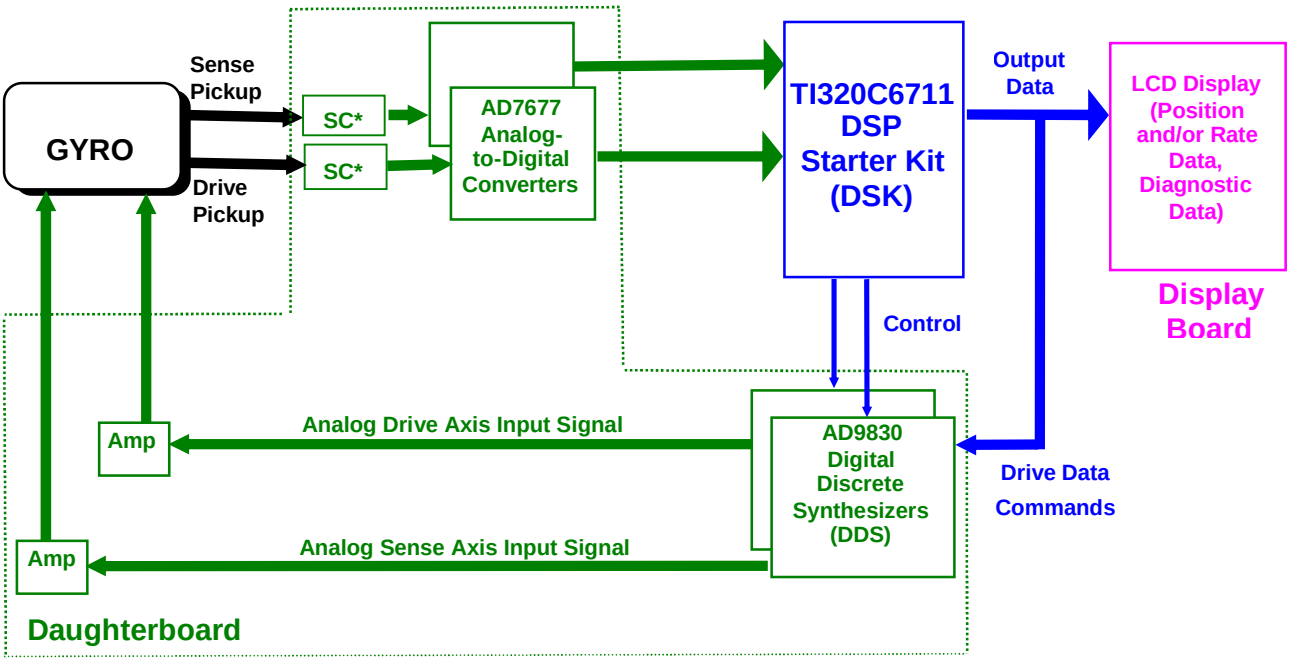

Figure 6.7 Design of the daughterboard for gyro digital signal processing

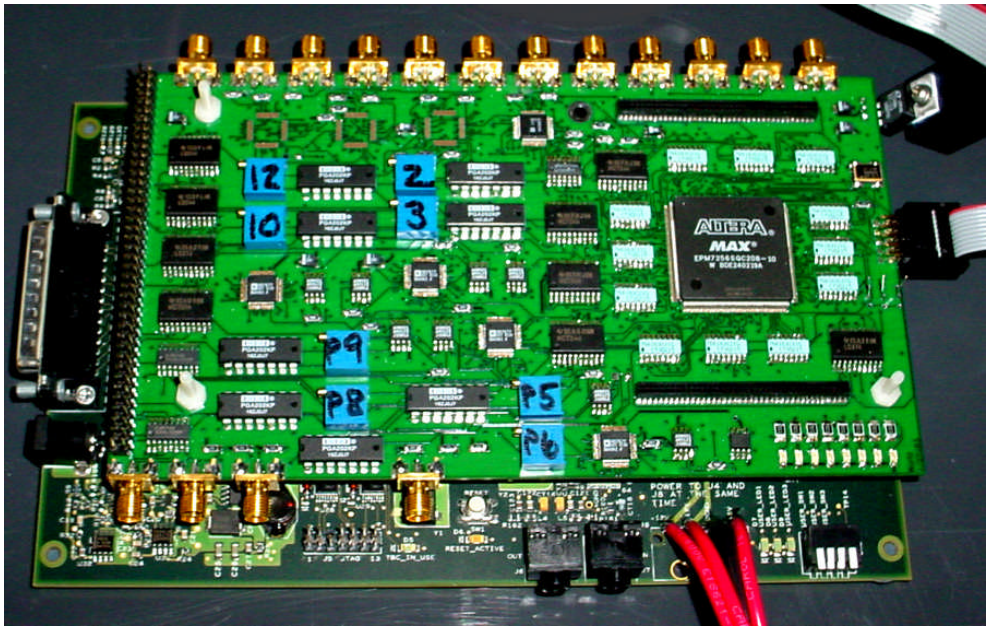

Figure 6.8 UA designed and constructed daughterboard for digital signal processing shown attached to the TI motherboard

7. FABRICATION

7.1 Summary

Successful development of the X-post gyro required major innovations in MEMS technology. The gyro is not a true MEMS device, but it is produced using MEMS technology. Depositing the several layers of materials, and then removing material to produce the needed configuration without shorting the electrodes required considerable work to master. First, the piezoelectric thin film must be nearly perfect, since it is only about a micron thick and defects will short the device between top and bottom electrodes. Also, the gyro is double-sided, not a common configuration in standard MEMS processing. It is hoped that the technology developed in this work will assist others who may face some of the same challenges with other future devices.

Fabrication of an X-post gyroscope requires the production and assembly of four components – an active wafer, two handle wafers, and a post. After fabrication of the components, the components are assembled to produce a device.

7.2 The Active Wafer

The active wafer is the most complex of the components of the X-post gyroscope. It contains the PNZT, the piezoelectric material used to form the actuators and sensors for the device. Another feature that complicates fabrication is the two-sided nature of the active wafer. The wafer stack is symmetric about the midplane of the wafer. As a result, when machining one side of the active wafer, the opposite side of the wafer must be protected.

The general approach used in producing an active wafer is to first build up a complete stack containing all of the needed material layers, and then systematically removing material to produce the desired geometry. We have used photoresist as the masking material to control where the various etches take place. We have procured 400 micron thick silicon wafers from Radiant Technologies that have been coated with a 5000 $\mathring{A}$ layer of SiO_2, a 400 $\mathring{A}$ layer of TiO_2, a 1500 $\mathring{A}$ layer of platinum, and a 1-1.2 micron thick layer of PNZT. To complete the wafer stack, the layers comprising the exterior electrodes -- a 200 $\mathring{A}$ thick layer of titanium, and then a 2500 $\mathring{A}$ thick layer of gold -- were deposited on both sides of the active wafer using an E-beam evaporator.

Patterning of the exterior electrodes is a fairly straightforward process. When patterning side 1, side 2 is first coated with a protective coat of photoresist. Side 1 is then coated with Shipley 1818 photoresist, and patterned using an appropriate chrome mask to define the electrode areas. A pictorial representation of an active wafer coated with photoresist and patterned with the UAA0 mask is shown in Fig. 7.1a. The gold and titanium that comprise the outer electrodes are etched away using commercial wet etchants (Transene TFA and Transene TFT, respectively). Figure 7.1b represents the appearance of the wafer after the wet etching of the gold and titanium layers.

Initial efforts to remove the PNZT focused on using a wet etchant (400 ml HCl, 400 ml H_2O, 8 g NH_4F) but this approach proved to be somewhat problematic. Figure 7.2a shows a portion of a test sample with a patterened exterior electrode and an overlapping layer of photoresist. The sample has not yet been exposed to the PNZT etchant. The square electrode is one millimeter on a side. We will pay special attention to the corner formed by one side of the electrode and one side of the photoresist, indicated by

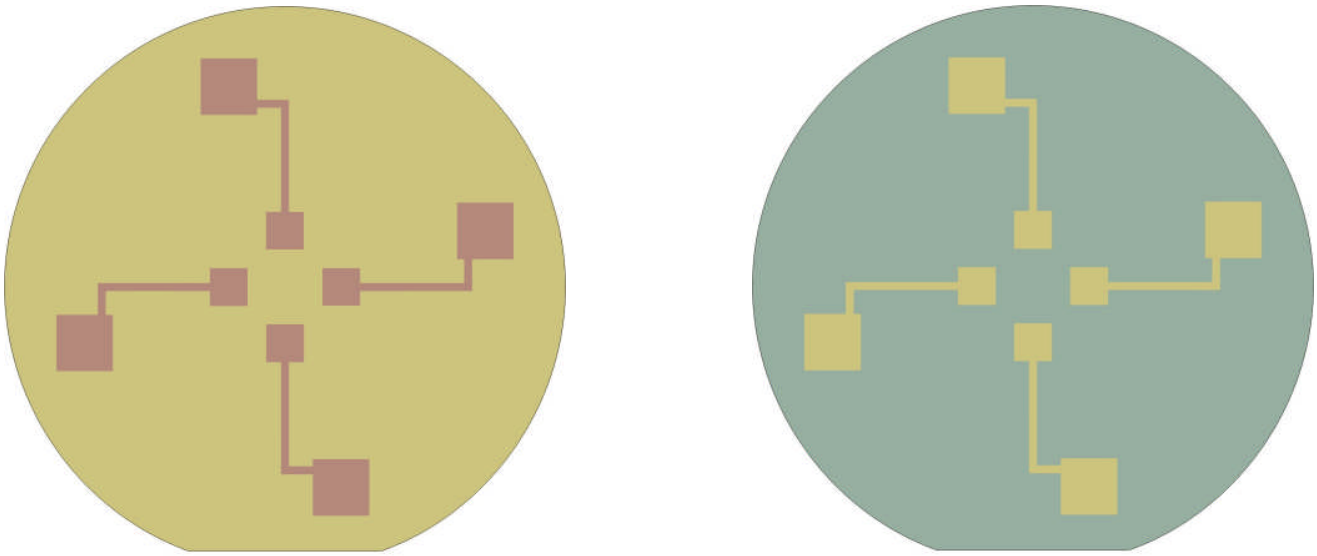

(a) (b)

Figure 7.1. Pictorial representation of the active wafer after (a) patterning photoresist with the UAA0 mask and (b) wet etching of the gold and titanium and subsequent stripping of the resist..

the arrow in the image. Figure 7.2b shows the SEM image obtained from just such a corner after the PNZT wet etch, and subsequent removal of the photoresist. What is seen is that there is considerable undercut in areas that were presumably protected by either the top electrode or the photoresist. In fact, the etchant has progressed farther laterally than it has downward toward the bottom electrode. When etching through the thickness of the PNZT, the etchant encounters an etch stop when it reaches the platinum layer. No such etch stop exists in the lateral directions. What is more, the etchant seems to "tunnel" along grain boundaries, allowing it to reach far under any protective layer before the PNZT can be completely removed where its removal is intended. In addition, a "flap" of gold that bends down

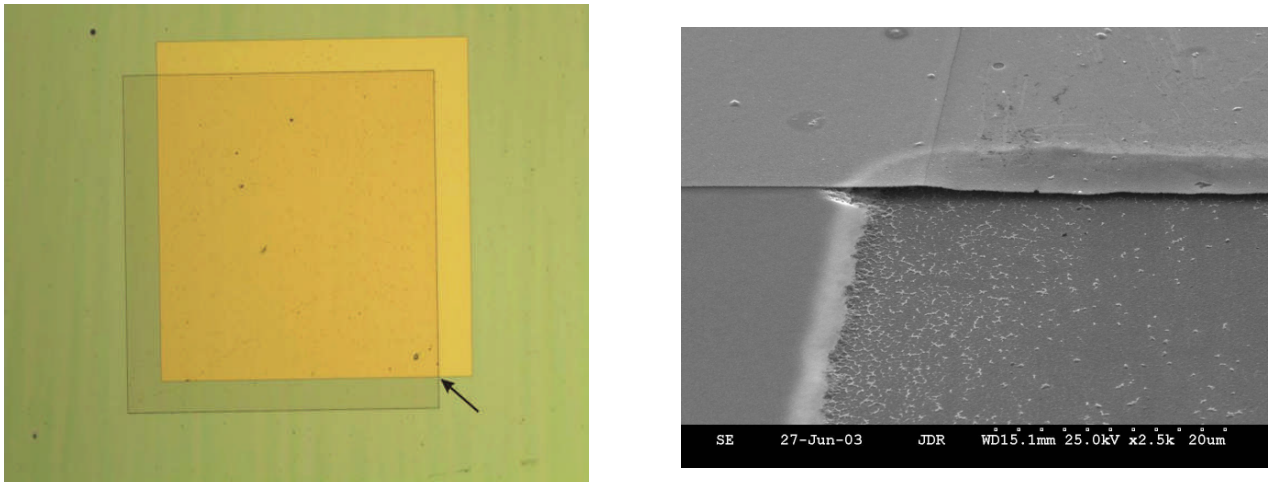

(a) (b)

Figure 7.2 (a) A PNZT etch test specimen with a patterned electrode and overlapping photoresist and (b) an SEM image taken near the corner identified in (a) between the top electrode and the offset photoresist after wet etching the PNZT and stripping the photoresist. (Image courtesy of Dr. Deanna McMillen, Aegis Technology Group, Huntsville, AL)

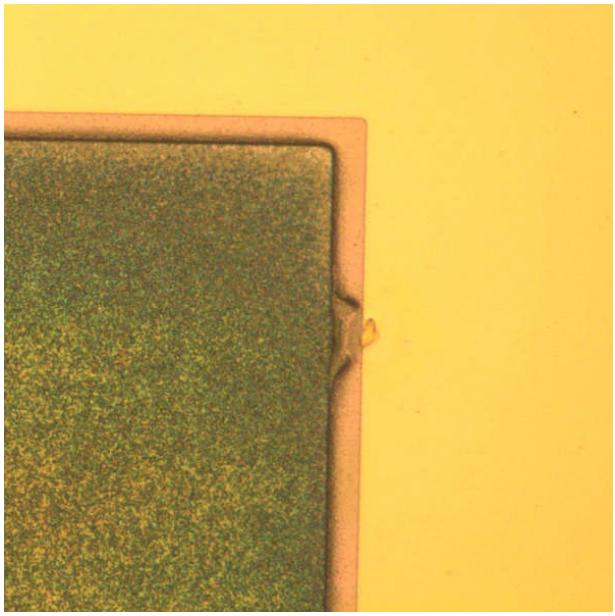

Figure 7.3 Micrograph showing preferential PNZT etch along a defect that led to shorting of the electrodes.

toward the bottom electrode is clearly visible. In fact, shorting of the two electrodes is quite a common occurrence when a wet etchant alone is used.

The first attempt to circumvent the severe undercut observed when using the wet etchant was to use an overlapping layer of photoresist. For our application, this approach did not prove successful. Figure 7.3 shows a micrograph of a region near the boundary one of the gold electrodes of an active wafer that had the PNZT partially etched away. The overlap of the photoresist about 12 microns beyond the boundary of the electrode is readily seen. The most conspicuous feature in the image is an indication of preferential etching along what appears to have been a defect in the PNZT film. This defect was not visible prior to the PNZT etch. When the PNZT etch was completed, this electrode was in fact shorted to the interior electrode. It is true that PNZT is used in the production of MEMS devices. But, in this case, our attempt to use a wet etchant only falls victim to the second significant complication associated with producing an X-post device – the device is large. When many devices are produced on a single wafer, the difficulty seen in Figure 7.3 may be tolerable, though it does produce a reduction in yield. Unfortunately, since at present only one X-post device can be produced per active wafer, our yield is binary, and this difficulty is not tolerable.

The process adopted to cope with the difficulties associated with the PNZT wet etch is as follows. To remove the PNZT from side 1 of the active wafer, the active wafer is bonded to a carrier wafer (a plain, single side polished, silicon wafer) with side 2 toward the carrier wafer using Shipley 1818 photoresist as a bonding agent. The carrier wafer serves to protect side 2 during several processing steps. Next, side 1 is coated with a thick (15 micron nominal) layer of Shipley 5740 photoresist. This photoresist is patterned using the UAA1 mask, which has been designed such that after patterning, the photoresist overlaps the exterior electrodes by 6 microns. The wafer at this stage of processing, with the patterned photoresist, is shown schematically in Fig. 7.4a. Ion milling is then used to remove 80-90 percent of the PNZT layer. After this ion milling step is complete, the photoresist is stripped for the wafer stack. Figure 7.4b shows a graphical representation of the wafer at this stage of processing.

Wet etching is used to remove the PNZT and expose clean platinum surfaces at five critical areas. These areas are the four pads used for accessing the interior platinum electrodes used for the sensors/actuators, and the central area which will ultimately be used for attaching the post. The wafer is coated with the 1818 photoresist, and patterned using the UAA2 mask. Figure 7.5a presents a graphical representation of the active wafer after the patterning of the photoresist. Note that only five areas are not covered by photoresist, and that as a result only these five areas are exposed to the etchant during the wet etch. Further, all of these areas are well removed from the gold outer electrodes. In fact, these exposed regions are at least 200 microns away from a gold pad or trace, so that the danger of undercut producing a short is eliminated. Figure 7.5b represents the active wafer after the wet etch has been conducted, and after the photoresist has been stripped from the wafer stack.

The next step in processing the active wafer is to remove the remaining PNZT, as well as removing platinum, TiO2, and SiO2 to reach the silicon at the center of the wafer in preparation for the deep etch that will complete the processing. In addition, final patterning of the interior electrodes and the bonding pad for the post is performed during this step. The wafer is coated with a thick layer of 5740 photoresist and patterned using the Level 3 mask. The wafer with patterned photoresist is shown schematically in Fig. 7.6a. Note that some lines have been included near the central pad. These lines are used to help in aligning the post when it is ultimately bonded to the device. Ion milling is used to remove the remaining PNZT, platinum, TiO_2, and SiO_2 in those areas not protected by the photoresist. Figure 7.6b is a graphical representation of the active wafer after this ion milling step and stripping of the photoresist.

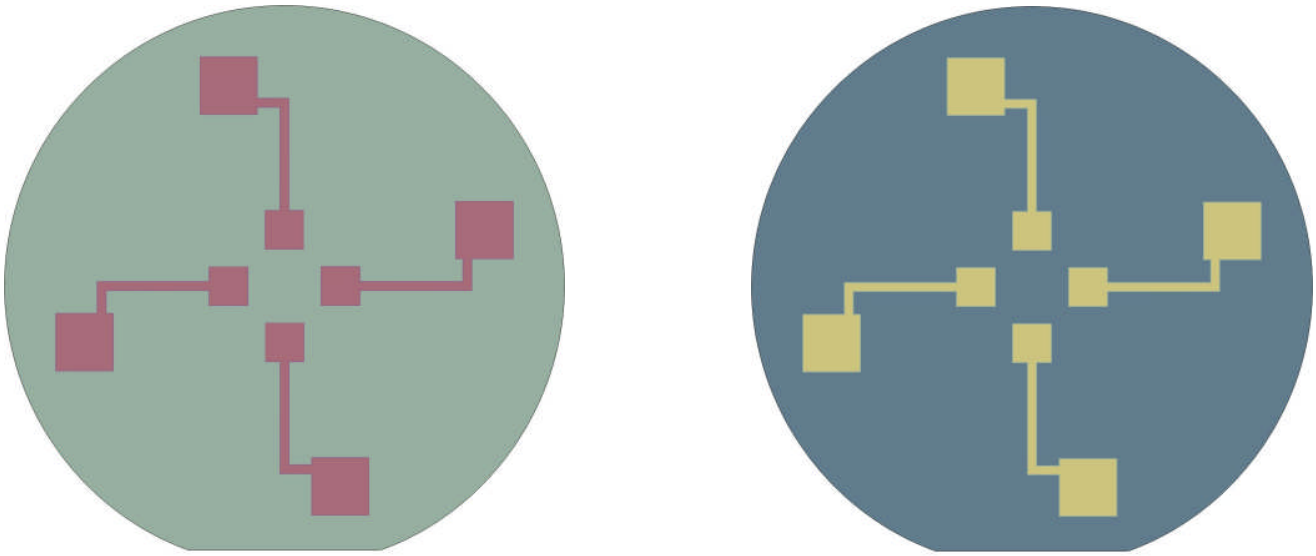

Figure 7.4 Pictorial representation of the active wafer after (a) patterning photoresist with the UAA1 mask and (b) after ion milling of the PNZT layer and subsequent stripping of the photoresist

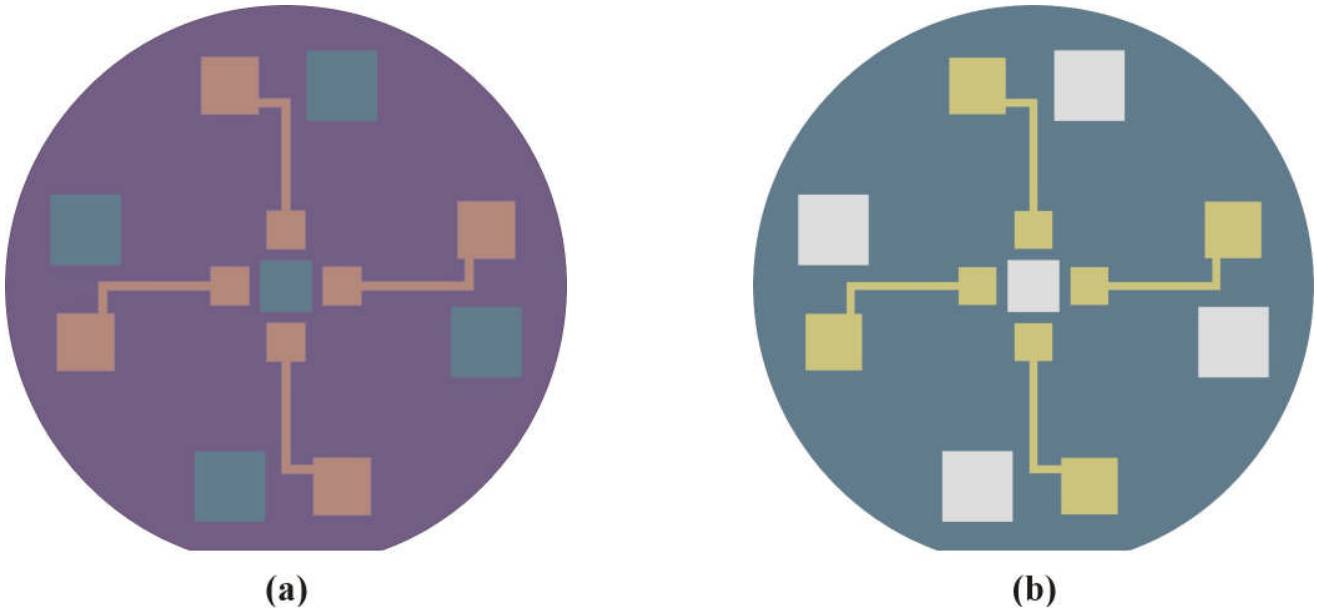

Figure 7.5 Pictorial representation of the active wafer after (a) patterning photoresist with the UAA2 mask and (b) wet etching of the PNZT layer and subsequent striping of the photoresist

The final step in fabricating the active wafer is to perform a deep etch through the central silicon layer. In preparation for this etch, the wafer stack is coated with a thick layer of 5740 photoresist, and patterned using the UAA4 mask, as shown in Fig. 7.7a. The deep etch is performed in a deep reactive ion etcher (DRIE), the STS Advanced Silicon Etcher, that uses the Bosch process to produce vertical sidewalls, as the process produces very little undercut. Note that four "angles" will be cut free from the rest of the wafer when the deep etch is complete. The features to be removed were outlined with 80 micron trenches because a recipe was already known for performing very deep etches of 80 micron trenches that would have essentially vertical side walls. Once the deep etch is completed, the photoresist

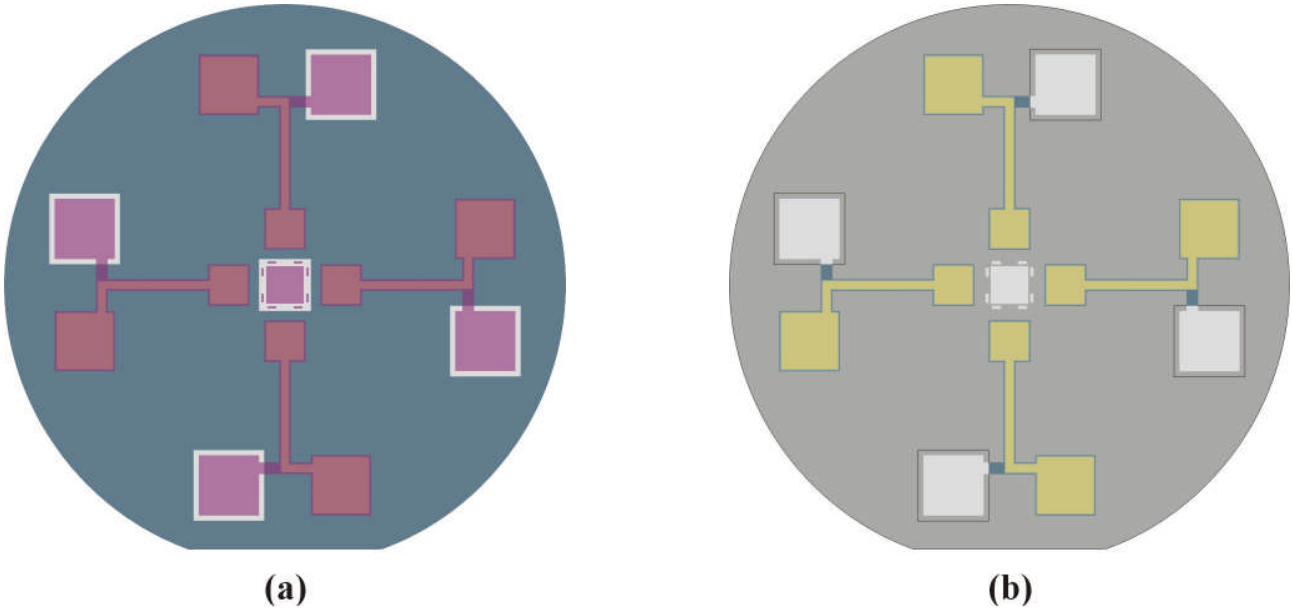

Figure 7.6 Pictorial representation of the active wafer (a) after patterning of photoresist with the UAA3 mask and (b) after ion milling to the silicon and subsequent striping of the photoresist

is stripped from the wafer stack, and the stack is soaked in acetone to release the active wafer from its carrier wafer. Figure 7.7b is a graphical representation of the completed active wafer.

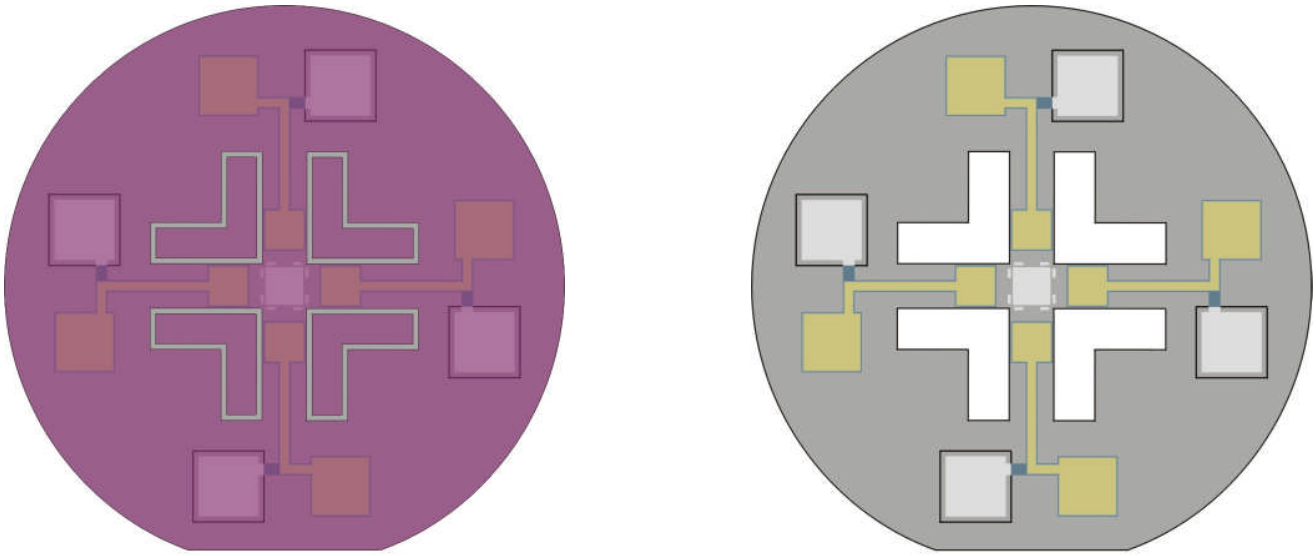

Figure 7.7 Pictorial representation of the active wafer after (a) patterning photoresist with the UAA4 mask and (b) completion of the deep etch and release of the wafer from its carrier wafer.

7.3 The Handle Wafers

To begin fabrication of a handle wafer, a plain silicon wafer is coated with 300 $\overset{o}{A}$ thick layer of chrome. The deposition of the chrome is perfomed using the E-beam evaporator. After patterning, this chrome layer provides a set of alignment marks that will be used in subsequent processing steps.

Next, a layer of 1818 photoresist is spun on the wafer, and patterned using the UAH0 mask. Figure 7.8a shows the handle wafer after patterning of the photoresist. While the real purpose of the chrome layer is to provide alignment marks (which are not shown in the graphic as they are very small) for later steps, the chrome must be removed in other areas to allow silicon etching in the DRIE. If the chrome were not removed, it would serve as a very effective mask prohibiting the silicon etch. Figure 7.8b shows the handle wafer after chrome etching and stripping of the photoresist.

Next, a layer of photo-definable polyimide is spun on the wafer. This polyimide will ultimately serve as the adhesive that bonds the handle wafer to the active wafer. The polyimide is HD Microsystems 2723 photo-definable polyimide. The spin is selected such that after the initial soft bake (3 min. at 110^{o}C), the polyimide is about 3.4 microns thick. Next, the wafer is patterned using the UAH1 mask. The polyimide is then developed in a dynamic process performed on the spinner. After development, the wafer is subjected to a higher temperature bake (10 min. at 270^{o}C). During this bake, the polymer undergoes some reflow. The thickness of the polyimide features after this step is about 2.2 microns. A pictorial representation of the handle wafer at this point is shown in Fig. 7.9. The polyimide is patterned such that there are “channels” where the polyimide is removed, and “stripes” where the polyimide remains. The channels ensure adequate venting during the bonding step, so that volatiles that may be driven off during that step are not trapped between the wafers.

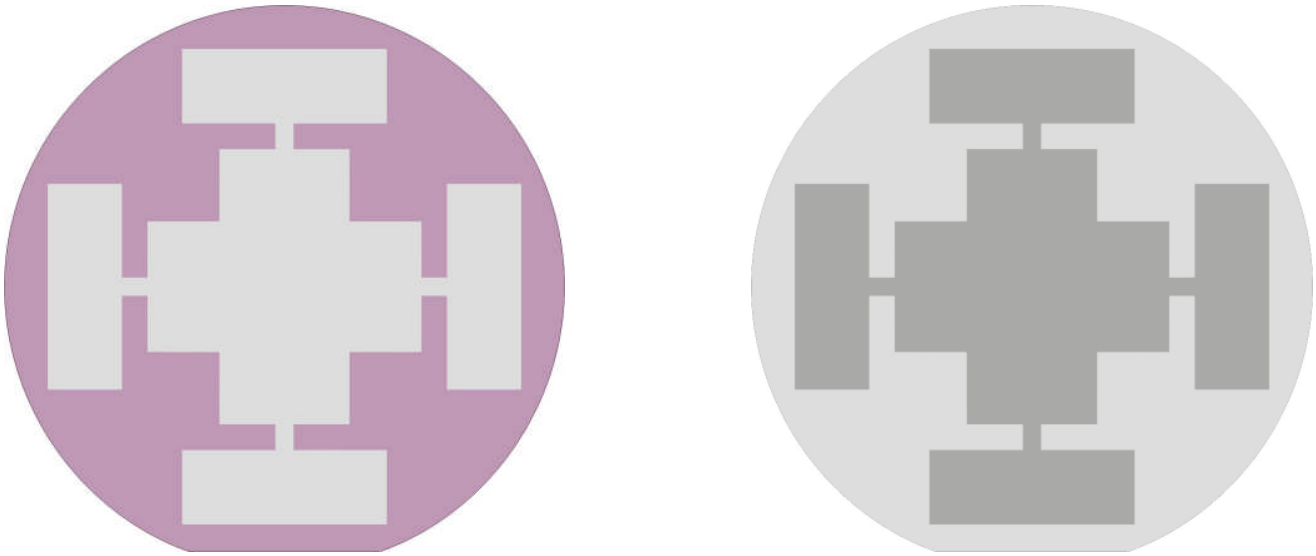

Figure 7.8. Pictorial representation of the handle wafer after (a) patterning photoresist with the UAH0 mask and (b) completion of the chrome etch and subsequent stripping of the photoresist.

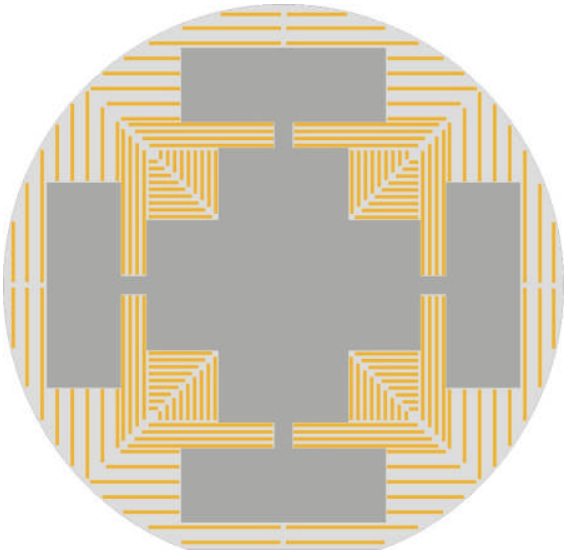

Figure 7. 9 Pictorial representation of the polyimide layer on the handle wafer after patterning with the UAH1 mask.

The next processing steps involve etching into the silicon using the DRIE. In preparation for these steps, the handle wafer is bonded, polyimide side out, to a carrier wafer using photoresist as an adhesive. Next, a coat of 5740 photoresist is spun on to the wafer, and patterned using the UAH2 mask. A pictorial representation of the handle wafer at this point is presented in Fig. 7.10a. Note that four small rectangular areas of silicon are exposed. A relatively "shallow" silicon etch (12 microns deep) is performed in the DRIE at this point. The four rectangular regions exposed to the etching plasma become "trenches" that accommodate the conductive traces in the active wafer. The trenches prevent the outer electrodes in these traces from shorting via contact with the silicon in the handle wafer. Figure 7-10b shows the handle wafer at the conclusion of this processing step.

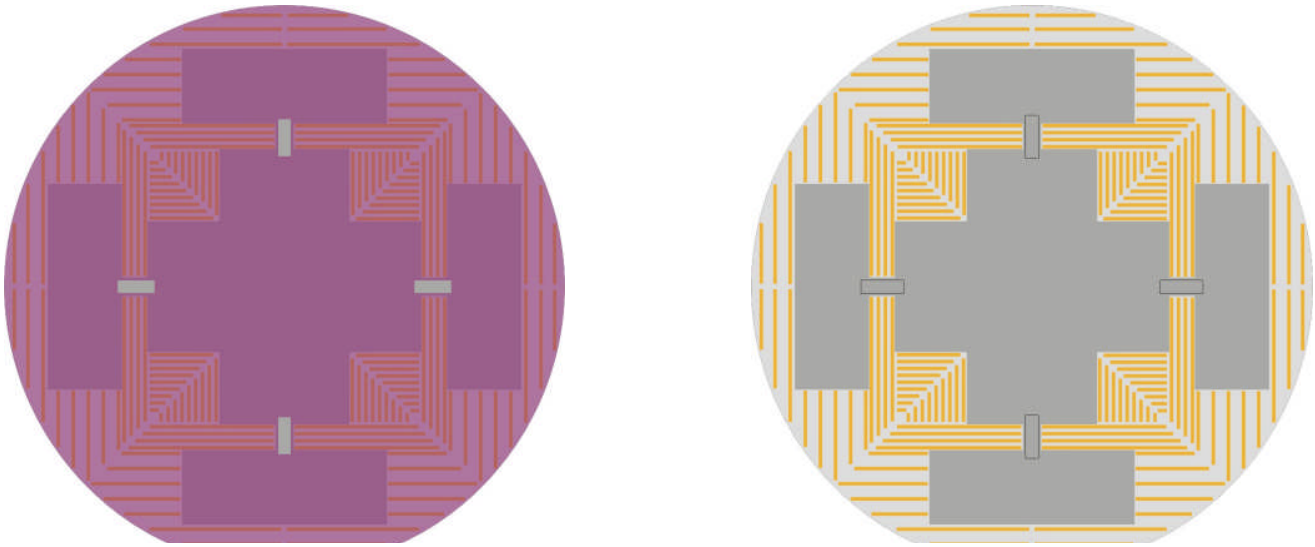

Figure 7.10 Pictorial representation of the handle wafer after (a) patterning photoresist with the UAH2 mask and (b) completion of the shallow silicon etch and subsequent stripping of the photoresist.

Finally, the handle wafer is prepared for a deep silicon etch through the full thickness of the wafer. The wafer is coated with a thick layer of 5740 photoresist, and patterned using the UAH3 mask, as shown in Fig. 7.11a. As was done with the active wafer, the areas to be removed are outlined with lines that are 80 micron wide. Note that in addition to the central area where the crossing arms are located in the active wafer, four additional rectangular areas will be removed. These areas allow access to the electrodes on the active wafer. Figure 7.11b shows the completed handle wafer.

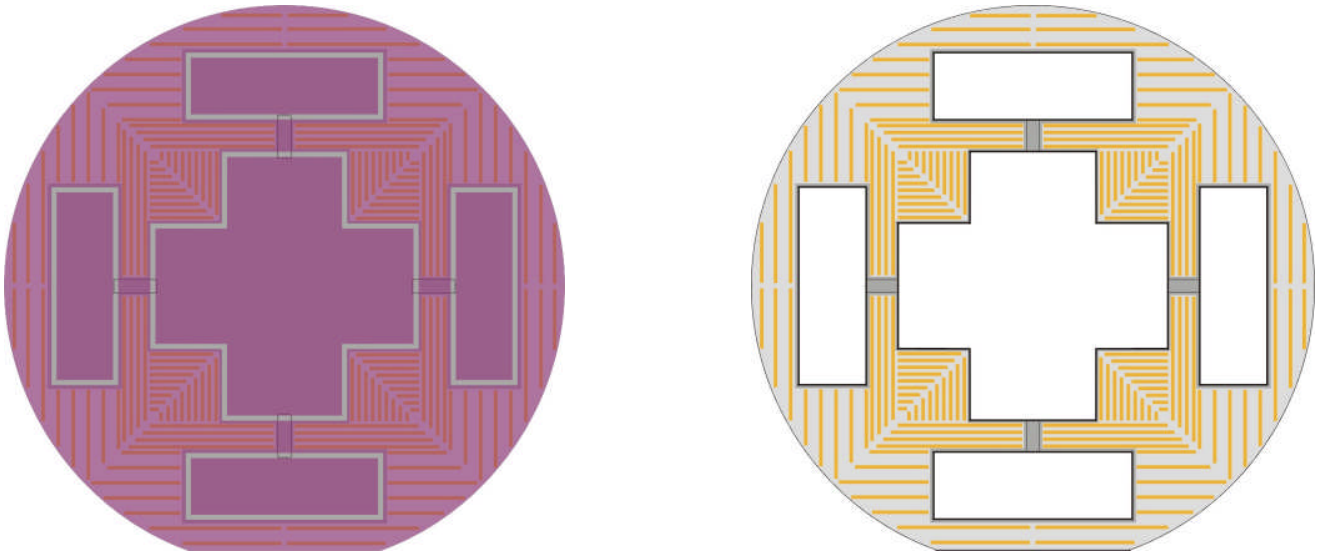

Figure 7.11 Pictorial representation of the handle wafer after (a) patterning photoresist with the UAH3 mask and (b) completion of the deep silicon etch and subsequent release of the handle wafer from its carrier wafer.

7.4 Wafer Bonding

Assembly of an X-post gyroscope begins with the bonding of two handle wafers to an active wafer. The bonding was performed using facilities at the Weapon Sciences Integrated Devices group at AMCOM in

Huntsville. The key piece of equipment used in this processing step was a bond aligner equipped with two vacuum chucks – one to hold the upper substrate, and one to hold the lower substrate. Infrared microscopes permit viewing through the silicon to view alignment marks on the substrates. Micrometer controls facilitate aligning the two substrates, and then bringing the substrates into contact with each other. The joined substrates are then carefully moved to a hot plate, and placed under pressure, and then subjected to elevated temperature to allow the polyimide that is acting as a bonding agent to flow.

The first step in assembling the three wafer stack was to bond the active wafer to a handle wafer. This process is illustrated schematically in Fig. 7.12. The two wafers were aligned, and then brought into contact. After placement on the hot plate, "pressure" was applied to the stack via the application of dead weight. The stack was then tacked together via heating to a temperature of 330^{o}C, and then being allowed to cool to room temperature. At this point, the wafers were attached to each other, forming a

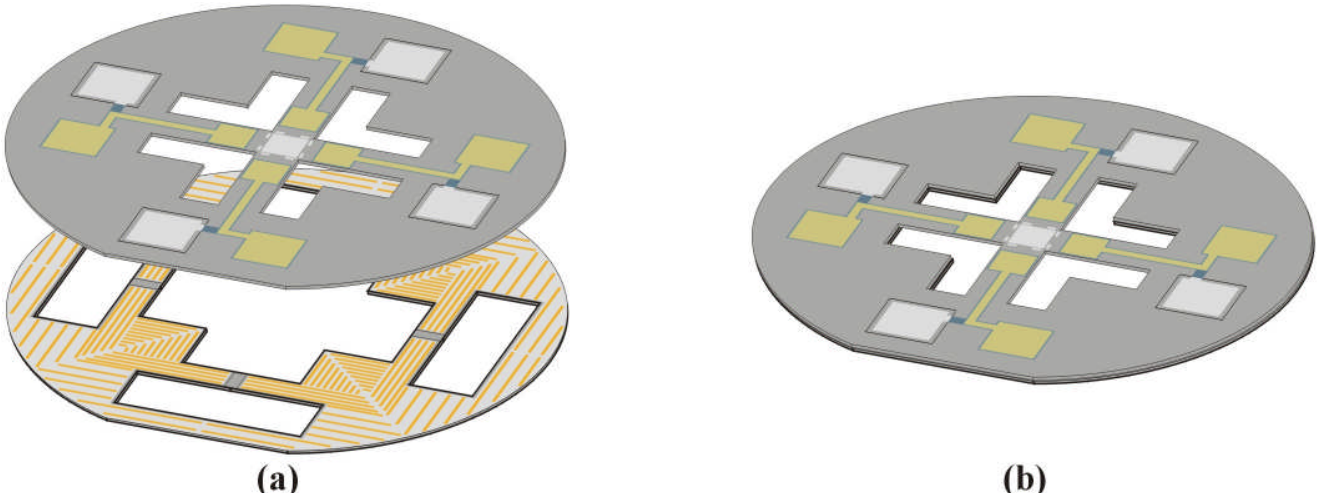

Figure 7.12 (a)Wafer bonding begins with the alignment of the active wafer with a handle wafer. (b) Once the wafers are tacked together, the result is a two wafer stack.

two wafer stack.

The second step was to bond another handle wafer onto the two wafer stack. This process is indicated schematically in Fig. 7.13. Once again, the tacking procedure described above was performed so that all three wafers were adhered into a single stack. The last stage of wafer bonding was to put the three wafer stack in a vacuum bonding jig for final bonding. The vacuum bonding jig ensures that a uniform pressure roughly equal to atmospheric pressure squeezes the wafers together during final bonding. The temperature is raised to 350^{o}C during this final bonding step.

7.5 Fabricating and Bonding the Post

Silicon posts having dimensions 2 mm by 2 mm by 4 mm were fabricated from a 2 mm thick silicon wafer. The wafer was placed on an adhesive mount in a computer controlled dicing saw. A series of saw cuts were made such that the cuts were spaced by 4 mm plus the kerf of the saw blade. Next, the wafer was rotated 90^{o}. A second series of cuts, this time with a spacing equal to 2 mm plus the kerf of the saw blade, was made. This procedure yielded numerous 2 mm by 2 mm by 4 mm posts. However, the ends of the posts were not as smooth as desired. The posts were stood on end and "glued" together using a thermoplastic wax. Once bonded together, the ends of the posts were polished to remove any saw marks. After polishing, the assemblage of posts was soaked in a solvent to remove the thermoplastic, and free the individual posts.

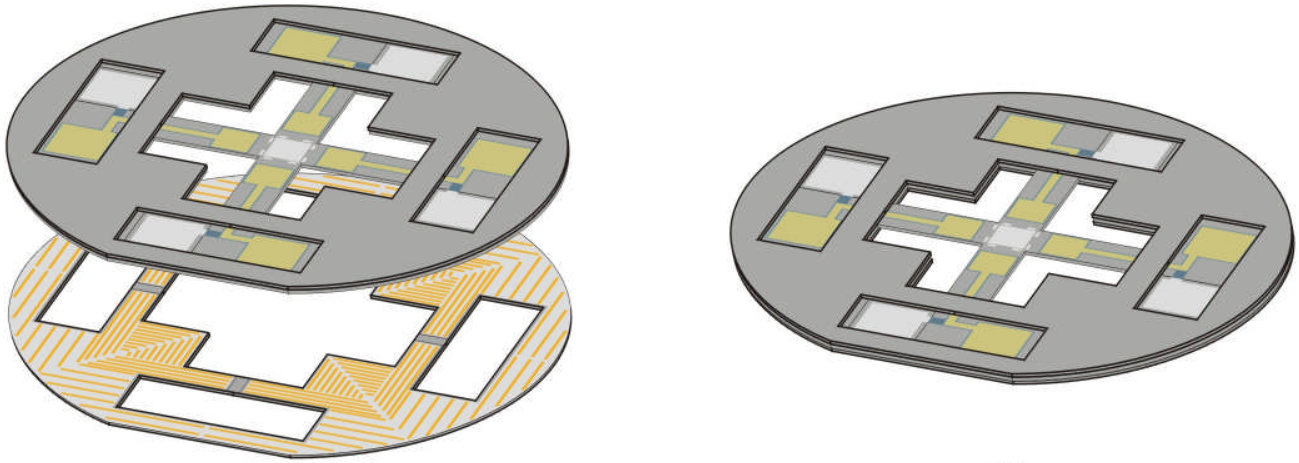

Figure 7.13 (a) The second handle wafer is aligned with the two wafer stack. (b) After final bonding, the three wafer stack is complete.

To complete the basic x-post device, a post was bonded to the center of the cross in the three wafer stack. A small drop of epoxy was placed on the central target area. Then the post was carefully placed on the epoxy drop, taking care that the faces of the post aligned nicely with the alignment marks provided near the central 2mm by 2mm platinum pad at the center of the cross. The post bonding process is illustrated schematically in Fig. 7.14.

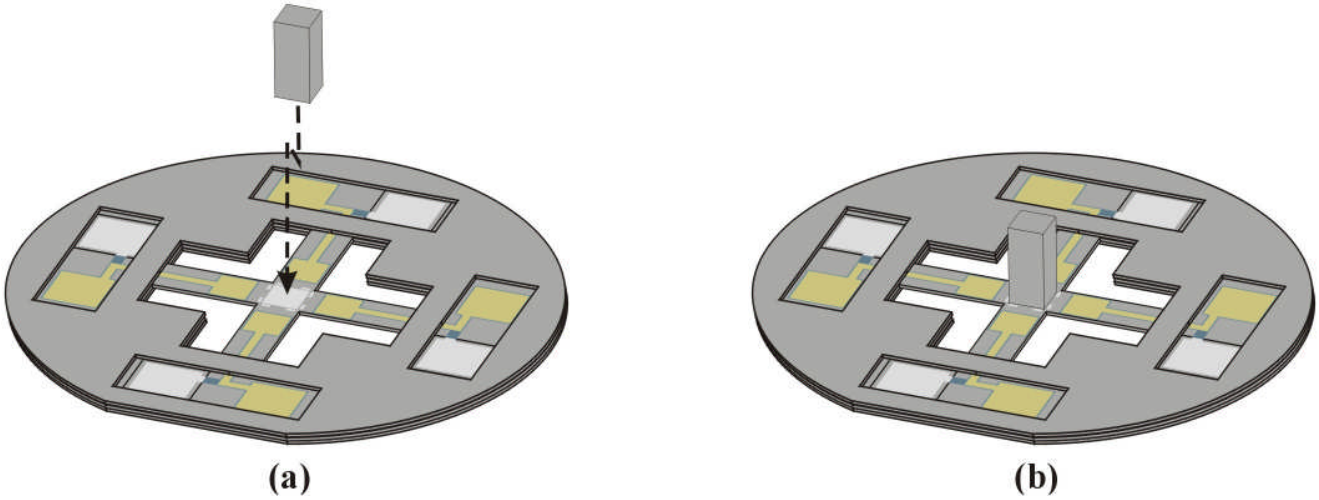

Figure 7.14 (a) The post is carefully placed at the center of the cross. Epoxy is used as an adhesive. (b) After the epoxy has cured, the basic x-post device is complete.

7.6 Final Assembly

Although the basic sensor was complete at this point, some additional assembly was required to make the device functional. First, the completed sensor was glued to a stainless steel plate using an RTV adhesive to facilitate handling. Next, wires were connected to the various conductive pads of the sensor using a conductive epoxy. The other ends of these wires were soldered to copper tabs that had been placed around the perimeter of the steel plate. The stainless steel plate assembly was then fastened to an aluminum plate that serves as a mount for the rate table. The device was now ready for testing. A photograph of completed device UA-11 is shown in Fig. 7.15.

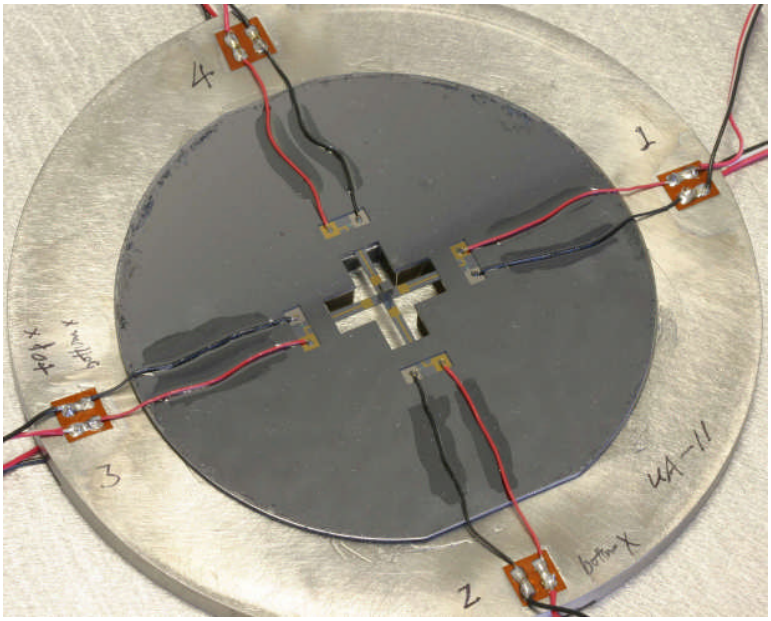

Figure 7.15 Photograph of completed X-post device UA-11.

8. TESTING THE X-POST DEVICE

8.1 Summary

Near the end of the project we were able to test the first X-post gyro design. This section explains the testing done and the status of the device. With a small grant obtained since the end of the FAA project, we are attempting to correct some of the deficiencies we have seen in the initial device. New masks are being produced with the goal of testing the next generation design. Better electrical shielding will be provided and an attempt to reduce parasitic capacitance will tried by reducing electrode size. If possible, laser trimming will be attempted.

8.2 Poling the PNZT

To prepare the x-post gyroscope for testing, it is first necessary to pole the PNZT. During poling, an alternating electric field is applied across the thickness of the PNZT to help align the polarization vectors associated with the various grains that comprise the PNZT layer. Poling increases the piezoelectric effect. Work with test samples had indicated that it was possible to pole using a peak voltage of about 15 V across the PNZT layer without producing shorting across the PNZT. Unfortunately, in the completed x-post devices, this degree of poling was not possible. If the poling voltage was increased above 4-5 V, shorts developed. To produce a working device, it was necessary to limit the poling voltage to about 4 V maximum, and accept a corresponding reduction in piezoelectric properties of about a factor of 5 compared to the test samples that had been poled to a full 15 V. The net effect on gyro performance is a reduction by a factor of about 25 from what was expected, as the reduction in properties influences both the strength of excitation produced when driving a piezo, and the sensitivity to deformation when sensing gyro output.

One reason for the discrepancy between behavior of the test samples and that of the actual devices is that the electrodes on the test samples were quite small, whereas the electrodes on the x-post are very large. Each gold-coated area on the x-post device has a 2 mm square pad near the center that acts as an actuator, and a 3mm square pad away from the center that serves as an electrical contact. The two squares are connected by a 0.4 mm wide trace. The total area of each electrode is quite large, increasing the probability that the electrode will cover some “weak” area where a short might develop. In addition, the test samples were not subjected to the full array of processing steps required to make the x-post device. It is possible that one of the processing steps could affect the structure or properties of the PNZT layer. Further study is required to resolve this question as to whether or not wafer processing affects the PNZT.

8.3 Device Testing

Some data was acquired form each of three devices and the trends were very consistent from device to device. It was possible to get each device to oscillate by applying a drive signal. Further, the resonant peak occurred at essentially the same frequency predicted by the finite element analysis. However, the output signals sensed when the oscillations were induced, were quite small. And another physical phenomenon also contributed to the output signal.

To assist the discussion of the results, Fig. 8.1 shows a plan view of an x-post gyroscope with the various arms of the device identified with numbers. In this view, the post is projecting up out of the plane of the active wafer. The side to which the post is bonded is referred to as the top side of the device.

When testing the device, a drive signal was applied to one arm of the device. The drive signal was a

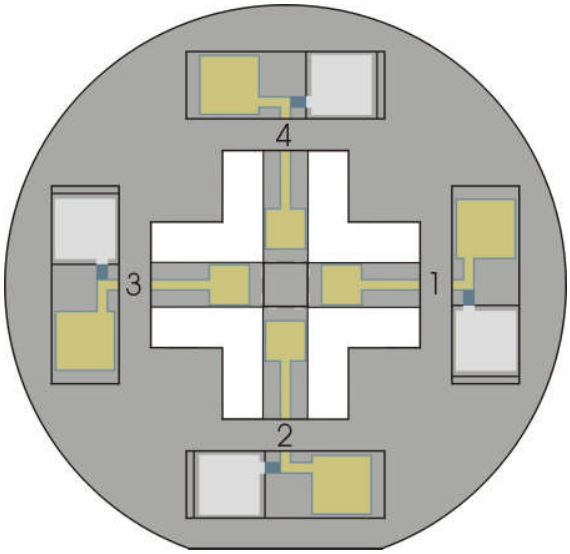

Figure 8.1. Plan view of completed X-Post device identifying the four arms of the device. The post sticks up out of the page in this view.

sinusoidal signal varying oscillating between 0 V and the peak voltage. For the testing described here, a peak voltage of 4 V was used. Thus, the input signal was 4 V peak to peak, with a mean value of 2 V. The drive signal was applied using a function generator so that it was easy to sweep through a range of frequencies to get the frequency response of the device. Output from the arm (and associated piezo) that was used as the sensor was amplified first by a charge amplifier using a gain of 1000. The output of the charge amplifier was fed into a lock-in amplifier that provided an additional gain of 100. Thus, total amplification for the sense electronics was 100,000.

Figure 8.2 shows the frequency response of UA-11 when the drive signal was applied to the piezo on the bottom side of arm 4, and the output was sensed from the top piezo on arm 2. The plot clearly shows a resonant peak that occurred at about 12.45 kHz. The resonant peak is superposed on top of a curve in which the sensed amplitude increases with increasing frequency, a curve indicative of parasitic capacitance between the trace used for driving the device and the trace used to sense the output. The resonant peak is quite small, only 1 mV produced by a 4 V input. And the sensor is aligned with the intended rocking motion of the device, so this signal should be relatively large. It is also clear that the effect of the parasitic capacitance is of similar magnitude to the piezoelectric induced response indicated by the resonant peak. If it had been possible to pole the piezo layers to a significantly higher voltage, the magnitude of the piezoelectric induced response would have increased significantly (by a factor of 25 or so), while the while the effect of the parasitic capacitance would remain unchanged. This would have made it much simpler to isolate the response associated with mechanical vibration of the sensor.

Figure 8.3 shows the response of UA-11 to the same 4 V peak to peak input applied to the bottom piezo of arm 4 described above, but this time the output was being sensed on the top piezo on arm 1 of the device. Under ideal circumstances, this sensing piezo would produce zero output in the absence of rotation. The plot shows that there is some indication of a resonant peak, although the strength of that peak is somewhat smaller that what was seen in Fig. 8.2. This indicates that the sensor is out of trim – the vibration modes do not line up with the two “axes” defined by the arms of the gyro. As a result, driving the piezo on the bottom excites two rocking modes. And once again, the effect of the parasitic capacitance is evident in Fig. 8.3.

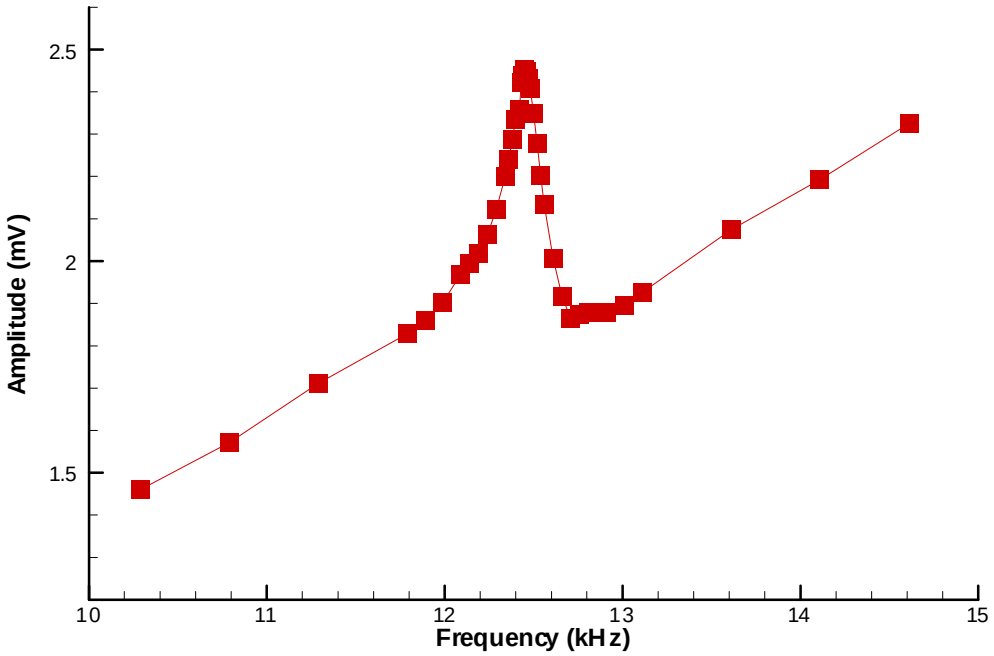

Figure 8.2 Frequency response of UA-11 when driving piezo 4 bottom and sensing piezo 2 top.

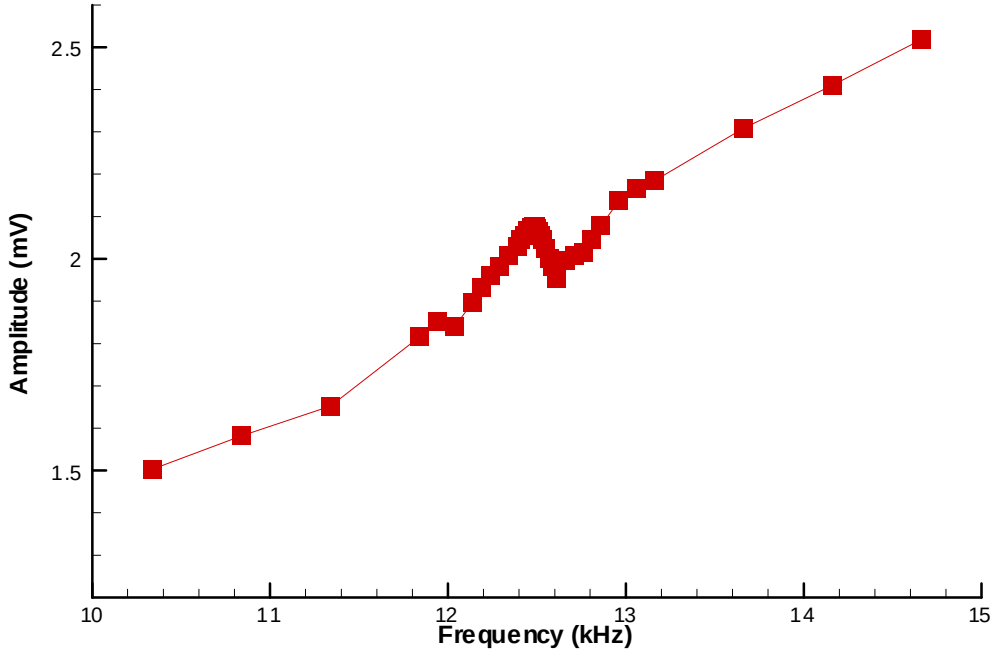

Figure 8-3 Frequency response of UA-11 when driving piezo 4 bottom and sensing piezo 1

To this point, efforts to measure a rotation rate with the device have been unsuccessful. The piezoelectric effect is somewhat weak because poling could not be carried out as effectively on the devices as on the test samples, so that even the response in the drive axis is rather small. The response due to rotation is expected to be two to three orders of magnitude smaller than the response due to the

forced oscillations. Finally, the magnitude of the parasitic capacitance has made it difficult to isolate that part of the response caused by mechanical vibrations.

To get the best possible gyro performance, some effort must be made to mechanically "trim" the resonator so that it more closely follows the ideal response. Both mechanical trimming and electronic trimming are required to achieve the best performance. We have established a laser trimming system to do the trimming but expiration of the project precluded its use.

APPENDIX A: Wafer Traveler for Active Wafer

AMCOM – REDSTONE

UA Gyro Wafer Process -- Active Wafer Lot #:
#Wafers/Lot: 5

Wafer :
Purpose:
Targets:

PROCESS FLOW

PROCESS	**DECRIPTION**	**ITL**	**DATE**	**COMMENTS**
ACTIVE WAFER				
RUN START	Radiant Technologies PNZT/Pt/TiO_2/SiO_2/Si/SiO_2/ TiO2/Ti/Pt/PNZT _?_Å/1500Å/400Å/5000Å… Lot # _____ 3" Si ___ type, ____ohm-cm, Orientation: <1-0-0> Wafer Thickness: 400 micron Order # Date:			
METALIZATION SIDE I	Evaporate 200Å Ti then 2500Å Au **E-Beam Evaporator** **Ti: Deposit. Rate: 0.5** Å **/s E-beam Power: 7.5%** **Au: Deposit. Rate: 5** Å **/s E-beam Power: 32%**			
POST METAL DEPOSITION INSPECTION	Examine for macroscopic defects.			
METALIZATION SIDE II	Evaporate 200Å Ti then 2500Å Au **E-Beam Evaporator** **Ti: Deposit. Rate: 0.5** Å **/s E-beam Power: 7.5%** **Au: Deposit. Rate: 5** Å **/s E-beam Power: 32%**			
POST METAL	Examine for macroscopic			

DEP. INSPEC.	defects.			
RESIST COAT SIDE II	1818, Prog 2 , 2500 rpm/30s for back side protection			
RESIST BAKE SIDE II UP	40 min@ 125 °C in oven			**Needs to be long/hot for back side protection**
RESIST COAT SIDE I	1818, Prog. 2 , 2500 rpm/30 s			
RESIST SOFT BAKE SIDE I UP	100 ˚C, 30 min in oven (hotplate cannot be used with 1045 resist on back side)			**Too low a temp may give wrinkled look to resist edges.**
EXPOSE SIDE I	**Mask: UAA0_R04** Karl Suss Contact Aligner Program: Vacuum Contact Exposure time: 6 s (No alignment. Just center wafer chuck)			
DEVELOP	MP Developer (diluted 1:1). 1 min			
POST PATTERN LITHO INSPEC.	Examine for litho errors or defects; note severity on map			
RESIST HARD BAKE SIDE I UP	125 ˚C, 30 min in oven			
DESCUM	3 min. at 300 W in YES-R3			
GOLD WET ETCH	45 sec TFA visual endpoint detection			
POST GOLD ETCH INSPECTION	Examine with microscope to insure that all gold has cleared and that edge of features look good			**Measure Gold feature sizes here.**
Ti WET ETCH	Transene TFT Ti Etchant w/ a 1:30 dilution. Etch 45s. @ Rm temp. 2step rinse.			
POST Ti ETCH INSPECTION	Examine to insure that all Ti has cleared and that edge of features look good			
RESIST STRIP SIDE I	Strip on spinner with Acetone and IPA			
DESCUM SIDE I	3 min. at 300 W in YES-R3			
RESIST STRIP SIDE II	Strip on spinner with Acetone and IPA			
DESCUM SIDE II	3 min. at 300 W in YES-R3			
RESIST COAT SIDE I	1818, Prog 5 , 2500 rpm/60s for back side protection			
RESIST BAKE SIDE I UP	40 min@ 125 °C in oven			**Needs to be long/hot for back side protection**

RESIST COAT SIDE II	1818, Prog. 2 , 2500 rpm/30 s			
RESIST SOFT BAKE SIDE II UP	100 ˚C, 30 min in oven (hotplate cannot be used with 1045 resist on back side)			**Too low a temp may give wrinkled look to resist edges.**
EXPOSE SIDE II	**Mask: UAA0_R04** Karl Suss Contact Aligner Program: Vacuum Contact Exposure time: 6 s Use Back Side Alignment			
DEVELOP	MP Developer (diluted 1:1). 1 min			
POST PATTERN LITHO INSPEC.	Examine for litho errors or defects; note severity on map			
RESIST HARD BAKE SIDE II UP	125 ˚C, 30 min in oven			
DESCUM	3 min. at 300 W in YES-R3			
GOLD WET ETCH	45 sec TFA visual endpoint detection			
POST GOLD ETCH INSPECTION	Examine with microscope to insure that all gold has cleared and that edge of features look good			**Measure Gold feature sizes here.**
Ti WET ETCH	Transene TFT Ti Etchant w/ a 1:30 dilution. Etch 45s. @ Rm temp. 2step rinse.			
POST Ti ETCH INSPECTION	Examine to insure that all Ti has cleared and that edge of features look good			
RESIST STRIP SIDE II	Strip on spinner with Acetone and IPA			
DESCUM SIDE II	3 min. at 300 W in YES-R3			
RESIST STRIP SIDE I	Strip on spinner with Acetone and IPA			
DESCUM SIDE I	3 min. at 300 W in YES-R3			
RESIST COAT CARRIER WAFER	1818, 2500 rpm/30s for bonding carrier wafer to active wafer			
BOND CARRIER WAFER TO ACTIVE WAFER	Place carrier wafer (resist side up) on bonding jig. Place active wafer (Side I up) on top of carrier wafer. Place top plate on jig. Put jig on hot plate preheated to 70°C. Hold at 70°C for 5 min., ramp to 125°C for 30 min., hold at 125°C for 30 min., ramp down to 70°C for 30 min.			

CLEAN STACK	Strip on spinner with Acetone and IPA			
RESIST COAT	SJR-5740 – Spin using 3 s spread at 400 rpm, followed by a 2000 rpm spin for 10 s. Allow 10 minutes of "relaxation time" at RT prior to baking.			**Resist thickness should be about 15 microns.**
RESIST SOFT BAKE	100 ˚C for 37 min in oven.			
REHYDRATION	Allow at least one hour for the 5740 photoresist to rehydrate prior to patterning.			
EXPOSE SIDE I	**Mask: UAA1_R04** Karl Suss Contact Aligner Program: Soft Contact Exposure time: 104 s (4 reps of 26 s, with 10 s pauses) **Dose=1360 mJ/cm^2 for 365 nm light.**			
DEVELOP	MF-453 Developer (undil.) for 15-20 min.			**Check every 10 minutes or so of developing time to see if resist has cleared.**
POST PATTERN LITHO INSPEC.	Examine for litho errors or defects; note severity on map			
PAINT W/ RESIST	Paint over the alignment marks and any other litho defects with 5740 resist. Paint around edge with 1818 resist.			
BAKE	Bake for 90 min. at 100^{o}C			
DESCUM	3 min. at 300 W in YES-R3			
ION MILLING OF PNZT – SIDE I	Accelerating voltage: 500 V Beam Current: 40 mA Time: 75 minutes Etch rate approx. 80 Å^o/ min.			**Objective here is to remove 80-90% of PNZT via this dry etch. Done in two or three steps, to monitor etch depth.**
POST-MILL INSPECTION	Check milled depth using the Dektak.			
DESCUM	3 min. at 300 W in YES-R3			
RESIST STRIP	Strip on spinner with Acetone and IPA			
DESCUM	3 min. at 300 W in YES-R3			
RESIST COAT	1811, Prog. 2 , 2500 rpm/30 s			
RESIST SOFT BAKE	100 ˚C, 30 min in oven			**Too low a temp may give wrinkled look to resist edges.**
EXPOSE	**Mask: UAA2_R04** Karl Suss Contact Aligner Program: Vacuum Contact Exposure time: 6 s			
DEVELOP	MP Developer (diluted 1:1). 1 min			
POST PATTERN LITHO INSPEC.	Examine for litho errors or defects; note severity on map			

PAINT W/ RESIST	Paint over the alignment marks and any other litho defects with 1818 resist. Paint around edge with 1818 resist.			
BAKE	Bake for 90 min. at 100°C			
DESCUM	3 min. at 300 W in YES-R3			
WET ETCH PNZT	**400ml H2O,400ml HCl + 8g NH4F Etch rate~400nm/min**			**DON'T OVERETCH!!! CAREFUL**
RESIST STRIP	Strip on spinner with Acetone and IPA			
DESCUM SIDE I	3 min. at 300 W in YES-R3			
INSPECTION OF METAL PATTERN SIDE I	Examine pattern with optical microscope, note defects and severity on defect map			
Microscope and MULTIMETER TEST	Use multimeter to ensure top electrodes and Pt bottom electrode are not in contact			**Measure PNZT Stack feature size here.**
RESIST COAT	SJR-5740 – Spin using 3 s spread at 400 rpm, followed by a 2000 rpm spin for 10 s. Allow 10 minutes of "relaxation time" at RT prior to baking.			**Resist thickness should be about 15 microns.**
RESIST SOFT BAKE	100 ˚C for 37 min. in oven.			
REHYDRATION	Allow at least one hour for the 5740 photoresist to rehydrate prior to patterning.			
EXPOSE SIDE I	**Mask: UAA3_R04** Karl Suss Contact Aligner Program: Soft Contact Exposure time: 104 s (4 reps of 26 s, with 10 s pauses) **Dose=1360 mJ/cm^2 for 365 nm light.**			
DEVELOP	MF-453 Developer (undil.) for 15-20 min.			**Check every 10 minutes or so of developing time to see if resist has cleared.**
POST PATTERN LITHO INSPEC.	Examine for litho errors or defects; note severity on map			
PAINT W/ RESIST	Paint over the alignment marks and any other litho defects with 5740 resist. Paint around edge with 1818 resist.			
BAKE	Bake for 90 min. at 100°C			
DESCUM	3 min. at 300 W in YES-R3			
ION MILLING OF PNZT, Pt, TiO_2, SiO_2 – SIDE I	Accelerating voltage: 500 V Beam Current: 40 mA Time: 90 minutes Etch rate approx. 100 Å /			**Objective here is to remove 80-90% of PNZT via this dry etch. Done in two or three steps, to monitor etch depth.**

	min.			
POST-MILL INSPECTION	Check milled depth using the Dektak.			
DESCUM	3 min. at 300 W in YES-R3			
RESIST STRIP	Strip on spinner with Acetone and IPA			
SEPARATE STACK	Soak in acetone to separate handle wafer from carrier wafer.			
DESCUM SIDE I	3 min. at 300 W in YES-R3.			
DESCUM SIDE II	3 min. at 300 W in YES-R3.			
RESIST COAT CARRIER WAFER	1818, 2500 rpm/30s for bonding carrier wafer to active wafer			
BOND CARRIER WAFER TO ACTIVE WAFER	Place carrier wafer (resist side up) on bonding jig. Place active wafer (Side II up) on top of carrier wafer. Place top plate on jig. Put jig on hot plate preheated to 70°C. Hold at 70°C for 5 min., ramp to 125°C for 30 min., hold at 125°C for 30 min., ramp down to 70°C for 30 min.			
CLEAN STACK	Strip on spinner with Acetone and IPA			
RESIST COAT	SJR-5740 – Spin using 3 s spread at 400 rpm, followed by a 2000 rpm spin for 10 s. Allow 10 minutes of "relaxation time" at RT prior to baking.			**Resist thickness should be about 15 microns.**
RESIST SOFT BAKE	100 ˚C for 37 min. in oven.			
REHYDRATION	Allow at least one hour for the 5740 photoresist to rehydrate prior to patterning.			
EXPOSE SIDE II	**Mask: UAA1_R04** Karl Suss Contact Aligner Program: Soft Contact Exposure time: 104 s (4 reps of 26 s, with 10 s pauses) **Dose=1360 mJ/cm^2 for 365 nm light.**			
DEVELOP	MF-453 Developer (undil.) for 15-20 min.			**Check every 10 minutes or so of developing time to see if resist has cleared.**
POST PATTERN LITHO INSPEC.	Examine for litho errors or defects; note severity on map			

PAINT W/ RESIST	Paint over the alignment marks and any other litho defects with 5740 resist. Paint around edge with 1818 resist.			
BAKE	Bake for 90 min. at 100°C			
DESCUM	3 min. at 300 W in YES-R3			
ION MILLING OF PNZT – SIDE II	Accelerating voltage: 500 V Beam Current: 40 mA Time: 75 minutes Etch rate approx. 80 Å / min.			**Objective here is to remove 80-90% of PNZT via this dry etch. Done in two or three steps, to monitor etch depth.**
POST-MILL INSPECTION	Check milled depth using the Dektak.			
DESCUM	3 min. at 300 W in YES-R3			
RESIST STRIP	Strip on spinner with Acetone and IPA			
DESCUM	3 min. at 300 W in YES-R3			
RESIST COAT	1811, Prog. 2 , 2500 rpm/30 s			
RESIST SOFT BAKE	100 ˚C, 30 min in oven			**Too low a temp may give wrinkled look to resist edges.**
EXPOSE	**Mask: UAA2_R04** Karl Suss Contact Aligner Program: Vacuum Contact Exposure time: 6 s			
DEVELOP	MP Developer (diluted 1:1). 1 min			
POST PATTERN LITHO INSPEC.	Examine for litho errors or defects; note severity on map			
PAINT W/ RESIST	Paint over the alignment marks and any other litho defects with 1818 resist. Paint around edge with 1818 resist.			
BAKE	Bake for 90 min. at 100°C			
DESCUM	3 min. at 300 W in YES-R3			
WET ETCH PNZT	**400ml H2O,400ml HCl + 8g NH4F** **Etch rate~400nm/min**			**DON'T OVERETCH!!! CAREFUL**
RESIST STRIP	Strip on spinner with Acetone and IPA			
DESCUM	3 min. at 300 W in YES-R3			
INSPECTION OF METAL PATTERN SIDE I	Examine pattern with optical microscope, note defects and severity on defect map			
Microscope and MULTIMETER TEST	Use multimeter to ensure top electrodes and Pt bottom electrode are not in contact			**Measure PNZT Stack feature size here.**

RESIST COAT	SJR-5740 – Spin using 3 s spread at 400 rpm, followed by a 2000 rpm spin for 10 s. Allow 10 minutes of "relaxation time" at RT prior to baking.			**Resist thickness should be about 15 microns.**
RESIST SOFT BAKE	100 ˚C for 37 min in oven.			
REHYDRATION	Allow at least one hour for the 5740 photoresist to rehydrate prior to patterning.			
EXPOSE SIDE II	**Mask: UAA3_R04** Karl Suss Contact Aligner Program: Soft Contact Exposure time: 104 s (4 reps of 26 s, with 10 s pauses) **Dose=1360 mJ/cm^2 for 365 nm light.**			
DEVELOP	MF-453 Developer (undil.) for 15-20 min.			**Check every 10 minutes or so of developing time to see if resist has cleared.**
POST PATTERN LITHO INSPEC.	Examine for litho errors or defects; note severity on map			
PAINT W/ RESIST	Paint over the alignment marks and any other litho defects with 5740 resist. Paint around edge with 1818 resist.			
BAKE	Bake for 90 min. at 100^{o}C			
DESCUM	3 min. at 300 W in YES-R3			
ION MILLING OF PNZT, Pt, TiO_2, SiO_2 – SIDE II	Accelerating voltage: 500 V Beam Current: 40 mA Time: 80 minutes Etch rate approx. 100 Å^o / min.			**Objective here is to remove 80-90% of PNZT via this dry etch. Done in two or three steps, to monitor etch depth.**
POST-MILL INSPECTION	Check milled depth using the Dektak.			
DESCUM	3 min. at 300 W in YES-R3			
RESIST STRIP	Strip on spinner with Acetone and IPA			
DESCUM	3 min. at 300 W in YES-R3			
RESIST COAT	SJR-5740 – Spin using 3 s spread at 400 rpm, followed by a 2000 rpm spin for 10 s. Allow 10 minutes of "relaxation time" at RT prior to baking.			**Resist thickness should be about 15 microns.**
RESIST BAKE	Bake for 40 min. at 100^{o}C.			
REHYDRATION	Allow at least one hour for the 5740 photoresist to rehydrate prior to patterning.			
EXPOSE	**Mask: UAA4_RB4** Karl Suss Contact Aligner Program: Soft Contact			

	Exposure time: 104 s (4 reps of 26 s, with 10 s pauses) **Dose=1360 mJ/cm^2 for 365 nm light.**			
DEVELOP	MF-453 Developer (undil.) for 15-20 min.			**Check every 10 minutes or so of developing time to see if resist has cleared.**
POST PATTERN LITHO INSPEC.	Examine for litho errors or defects; note severity on map			
DESCUM	3 min. at 300 W in YES-R3			
PAINT W/ RESIST	Paint over the alignment marks and any other litho defects with 5740 resist. Paint around edge with 1818 resist.			
BAKE	Bake for 90 min. at 100°C			
ETCH IN DRIE	Process DP_80_01 is ASE. (Deep etch takes 2:55:00)			**Must etch completely through the handle wafer.**
DESCUM	3 min. at 300 W in YES-R3			
RESIST STRIP	Strip on spinner with Acetone and IPA			
SEPARATE STACK	Soak in acetone to separate handle wafer from carrier wafer.			
DESCUM SIDE I	3 min. at 300 W in YES-R3.			
DESCUM SIDE II	3 min. at 300 W in YES-R3.			

APPENDIX B: Wafer Traveler for Handle Wafer

AMCOM – REDSTONE

UA Gyro Wafer Process – Handle Wafer Lot #:
#Wafers/Lot: 5

Wafer :
Purpose:
Targets:

PROCESS FLOW

PROCESS	DECRIPTION	ITL	DATE	COMMENTS

Handle Wafer Process Steps

Process Flow

CHROME COAT	Coat with 300 Å of chrome **E-Beam Evaporator** **Cr: Deposit. Rate: 1 Å /s** **E-beam Power: 4%**			
RESIST COAT	Coat with 1818 photoresist (2500 rpm for 30 s)			
BAKE	30 min. in 100°C oven			
EXPOSE	Expose for 6 s in Suss using mask UAH0_R04 Program: Vacuum Contact			
DEVELOP	Microposit Dev. Conc (Diluted 1:1 wit DI water) for 2 min. Then rinse.			
DESCUM	3 min. at 300 W in YES-R3			
CHROME ETCH	45 s in CEP-200 chrome etchant.			
POST-ETCH INSPECTION	Examine to insure that all chrome has cleared and that edge of features look good			
RESIST STRIP	Strip using acetone and IPA on spinner			
DESCUM	3 min. at 300 W in YES-R3			
POLYIMIDE COAT	Spin on HD Microsystems 2723 Photodefineable polyimide. Start spread at 100 RPM. Slowly increase spin rate until entire wafer is covered. Then spin at 3760 RPM for 45 s.			
SOFT BAKE	Bake on a hot plate for 3 min. at 110°C.			
EXPOSE	Expose for 70 s in Suss using mask UAH1_R04 Program: Soft Contact			
DEVELOP	Perform a dynamic development. (15 s with 6180 developer at 750 r.p.m, 30 s with 6180 developer at 0 r.p.m, 15 s with 6180 developer at 750 r.p.m., 30 s with 50-50 mix of 6180 developer and 9180 rinse at 750 r.p.m., 30 s with 9180 rinse at 750 r.p.m., then spin at 2500 r.p.m. for 30 s to dry).			
INSPECT	Inspect microscopically to insure complete development. Measure the height of the polyimide pads using the Dektak.			**At this stage, the pads should be about 3.4 microns tall**
HARD BAKE	10 min on 270°C Hot Plate			
INSPECT	Measure the height of the polyimide pads using the			**At this stage, they should be about 2.2 microns tall.**

	Dektak.			
DESCUM	3 min. at 300 W in YES-R3			
COAT CARRIER WITH BONDING LAYER OF RESIST	1818, Prog. 2, 2500 rpm for 30 s			
ASSEMBLE STACK	Place the 4 in carrier wafer, resist side up, on the bottom plate of bonding jig. Place the handle wafer top of the carrier wafer, polyimide side up. Place a cover wafer on top of the active wafer. Carefully lower the top plate onto the stack.			
BAKE	Place carrier wafer (resist side up) on bonding jig. Place active wafer (Side I up) on top of carrier wafer. Place top plate on jig. Put jig on hot plate preheated to 70°C. Hold at 70°C for 5 min., ramp to 125°C for 30 min., hold at 125°C for 30 min., ramp down to 70°C for 30 min.			
CLEAN STACK	Perform acetone/IPA strip and/or descum as needed			
RESIST COAT	SJR-5740 – Spin using 3 s spread at 400 rpm, followed by a 2000 rpm spin for 10 s. Allow 10 minutes of "relaxation time" at RT prior to baking.			**Resist thickness should be about 15 microns.**
RESIST BAKE	Bake for 37 min. at 100°C.			
REHYDRATION	Allow at least one hour for the 5740 photoresist to rehydrate prior to patterning.			
EXPOSE	**Mask: UAH2_R04** Karl Suss Contact Aligner Program: Soft Contact Exposure time: 150 s (5 reps of 30 s, with 10 s pauses) **Dose=1360 mJ/cm^2 for 365 nm light.**			
DEVELOP	MF-453 Developer (undil.) for 15-20 min.			**Check every 10 minutes or so of developing time to see if resist has cleared.**
POST PATTERN LITHO INSPEC.	Examine for litho errors or defects; note severity on map			

PAINT W/ RESIST	Paint over the alignment marks and any other litho defects with 5740 resist. Paint around edge with 1818 resist.			
BAKE	Bake for 90 min. at 100°C			
DESCUM	If necessary Technics 2 min O_2 descum			
ETCH IN DRIE	Shallow etch takes 5 min.			
DESCUM	3 min. at 300 W in YES-R3. Removes hard shell from surface of resist.			
RESIST STRIP	Strip using acetone and IPA on spinner			
DESCUM	3 min. at 300 W in YES-R3.			
INSPECT	Check for etch defects, excessive undercut. Dektak to verify etch depth.			**Etch depth should be about 10 microns.**
RESIST COAT	SJR-5740 – Spin using 3 s spread at 400 rpm, followed by a 2000 rpm spin for 10 s. Allow 10 minutes of "relaxation time" at RT prior to baking.			**Resist thickness should be about 15 microns.**
RESIST BAKE	Bake for 37 min. at 100°C.			
REHYDRATION	Allow at least one hour for the 5740 photoresist to rehydrate prior to patterning.			
EXPOSE	**Mask: UAH3_R04** Karl Suss Contact Aligner Program: Soft Contact Exposure time: 150 s (5 reps of 30 s, with 10 s pauses) **Dose=1360 mJ/cm^2 for 365 nm light.**			
DEVELOP	MF-453 Developer (undil.) for 15-20 min.			**Check every 10 minutes or so of developing time to see if resist has cleared.**
POST PATTERN LITHO INSPEC.	Examine for litho errors or defects; note severity on map			
PAINT W/ RESIST	Paint over the alignment marks and any other litho defects with 5740 resist. Paint around edge with 1818 resist.			
BAKE	Bake for 90 min. at 100°C			
DESCUM	If necessary Technics 2 min O_2 descum			

ETCH IN DRIE	Deep etch takes 2.5 – 3 hours.			**Must etch completely through the handle wafer.**
SEPARATE STACK	Soak in acetone to separate handle wafer from carrier wafer.			
DESCUM TOP	3 min. at 300 W in YES-R3.			
DESCUM BOTTOM	3 min. at 300 W in YES-R3.			